UC Santa Barbara
UC Santa Barbara Electronic Theses and Dissertations

Title
A Frequency-agile Terahertz Heterodyne Detector Based on Intersubband Transitions in Single Quantum Wells

Permalink
https://escholarship.org/uc/item/4832f0f7

Author
Yoo, Changyun

Publication Date
2022

Peer reviewed|Thesis/dissertation

eScholarship.org Powered by the California Digital Library
University of California

University of California
Santa Barbara

A Frequency-agile Terahertz Heterodyne Detector Based on Intersubband Transitions in Single Quantum Wells

A dissertation submitted in partial satisfaction
of the requirements for the degree

Doctor of Philosophy
in
Physics

by

Changyun Yoo

Committee in charge:

Professor Mark Sherwin, Chair
Professor Andrea Young
Professor Nathaniel Craig
Boris Karasik, Ph.D., NASA Jet Propulsion Laboratory

June 2022

The Dissertation of Changyun Yoo is approved.

Professor Andrea Young

Professor Nathaniel Craig

Boris Karasik, Ph.D., NASA Jet Propulsion Laboratory

Professor Mark Sherwin, Committee Chair

April 2022

A Frequency-agile Terahertz Heterodyne Detector Based on Intersubband Transitions in Single Quantum Wells

Copyright © 2022

by

Changyun Yoo

To my parents, Wansuk Yoo and Hyunsuk Kim

Acknowledgements

First and foremost, I'd like to express my gratitude to Prof. Mark Sherwin, who kindly took me under his wings, placed me in one of the coolest (and most difficult) research projects that I've ever worked on, and guided me all the way to completion of this dissertation. I especially thank him for remaining optimistic in the face of many mistakes and setbacks that I created and for allowing me to go through and explore them at my own pace. Without his patience, guidance, and advice, this work would have been impossible.

I would also like to thank my collaborators at Jet Propulsion Laboratory, Dr. Boris Karasik and Dr. Jon Kawamura. I was fortunate to work with not just one, but three outstanding senior scientists. I can only imagine how painful it must have been for them to work with a toddler in science and engineering like myself during the early phase of this project, and I'm constantly in awe of their generosity and patience as I reflect on my past mistakes. Their expertise not only on THz science and technology but also on scientific and engineering research in general has constantly inspired and helped me to move on throughout this project.

I thank my other committee members, Prof. Andrea Young and Prof. Nathaniel Craig, for their support, help, and guidance throughout my defense and writing of this dissertation.

My sincere thanks also go to Prof. Loren Pfeiffer and Dr. Ken West at Princeton University who grew us arguably the world's best and cleanest GaAs/AlGaAs quantum-well samples. Also, I'd like to thank Dr. Mengchen Huang, who gave me a 3-month crash course in clean-room processing, when I didn't even know exactly what GaAs is. I also thank the staff members in the UCSB Nanofab, especially Dr. Brian Thibeault and Dr. Demis D. John for their help in consulting our fabrication process. Also, I'd like to

thank Dr. Amanda Strom in Material Research Lab for her help in taking care of the Low T lab. I thank Dr. Nick Agladze for his help in lab.

I'd also like to thank my current and past lab mates—Seamus O'hara, Joe Costello, Brad Price, Dr. Qile Wu, Dr. Hunter Banks, Dr. Darren Valovcin, Dr. Jessica Clayton, Dr. Blake Wilson, Dr. Marzieh Kavand, and Dr. Xialing (Cocoa) Wang—for their companies in the lab. I especially thank our current lab members—Seamus O'hara, Joe Costello, Brad Price, and Dr. Qile Wu—for their support and help throughout the past four months. I thank Dr. Minwook Park, Dr. Jongyeon Lee, Dr. Seungchan Lee, and Dr. Wonho Lee for their companies and help when I was preparing for the defense and writing this dissertation. I'd also like to thank current and past members of the Korean Surf gang. I especially thank Sangcheol Yoon, Hyunjun Kim, and Danny Lim for their support and friendship both inside and outside the lineup. Also, special thanks to Dr. Seunggeun Lee, Dr. Jaehwan Chu, and Dr. Daehwan Jung for their friendship in the early days of my PhD studies.

Last but not the least, I would like to thank my family, my parents and sisters, for supporting me from a far. I especially thank my parents for teaching me how to be independent, and how to remain positive through the obstacles of life.

Curriculum Vitæ
Changyun Yoo

Education

2022	Ph.D., Physics, University of California, Santa Barbara, California
2018	M.A., Physics, University of California, Santa Barbara, California
2015	B.A. cum laude, Physics, Amherst College, Amherst, MA

Professional Experience

2016-2022	Graduate research assistant, Physics Department, UCSB
2015-2016	Teaching assistant, Physics Department, UCSB
2013-2015	Undergraduate research assistant, Physics and Astronomy Department, Amherst College
2013-2015	Undergraduate grader and lab assistant, Physics and Astronomy Department, Amherst College

Military Experience

2010-2012	Military training administrative specialist, Republic of Korea Army

Publication

Yoo, C., Huang, M., Kawamura, J. H., West, K. W., Pfeiffer, L. N, Karasik, B. S., and Sherwin, M. S. "Demonstration of a tunable antenna-coupled intersubband terahertz (TACIT) mixer." Applied Physics Letters 116, 013504 (2020)

Manuscripts in Preparation

Yoo, C., Huang, M., Kawamura, J. H., West, K. W., Pfeiffer, L. N, Karasik, B. S., and Sherwin, M. S "Indium-Bond-And-Stop-Etch (IBASE) Technique for Dual-side Processing of Thin GaAs/AlGaAs Heterostructure Devices."

Yoo, C., Huang, M., Kawamura, J. H., West, K. W., Pfeiffer, L. N, Curwen, C. A., Karasik, B. S., and Sherwin, M. S "Impedance Models for Tunable Antenna-Coupled Intersubband Terahertz (TACIT) Mixers"

Conference Abstracts

Yoo, C., Huang, M., Kawamura, J. H., West, K. W., Pfeiffer, L. N, Karasik, B. S., and Sherwin, M. S. "Design Study for Optimal Performance of Tunable Antenna Coupled Intersubband Terahertz (TACIT) Mixer." Talk presented at: 31st IEEE International Symposium on Space THz Technology (ISSTT2020); March 10, 2020; Tempe, AZ, USA.

Yoo, C., Huang, M., Kawamura, J. H., West, K. W., Pfeiffer, L. N, Karasik, B. S., and Sherwin, M. S. "Tunable Antenna-Coupled Intersubband Terahertz (TACIT) Mixers." Talk presented at: 2019 Infrared Terahertz Quantum Workshop (ITQW 2019); September 20, 2019; Ojai, CA, USA.

Yoo, C., Huang, M., Kawamura, J. H., West, K. W., Pfeiffer, L. N, Karasik, B. S., and Sherwin, M. S. "Demonstration of a Frequency-agile Quantum-well Based THz Heterodyne Detector." Talk presented at: 2019 44th International Conference on Infrared, Millimeter, and Terahertz Waves (IRMMW-THz 2019); September 6, 2019; Paris, France.

Yoo, C., Huang, M., Kawamura, J. H., West, K. W., Pfeiffer, L. N, Karasik, B. S., and Sherwin, M. S. "Demonstration of a TACIT Heterodyne Detector at 2.5 THz." Talk presented at: 30th IEEE International Symposium on Space THz Technology (ISSTT2019); April 17, 2019; Gothenburg, Sweden.

Yoo, C., Huang, M., Kawamura, J. H., West, K. W., Pfeiffer, L. N, Karasik, B. S., and Sherwin, M. S. "A Tunable Antenna-coupled Intersubband Terahertz Detector." Poster presented at: 29th IEEE International Symposium on Space THz Technology (ISSTT2018); March 27, 2018; Pasadena, CA, USA.

Honors

2018-2019	The Amherst Memorial Fellowship
2016-2018	The Forris Jewett Moore Fellowship
2015	The Bassett Physics Prize
2015	Summer Research Award
2013	Howard Hughes Medical Institutde Summer Science Research Fellowship
2012-2015	Amherst College International Student Scholarship
2009-2010	Amherst College International Student Scholarship

Abstract

A Frequency-agile Terahertz Heterodyne Detector Based on Intersubband Transitions in Single Quantum Wells

by

Changyun Yoo

Terahertz (THz) heterodyne detectors, also known as mixers, are widely used for high-resolution (with frequency resolution $\nu/\Delta\nu > 10^6$) detection of THz radiation in space for astrophysics and planetary science applications, and important for applications in bio-medical imaging and future THz wireless communications. Above 1 THz, heterodyne detectors based on hot-electron effects in thin superconducting films (superconducting hot-electron bolometers, or HEBs) are the current state-of-the art mixers, with an excellent sensitivity (with single-sideband noise temperature $T_{SSB} \sim 1,000$ K at 2 THz), a wide intermediate-frequency (IF) bandwidth (∼3 GHz), and a small required local-oscillator (LO) power (∼1 μW). However, cryogenic operating temperature (4 K or below) required for the superconducting HEBs limits their use in certain applications (e.g. deep-space missions to planets and comets) that cannot afford the power and mass required for active cryogenic cooling. To date, the only option for such applications has been Schottky-diode mixers that work at ambient temperature, but at the cost of significantly lower sensitivity ($\mathrm{T_{SSB}} \sim 10,000$ K above 1 THz) and a higher required LO power (∼1 mW). The latter especially limits the use of Schottky mixers in heterodyne array applications, which is important for cost- and time-effective heterodyne observations in space.

In this work, we explore a new type of THz heterodyne detector based on intersubband transitions of high-mobility 2-dimensional electron gas (2DEG) confined in single

GaAs/AlGaAs quantum wells. Named as Tunable Antenna-Coupled Intersubband Terahertz (TACIT) mixer, our device is predicted to be as sensitive as superconducting HEB mixers (with $T_{SSB} \sim 1,000$ K) at relatively high operating temperature (20–60 K), with a wide IF bandwidth ($\sim$ 10 GHz) and a small required LO power ($< 1\mu$W). In addition, THz absorption frequency of TACIT mixers can be tuned with small (< 2) DC voltage biases, offering wide in-situ tunability in the detection frequency (2–5 THz). The operating temperature of TACIT mixers can be accessible with passive cooling for deep-space missions or with compact, light-weight coolers for other applications, which, along with other useful mixer characteristics, makes TACIT mixers an attractive mixer technology for a low-noise, multi-pixel THz heterodyne receiver for applications in THz high-resolution spectroscopy in deep space and for other applications in which relaxed cryogenic and LO power requirements are advantageous.

Despite the impressive mixer characteristics of TACIT mixers, experimental realization and characterization of the TACIT mixers have been challenging due to difficulties in fabricating reliable dual-gate structures required for their operation. In this work, using an advanced flip-chip technique that we developed in-house, we successfully fabricate and demonstrate two versions of prototype TACIT mixers. In the first prototype TACIT mixer integrated with a single slot antenna, we demonstrate the tunability in the detection frequency (2.52–3.44 THz) with relatively small (< 5 V) DC bias voltages, as well as the heterodyne detection (mixing) capability at 60 K with a wide IF bandwidth ($\sim$ 6 GHz). The observed tunability in the direct detection responses is consistent with the model responses based on intersubband transitions. In the second prototype TACIT mixers integrated with a modified, broadband bow-tie antenna, we explore capacitive coupling for the read-out of the device IF response and investigate the capacitive IF read-out and other properties of the device using various characterization methods, including microwave measurements and noise power measurements. In addi-

tion, we demonstrate tunability in both the direct detection and heterodyne detection consistent with the results from the first prototype TACIT mixer and with our model responses. In both prototype devices, the mixer noise temperature, conversion loss, and required LO power were not measured due the unexpectedly large conversion losses. We attribute these large losses to poor radiation efficiency of the antenna structures caused by impedance mismatch and non-optimal radiation patterns, as well as to possible degradation in the IF response caused by diffusion and ballistic cooling of the high-mobility 2DEG at low temperatures. To address these issues, we briefly discuss our plans for designing more optimized antenna structures and employing a different read-out mechanism based on the thermoelectric effect of high-mobility 2DEGs for future iterations of TACIT mixers.

Contents

Curriculum Vitae **vii**

Abstract **ix**

1 Introduction **1**
1.1 Motivation . . . 1
1.2 THz Heterodyne Detection System . . . 3
1.3 Two-terminal Mixers Based on 2-dimensional Electron Gas (2DEG) . . . 7
1.4 Tunable Antenna Coupled Intersubband Terahertz (TACIT) Mixer . . . 9

2 Device Operation and Modeling Results **15**
2.1 Device Operation . . . 16
2.2 Modeling Results . . . 24

3 Device Fabrication **49**
3.1 Previous Back-gating Techniques . . . 50
3.2 Indium-Bond-And-Stop-Etch (IBASE) Process . . . 52
3.3 Characterization Results . . . 56

4 Resistively-coupled Device **61**
4.1 Device Design and Fabrication . . . 63
4.2 IV Characterization . . . 66
4.3 THz Measurements . . . 69

5 Capacitively-coupled Device **81**
5.1 Device Design and Fabrication . . . 83
5.2 IV Characterization . . . 86
5.3 Microwave Characterization . . . 93
5.4 THz Measurements . . . 97
5.5 Noise Power Measurements . . . 100

6 Conclusions and Outlook **108**

A Heterodyne Detection Theory **110**

B Calculation of Intersubband Absorption Frequency **112**

C Indium-Bond-And-Stop-Etch (IBASE) Process Details **116**
C.1 Front-side Processing 117
C.2 Flip-chip Assembly 126
C.3 Backside Processing 131

D Finite-Element Method (FEM) Simulation Results **136**

Bibliography **146**

Chapter 1

Introduction

1.1 Motivation

Over the last several decades, THz radiation—loosely defined as electromagnetic radiation spanning the frequency range of 100 GHz to 10 THz[1]—has gained increasing attention in fields as diverse as remote sensing [1, 2, 3], astronomy [4, 5, 6, 7, 8], fundamental and applied physics research [9, 10, 11, 12], bio-medical imaging [13, 14], and future wireless communication [15, 16, 17]. Despite such widespread interest, the THz spectral range still remains as the least explored region in the electromagnetic spectrum, primarily due to difficulties in atmospheric transmission[2] and relatively immature source and detector technology (so-called THz gap). While these two factors continue to be significant challenges to overcome for many of the THz applications, the great wealth of scientific knowledge that can be gained in this frequency regime has continued to

[1]Equivalent to 3 mm down to 30 μm in wavelength, 0.41 meV to 41 meV in energy scale, and 1.7 K to 170 K in equivalent black-body temperature. In this work, however, we will mostly focus on 2 – 5 THz range, which corresponds to the detection frequency of our device.

[2]THz radiation is significantly attenuated in the atmosphere due to high absorption by water vapor. Above 1 THz, atmospheric attenuation is typically greater than 100 dB/km, peaking at around 8 THz with $\sim 2 \times 10^5$ dB/km attenuation, resulting in less than 1 % transmission over a 10 cm atmospheric path near these absorption peaks [18, 19].

motivate and drive THz technology development.

A major scientific driving force, and perhaps the most traditional application of THz technology, comes from astronomy and remote sensing. A variety of astronomical objects such as interstellar dust and many atoms, ions, and molecules in space (including oxygen, nitrogen, carbon, carbon monoxide, water, and many other species) emit THz radiation through either continuous black-body radiation or discrete line emission via transitions in rotational and vibrational modes [4, 5, 6, 8]. In particular, the black-body radiation of cold (15–150 K) dust in interstellar space peaks in THz region and, along with the discrete emission lines, provides useful information on the physical and chemical conditions of the interstellar space, which is important for understanding various cosmological and astronomical processes, such as the formation and evolution of stars [5, 6, 7, 8]. In addition, the THz spectral signatures of atoms, ions, and molecules are also present in the atmospheres of planets (including our own) and comets in our Solar system, and measuring these spectral signatures provides data on the atmospheric chemistry and dynamics critical for modeling and studying various atmospheric phenomena (such as ozone depletion and global warming in the case of Earth), as well as the origin and the evolution of our Solar system [1, 2, 6]. Such wealth of information that can be obtained in THz radiation in space has motivated significant investment in THz instrumentation for space applications, and numerous ground-based, balloon-based [20], airborne [21], and space [22] telescopes, as well as a cometary orbiter [23] targeting THz range[3] have been deployed so far [6, 8].

One particular application in astronomy and remote sensing that motivates this work is high-resolution (with frequency resolution $\nu/\Delta\nu > 10^6$) detection of THz radiation in space. The high-resolution detection enables precise measurements of the spectral line shapes of individual emission lines, including fine Doppler broadening and other fine

[3] 190 GHz and 562 GHz for the cometary orbiter [23].

structures that are sensitive to the environment and dynamics of the spectral sources. By measuring and processing these individual line shapes with the fine structures, one can learn not only about the existence and abundance of spectral sources but also about their physical and chemical conditions, such as temperature, density, wind velocity, and the presence of magnetic fields [5]. Especially, the high-resolution detection can resolve Doppler velocities of sub-km/s, enabling the study of the complex motion of interstellar medium [7, 24]. Such broad and unique observation capability makes THz high-resolution spectroscopy a powerful tool for studying physical, chemical, and dynamic processes in the intersterllar medium and in the atmospheres of planets and comets in our Solar system [7].

1.2 THz Heterodyne Detection System

At THz frequencies, such high-resolution detection is enabled by a heterodyne receiver[4], which transfers spectral information in a high-frequency signal to a much lower frequency for further processing and detection. In a typical THz heterodyne system (see Figure 1.1), an incoming THz signal (referred as RF following the convention in radio waves where the heterodyne technique was first developed) is combined, or "mixed" with another THz signal provided by a local oscillator (LO), and down-converted to an intermediate-frequency (IF) signal with a frequency several orders of magnitude lower than the RF.[5] The down-converted IF signal, which typically falls in microwave range where amplification and detection technology is mature, is then amplified with a series of amplifiers and processed with a back-end spectrometer for further signal processing.

[4] This is due to the fact that, for direct detectors at THz frequencies, the use of diffraction gratings and other frequency selection techniques is limited, which typically yields a frequency resolution $< 10^5$ [25].

[5] This down-conversion process can be understood in terms of simple trigonometry. For details, see Appendix A.

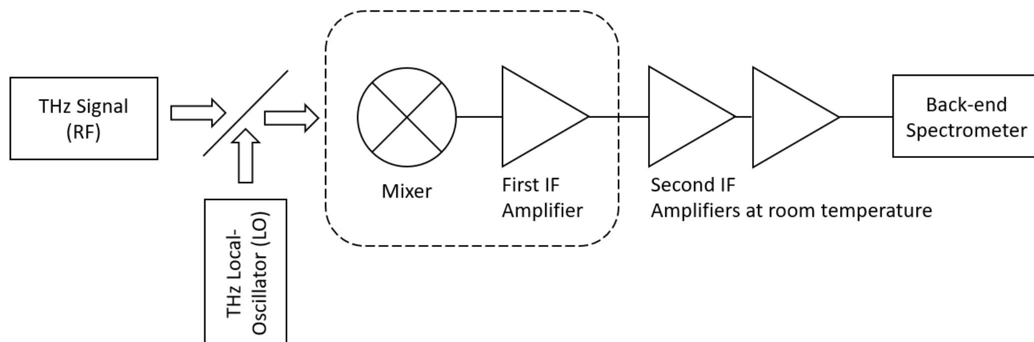

Figure 1.1: Schematic for a THz heterodyne receiver system. The dotted area shows the front-end of the system which is cooled to operating temperatures of the mixer and the low-noise amplifier in use. The second-stage room-temperature amplifiers further amplify the intermediate-frequency (IF) signal, which is detected by the back-end spectrometer.

Among the numerous components that make up a heterodyne receiver, a non-linear element known as a mixer is the key element that performs the down-conversion and determines the overall sensitivity of a heterodyne system T_{REC}[6], which is given by

$$T_{REC} = T_M + L_M T_{IF} \tag{1.1}$$

where T_M is mixer noise temperature, L_M is mixer conversion loss (this is defined as a ratio of the IF power at the output of a mixer divided by the RF power at its input), and T_{IF} is noise temperature of the first IF amplifier [26, 27].[7] The receiver noise temperature T_{REC} in turn determines the minimum detectable temperature difference δT_{min} for a signal of interest:

$$\delta T_{min} = \frac{k_{REC} T_{REC}}{\sqrt{\tau B}} \tag{1.2}$$

[6]Noise temperature is defined as the temperature of a black body at the input of an ideal, noise-less device that would generate the same noise power as that of a real, noisy device at its output. For detailed treatment on this, refer to [26] and [27].

[7]As we can see in Figure 1.1, a heterodyne receiver typically has more than one amplifier in the back end, but the noise contribution after the first amplifier is significantly reduced by the large gain of the first amplifier and can be ignored in most cases. For details, see [26].

where k_{REC} is a receiver sensitivity constant (typically 1 to 2 depending on receiver type), τ is the integration time, and B is the pre-detection bandwidth [26]. To get a numerical sense of Eq. 1.2, for a heterodyne receiver with $T_{REC} = 3,000$ K (we assume $K_{REC} = 1$), with values of 1 hr for τ and 250 kHz for B , we get $\delta T_{min} = 0.1$ K, which achieves a signal-to-noise (SNR) ratio of 10 for a typical 1 K astronomical source [28]. Because the integration time scales with $1/T_{REC}^2$ for a given δT_{min} and δT_{min} scales linearly with T_{REC} for a given integration time, a heterodyne detector with a lower noise temperature and conversion loss (and hence with a lower receiver noise temperature) can greatly reduce observation times with the given δT_{min} or detect weaker signals with the given τ. For example, with a heterodyne receiver with $T_{REC} = 1,000$ K, compared with a $3,000$-K receiver, we get a 9-fold improvement on the integration time ($\tau = 400s$) for the same $\delta T_{min} = 0.1$ K, or on the sensitivity $\delta T_{min} = 0.03$ K with the same integration time of $\tau = 1$ hr.

Along with the mixer noise temperature and conversion loss, some other mixer parameters are worth mentioning here. These include operating temperature, IF bandwidth, and required LO power. The operating temperature of a mixer is determined by the temperature necessary for the mixing mechanism to occur in the mixer and often determines the cooling requirement of a heterodyne receiver. As we will see shortly, having active cooling requirement (for example, cooling down to 4 K or lower for superconductor-based detectors) can add significant mass load to the receiver and can substantially reduce its lifetime. The IF bandwidth, defined as the -3dB fall-off frequency for the IF power, is another critical mixer parameter that affects the spectral range of heterodyne measurements. In particular, a mixer with a wide IF bandwidth is important for simultaneous observation of multiple lines, which improves both observation efficiency and calibration accuracy in heterodyne measurements [8]. Lastly, the required LO power is the minimum LO power required for the mixer and one of the key mixer parameters due to the lack

of reliable, compact high-power source at THz frequencies. Especially, a small required LO power is critical for heterodyne array applications, which is important for time- and cost-effective heterodyne measurements.

The main motivation for this work comes from the continuous and ongoing need for a sensitive mixer in the frequency range 1–5 THz that operates at a high operating temperature (> 20 K) with a wide IF bandwidth (∼10 GHz) and a small required LO power ($< 1\mu$W) [7, 8, 24], particularly for applications in THz high-resolution spectroscopy in deep space (e.g. atmospheres of planets and comets in our Solar system). In this THz frequency range, heterodyne detectors based on hot-electron effects in thin superconducting films (superconducting hot-electron bolometers, or HEBs) are the current state-of-the-art mixers that offer an excellent sensitivity (with single-sideband noise temperature $T_{SSB} \sim 1,000$ K at 2 THz[8]), a wide intermediate-frequency (IF) bandwidth (∼3 GHz), and a small required local-oscillator (LO) power (∼1 μW) [29]. However, cryogenic operating temperature (4 K or below) required for the superconducting HEBs limits their use in certain applications (i.e. deep-space missions to planets and comets) that cannot afford the power and mass required for active cryogenic cooling. To date, the only option for such applications has been Schottky-diode mixers that work at ambient temperature, but at the cost of significantly lower sensitivity ($\mathrm{T_{SSB}} \sim 10,000$ K above 1 THz) and a higher required LO power (∼1 mW) [29]. The latter especially limits the use of Schottky mixers in heterodyne array applications.

In this dissertation, we explore a new type of THz heterodyne detector based on intersubband transitions of high-mobility 2-dimensional-electron gas (2DEG) confined in single GaAs/AlGaAs quantum wells. Named as Tunable Antenna-Coupled Intersubband Terahertz (TACIT) mixer, our device is predicted to be as sensitive as superconducting

[8] Depending on whether the receiver operates in single-sideband (SSB) mode or double-sideband (DSB) mode, the receiver noise can be assigned to either one or two sidebands. With the same noise contributions for both cases, we have $T_{SSB} = 2T_{DSB}$ [26].

HEBs (with $T_{SSB} \sim 1,000$ K) at much higher operating temperatures (20–60 K), with a wide IF bandwidth ($\sim$ 10 GHz) and a small required LO power ($< 1\mu$W). In addition, the detection frequency of our device can be easily tuned with small DC bias voltages, offering wide in-situ tunability in the detection frequency (2–5 THz). The operating temperature of TACIT mixers can be accessible with passive cooling for deep-space missions and with compact, light-weight cryocoolers for other applications, and the small required LO power allows for multi-pixel applications, making TACIT mixers a useful mixer technology for a low-noise, multi-pixel heterodyne receiver for THz high-resolution spectroscopy for deep-space missions, and for other applications in which relaxed cryogenic and LO power requirements are advantageous.

1.3 Two-terminal Mixers Based on 2-dimensional Electron Gas (2DEG)

Before we introduce TACIT mixers in more detail, a brief review on previous 2DEG-based mixers is useful. First recognized by Smith et al. [30] as possible bolometric material for fast THz direct detectors[9], high-mobility 2DEGs had been proposed as an alternative bolometric medium for both phonon-cooled [31] and diffusion-cooled [32] HEB mixers at microwave and THz frequencies throughout the early 1990s and 2000s. Possible advantages in high temperature operation and a wide IF bandwidth were recognized in both types of 2DEG-based mixers, with an IF bandwidth of $\sim$ 10 GHz at 77 K and a conversion loss of 8 dB predicted for the phonon-cooled devices [31], and an IF bandwidth

[9] The demonstrated direct detector was based on high-mobility 2DEG with charge density $n_s \sim 2 \times 10^{11}$ cm^{-2} and mobility $\mu = 6 \times 10^5$ cm^2/V-s at 4.2 K. The detector used magnetic subbands (Landau levels) for frequency-agile detection of THz radiation at 94 GHz and at 2.52 THz with an applied magnetic field of 0.2 T and 6.2 T, respectively. A responsivity of 200 V/W was measured at 94 GHz with an noise-equivalent-power (NEP) of $5 \times 10^{-11} W/\sqrt{Hz}$ at 4 K. The responsivity and the NEP were not measured for 2.52 THz.

Figure 1.2: Schematic showing the two-terminal geometry of a conventional 2DEG-based HEB mixer. A planar THz antenna is integrated with the two Ohmic contacts shown in the schematic. The antenna orients the electric fields of THz RF and LO along the 2DEG plane for coupling via Joule heating in the 2DEG. The heating results in the change in the mobility of the 2DEG and results in the change in the in-plane resistance of the 2DEG. This bolometric response for the IF is coupled out by the two Ohmic contacts.

of $\sim$ 100 GHz and a DSB noise temperature T_{DSB} of $\sim 1,000$ K (at 1 THz) at 77 K predicted for the diffusion-cooled devices [32].

These 2DEG-based mixers follow the conventional two-terminal HEB mixer design, in which a THz planar antenna structure is integrated with the two terminals (two Ohmic contacts) of the devices (Figure 1.2). The integrated antenna structures orient THz RF and LO electric fields along the 2DEG plane, and THz absorption occurs via Ohmic losses, or Joule heating, of the 2DEG. This causes an increase in electron temperature in the 2DEG channel, and the strong temperature dependence of the mobility of the 2DEG results in a change in the in-plane resistance of the device. The heating of electrons can be very fast, with the energy relaxation times of 10–100 ps at 50–150 K for the phonon-cooled devices [33] and smaller for the diffusion-cooled devices [32], allowing the devices to operate with wide ($>$ 10 GHz) IF bandwidths at relatively high operating temperatures near 77 K.

As shown in Table 1.3, these two-terminal devices had initial successes in demonstrating mixing with wide IF bandwidths ranging from 3 GHz for phonon-cooled devices [34], to 20 GHz for diffusion-cooled devices [35], and even up to 40 GHz for ballistically-cooled devices [36]. However, the operating frequency of these device was largely limited to the millimeter-wave range because of large kinetic inductance of high-mobility 2DEGs [37]

that prevents efficient RF and LO absorption at THz frequencies via Joule heating. The kinetic inductance is inversely proportional to charge density, and can be significantly large in high-mobility 2DEGs whose charge density is orders of magnitude smaller than that of a typical metal. In terms of numbers, for a typical charge density of $\sim 2\times10^{11}$ cm^{-2} in a 2DEG system, the kinetic inductance is $\sim$ 1 nH/□, which yields a large reactance ωL_k of $\sim$ 6 kΩ for a square of 2DEG at 1 THz.[10] As a result, the conversion efficiency of the two-terminal 2DEG-based HEB mixers significant degrades above the practical upper frequency limit of 500 GHz [36], limiting the application of the two-terminal 2DEG HEB mixers at THz frequencies.

Table 1.1: Previous Experimental Demonstration of two-terminal 2DEG-based Mixers

	IF Bandwidth (GHz)	Temperature (K)	RF Frequency (GHz)
Phonon-cooled [34]	3	20	94
Diffusion-cooled [35]	20	77	115
Ballistically-cooled [36]	40	1.5	105

1.4 Tunable Antenna Coupled Intersubband Terahertz (TACIT) Mixer

TACIT mixers overcome the frequency limit in two-terminal 2DEG HEB mixers by using two additional gates to achieve a high THz coupling efficiency via intersubband transitions of 2DEGs in single quantum wells. In this four-terminal device scheme (see Figure 1.3), two Ohmic contacts (source and drain) are used to apply a DC bias current and couple out the IF response in the in-plane resistance of the device and two additional gates (top gate and bottom gate) are used to couple in THz RF and LO into the active region of the device, where THz radiation is resonantly absorbed by the 2DEG via an

[10] Large compared with a typical resistance value of 50-100 Ω for a square of 2DEG near 77 K.

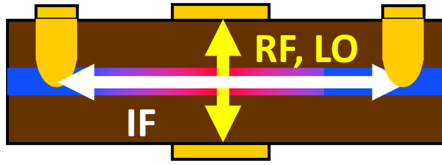

Figure 1.3: Schematic showing the four-terminal geometry of a TACIT mixer. A THz antenna structure is integrated with the two Schottky gates (top and bottom gates) shown in the schematic. To satisfy the selection rule for intersubband transitions, the antenna orients the electric fields of THz RF and LO perpendicular to the 2DEG plane (along the growth direction of the heterostructures). The THz intersubband absorption results in a change of 2DEG mobility via either bolometric effect (electron heating) or change in the subband mobility, and leads to a change in the in-plane resistance of the 2DEG. The two Ohmic contacts, biased with constant current, pick up this IF response.

intersubband transition. The absorbed THz energy promotes the electrons from the first subband to the second subband.[11] The electrons thermalize quickly above 50 K [38] and can heat up the active region, resulting in a fast bolometric response in the device resistance that follows the IF at GHz frequencies. To satisfy the selection rule for an intersubband transition in a confined 2DEG [39, 40], a planar antenna structure is integrated in the bottom gate metallization to orient the THz electric fields perpendicular to the 2DEG plane.

The use of intersubband transition in TACIT mixers offers numerous advantages over the two-terminal 2DEG-based HEB mixers. First of all, the intersubband absorption allows for more efficient coupling of THz radiation into high-mobility 2DEG, with the predicted coupling efficiency greater than 80 %[12], overcoming the frequency limitation of previous 2DEG-based HEB mixers. In addition, the detection frequency of TACIT mixers, which is determined by the absorption frequency for the intersubband transition between the first and the second subbands in the quantum wells, can be tunable with

[11]We will get into this in more detail in the next chapter.
[12]This is evaluated based on the impedance model for intersubband absorption [41] and one of the main topics in Chapter 2.

small DC biases, yielding wide in-situ tunability in the detection frequency (2–5 THz). Lastly, the use of intersubband transitions for THz absorption naturally separates the RF absorption channel from the IF read-out channel in TACIT mixers (see Figure 1.3), which allows for separate optimization of the individual channels for more efficient impedance matching and offers flexibility in device design.[13]

Before concluding the chapter, we provide a brief history of TACIT mixer development. TACIT detectors were initially proposed as fast THz direct detectors based on the rapid relaxation of intersubband transitions [42]. Soon they were recognized for their potential as THz mixers [43], and various IF read-out mechanisms, including bolometric response and mobility change due to either impurity scattering or mobility difference between subbands, were theoretically investigated [44, 45, 46]. Based on the RF impedance model for intersubband transitions [41], high THz coupling efficiency ($> 80\%$) as well as near quantum-noise-limited mixer performance was predicted[14], with a SSB noise temperature of 330 K with a required LO power of 0.5μW for 2.3 THz at 50 K. Despite the impressive predicted mixer characteristics, experimental realization of TACIT mixers have been difficult particularly due to challenges in fabricating reliable dual-gate structure necessary for frequency tuning of TACIT mixers. Numerous attempts have been made to fabricate the dual-gate structures using dual metal gates [47, 48, 49] and using doped QW layers [42, 44, 46] or doped GaAs layers [50] as back-gate layers. However, previous TACIT devices from these fabrication attempts had either unresponsive or leaky back gates, resulting in poor gate control and hence poor device performance. As a result, THz mixing capability of TACIT mixers had never been confirmed experimentally.

In this work, using an advanced flip-chip technique that we developed in-house, we

[13]Typically, the RF channel is matched to 80 Ω, which is a typical value for a planar THz antenna, and the IF channel is matched to 50 Ω, which is the typical input impedance of a first IF amplifier.

[14]The quantum limit here refers to the fundamental limit on the sensitivity of a heterodyne receiver due to the Uncertainty principle. In terms of numbers, we have $T_{REC} > h\nu/k_B \sim 48K/THz$ where h is the Plank constant and k_B is the Boltzmann constant.

successfully fabricate two versions of prototype TACIT mixers and demonstrate the THz mixing capability in TACIT mixers for the first time. Furthermore, we provide characterization results for several other features of TACIT mixers, including tunability in detection frequency, antenna coupling for intersubband transitions, capacitive coupling for IF read-out, and noise power behavior, that are useful for further optimization and development of TACIT mixers in the future.

In the first prototype TACIT mixer integrated with a single slot antenna, we demonstrate the tunability in the detection frequency (2.52–3.44 THz) with relatively small (< 5 V) DC bias voltages, as well as the heterodyne detection (mixing) capability at 60 K with a wide IF bandwidth (~ 6 GHz). The observed tunability in the direct detection responses is consistent with the response model based on intersubband transitions. In the second prototype TACIT mixers integrated with a modified, broadband bow-tie antenna, we explore capacitive coupling for the read-out of the device IF response and investigate the dependence of the noise power on various bias conditions of the device. In addition, we demonstrate tunability in both the direct detection and heterodyne detection consistent with the results from the first prototype TACIT mixer and with our model responses.

In both prototype devices, we observed unexpectedly large conversion losses, and the mixer noise temperature, conversion loss, and required LO power were not measured. We attribute these large losses to poor radiation efficiency of the antenna structures caused by impedance mismatch and non-optimal radiation patterns, as well as to to possible degradation in the IF response caused by diffusion and ballistic cooling of the high-mobility 2DEG at low temperatures. To address these issues, we will briefly discuss our plans for designing more optimized antenna structures and employing a different read-out mechanism based on the thermoelectric effect of high-mobility 2DEGs for future iterations of TACIT mixers.

The remainder of this dissertation is organized as follows. In Chapter 2, we will discuss the device operation in detail and provide modeling results for the device. In Chapter 3, we will describe the advanced flip-chip technique that allows for the fabrication of reliable dual-gate structures required for TACIT mixers. In Chapter 4, we will introduce the first prototype TACIT device integrated with a single-slot antenna, and provide characterization results for the tunability and THz mixing capability of the device. In Chapter 5, we will introduce the second prototype TACIT device integrated with a bow-tie antenna, and provide characterization results for the direct detection and heterodyne measurements, as well as other measurement results on the capacitive IF read-out and noise power behavior. Finally, in Chapter 6, we will review some of the limitations identified in the two prototype devices, including the poor conversion efficiency, and discuss our plans to address these issues for further development and optimization of TACIT mixers in the future.

Figure 1.4: Capacitively-coupled prototype TACIT mixer on a penny (it is a real device now!) [51].

Chapter 2

Device Operation and Modeling Results

For any semiconductor device, understanding and modeling the device operation is important for its design, evaluation, and optimization. For TACIT mixers, however, this can be challenging due to the novelty in the device concept and the relative lack of experimental verification on the device operation. In addition, the tunability in TACIT mixers further complicates numerical evaluation of the device models as the device material parameters (e.g. charge density and mobility) required for the modeling are also highly tunable. Despite these challenges, elementary models can be developed that are useful for the device design and for the evaluation of the device performance. In this chapter, we first discuss the device operation of TACIT mixers and then provide modeling results for various device characteristics including the detection frequency, RF and IF impedances, and mixer characteristics.

2.1 Device Operation

2-dimensional Electron Gas in Quantum Well

TACIT mixers are based on high-mobility 2-dimensional electron gas (2DEG) confined in single GaAs/AlGaAs quantum-well (QW) heterostructures. Advanced molecular beam epitaxy (MBE) techniques, along with the good lattice matching between GaAs and AlGaAs, allows for the growth of very clean heterostructure systems in which the two semiconductors with different band gaps are stacked together to form potential well at their interfaces. For the prototype TACIT mixers described in this work, we use a single 40-nm square GaAs/AlGaAs QW (see Figure 2.1 for a simplified structure). Electrons, provided with delta-doping technique, are trapped in the potential well in the GaAs layer, forming a 2-dimensional electron gas (2DEG) system, in which the electrons are free to move in the x- and y- directions (in-plane directions of the 2DEG) but not along the z-direction (the growth direction of the QW). The delta-doping technique allows for the doping layers to be placed outside the GaAs layer (conduction channel), making it possible for the 2DEG to have very high-mobility ($> 10^6$ cm^2/Vs) at low temperatures.[1]

The low-dimensionality for the 2DEG is a direct consequence of the quantization of the energy levels along the z-direction due to the confinement. This is most straightforward to see if we model the QW as an infinite square well, in which the energy eigenvalue E_n is given by

$$E_n\left(k_{xy}\right) = \frac{\hbar^2}{2m^*}\left(\pi^2 n^2/t^2 + k_{xy}^2\right) \tag{2.1}$$

where k_{xy} is the in-plane wavevector, $\hbar$ is the reduced Planck's constant, m^* is the effective mass in the well, n is a positive integer, t is the thickness of the well.[2] As we can

[1] This is because the delta-doping significantly reduces the impurity scattering for a 2DEG. For detailed discussion on various scattering mechanisms for the high-mobility 2DEG, please refer to [52] or [53].

[2] The derivation for this is trivial and shown in [40] and in [39] in greater detail.

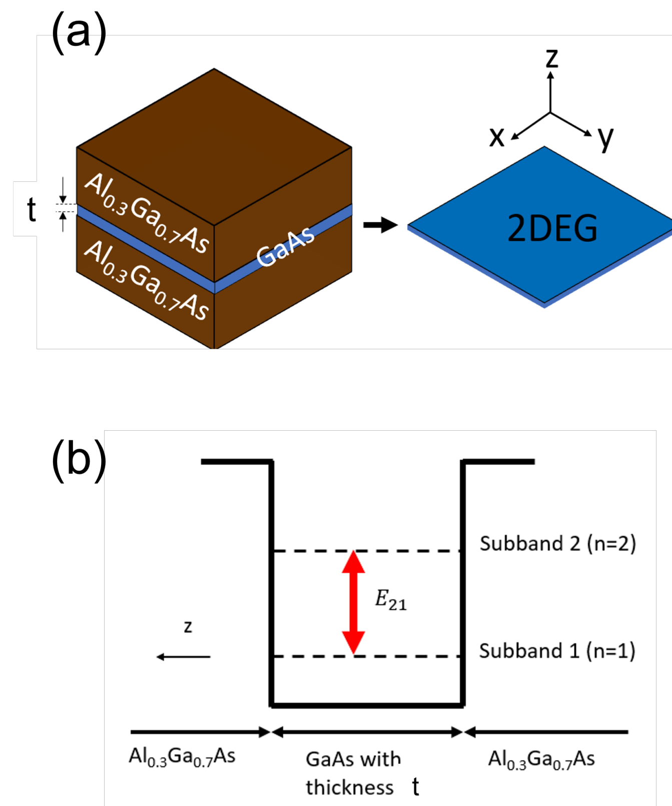

Figure 2.1: Schematics for (a) simplified QW structure for TACIT mixers and (b) simplified energy diagram for the square QW. For the prototype TACIT mixers in this work, we have $t = 40$ nm.

see in Eq. 2.1, the potential well creates quantized energy states ("subbands") with the positive integer n within the conduction band. For a typical 2DEG system, the doping density is engineered such that only the first subband energy is occupied, but transitions to higher subbands (so-called intersubband transitions) are also possible. As we can see in Eq.2.1, the energy spacing between these subbands can be engineered by adjusting the QW thickness t to be in the order of 10 meV, which falls in the THz range.

RF Absorption

For TACIT mixers, we engineer the thickness of the well t such that the energy spacing between the first ($n = 1$) and the second ($n = 2$) subbands $E_{21} = \frac{3\hbar^2\pi^2}{2m^*t^2}$ to be near the absorption energy required for the target intersubband absorption frequency, or the detection frequency, $\nu_{ISBT} \sim E_{21}/h$ (see Figure 2.1(b)).[3] For the prototype TACIT mixers in this work, we chose $t = 40$ nm such that we have $\nu_{ISBT} \sim E_{21}/h = 2.5$ THz. We also engineer the doping density such that only the first subband is occupied for more efficient THz absorption via intersubband transition. The RF impedance associated with the intersubband transition can be close to the impedance of a typical planar antenna structure, and a high predicted RF coupling efficiency $\alpha_{RF} > 80\%$ can be achieved at THz frequencies for TACIT mixers [41].

In addition to the high absorption efficiency at THz frequencies, RF absorption via intersubband transition also offers tunability in the detection frequency. The intersubband absorption frequency, primarily determined by the well width t, can be further tuned by applying an external DC electric field perpendicular to the 2DEG plane (along the growth direction of the QW) or by varying the charge density in the well. The DC electric field tilts the well potential and modifies the energy spacing between the subbands

[3] Note that the absorption frequency ν_{ISBT} doesn't exactly match the energy spacing frequency $\nu_{21} = E_{21}/h$ for various shifts in the absorption frequency including many-body effects [39].

via the DC Stark shifts (see Figure 2.2 for the illustrations describing this effect). At a given charge density, the energy level for the first subband is lowered with the tilted QW potential with the applied DC electric field, resulting in an increase in the intersubband energy spacing between the two subbands.[4] In addition, with an increase in the charge density in the QW, the well potential as well as the energy levels for the two subbands can be modified, also resulting in the shifts in the intersubband absorption frequency (see Figure 2.3). The intersubband absorption frequency is further affected by collective effects of the charge density (e.g. depolarization and exciton shifts), causing additional shifts in the intersubband absorption frequency ν_{ISBT}.[5]

While the intersubband absorption frequency depends both on the DC electric field and the charge density in the well, and hence the independent control of both quantities is important for its precise tuning, the effect of the DC electric field on the absorption frequency is dominant compared to the small shifts associated with the charge density. As a result, the absorption frequency can be mostly tuned by varying the DC electric field at a fixed charge density. For example, for a 40-nm single GaAs/AlGaAs QW, the absorption frequency for the intersubband transition between the first and the second subbands can be tuned in a wide range (2–5 THz) with relatively small DC electric fields (in the order of 10 kV/cm) at a fixed charge density. Such wide tunability has been already observed experimentally in a 40-nm square GaAs/AlGaAs QW structure previously studied in our group [54] and is also consistent with the modeling results on the absorption frequency.[6]

[4]This dependence is symmetric about the zero electric field and results in roughly parabolic "tuning curves" for TACIT mixers (that is, the intersubband absorption frequency shows roughly parabolic dependence on the applied electric field).

[5]For more details on the physical origin of these various shifts in the intersubband absorption frequency, refer to [39].

[6]This will be one of the modeling results provided in the next section. Also see Appendix B for more details on the calculation.

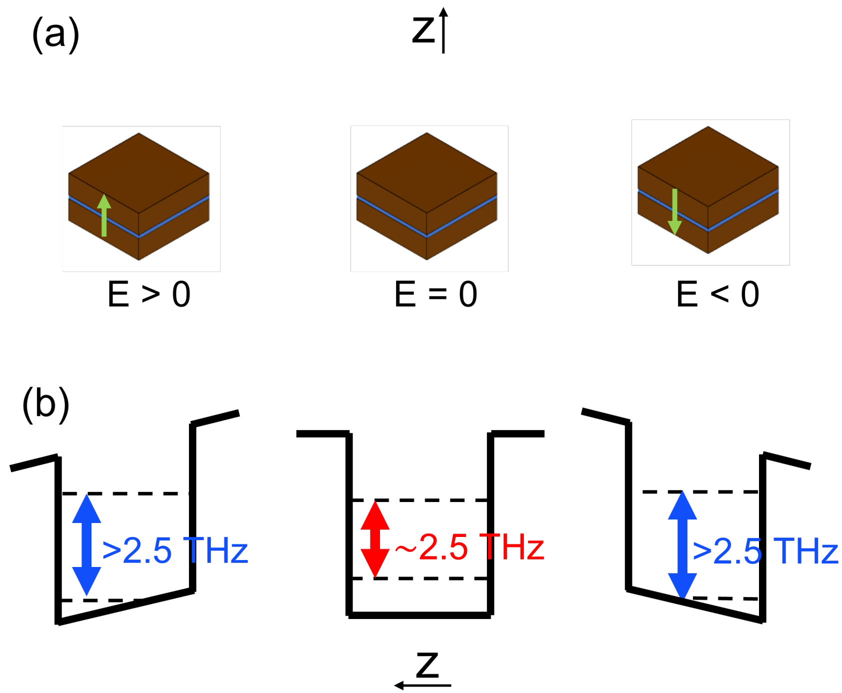

Figure 2.2: Schematics illustrating the change in the subband energy spacing with DC electric fields (via the DC Stark shift). Schematics in (a) show the directions for the DC electric field in real space and schematics in (b) show energy diagrams at corresponding DC electric fields.

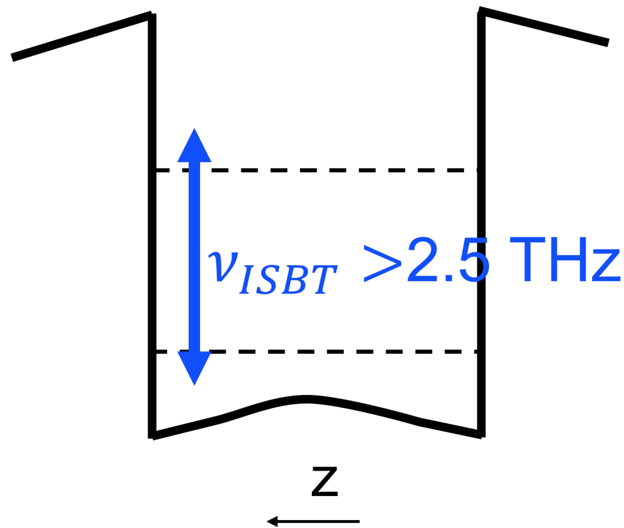

Figure 2.3: Schematic illustrating the effect of increasing charge density on the well potential and on the intersubband absorption frequency.

IF Response

After the RF absorption via intersubband transitions, the IF response of TACIT mixers comes from the fast, strong temperature dependence of the mobility of a high-mobility 2DEG. Such bolometric response causes a rapid, significant change in the in-plane resistance of the 2DEG, resulting in the IF response fast enough to follow the IF frequency in the GHz range.[7] In TACIT mixers, the RF and LO absorption occurs in a small (typically 5μm $\times 5\mu$m) patch of the 2DEG referred to as the active region. After the intersubband absorption of THz RF and LO, the electrons in the active region can thermalize quickly and can heat up, with the electron temperature raised above the lattice temperature.[8] Because the mobility of the high-mobility 2DEG is a strong function of the electron temperature (see Figure 2.4) [53], the change in the electron temperature can in turn strongly affect the in-plane resistance of the device.[9] Such change in the in-plane resistance of the device can be easily monitored and registered with a small (in the order of μA) constant DC bias current (see the inset of Figure 2.4) applied in the in-plane direction of the 2DEG. Furthermore, the bolometric response in the 2DEG is fast, with the energy relaxation time constant in the order of 10 ps at 20–60 K[10], allowing for the electron heating to be modulated at the GHz range for the IF response.

[7] While there may be more than one physical mechanisms causing this change in the in-plane resistance after intersubband absorption, such as the mobility difference between the two subbands, we will mostly focus on the bolometric IF response for this dissertation. For other possible types of IF responses, refer to [44, 45, 46].

[8] This is because of the small heat capacity for the electrons and the weak thermal coupling between the electrons and the lattice. For a typical active region area $A = 25\mu\text{m}^2$ and charge density $n_s \sim 2 \times 10^{11}$ cm^{-2}, we have the heat capacity $C_e \sim N_s k_B \sim 6.9 \times 10^{-19}$ J/K. Typical values for the thermal conductance are in the order of 100 nW/K near the operating temperature of TACIT mixers (20–60 K).

[9] In terms of temperature coefficient of resistance $\alpha_{TCR} = (dR_s/dT)/R_s$, we have $\alpha_{TCR} \sim 0.03$ K^{-1}, corresponding to roughly 30 % change in R_s with 10 K of electron heating.

[10] Assuming phonon-cooling, we have the energy relaxation time constant $\tau_e = C_e/G \sim 7$ ps, which yields the -3dB bandwidth $f_{-3dB} = 1/(2\pi\tau_e)$ in the order of 10 GHz.

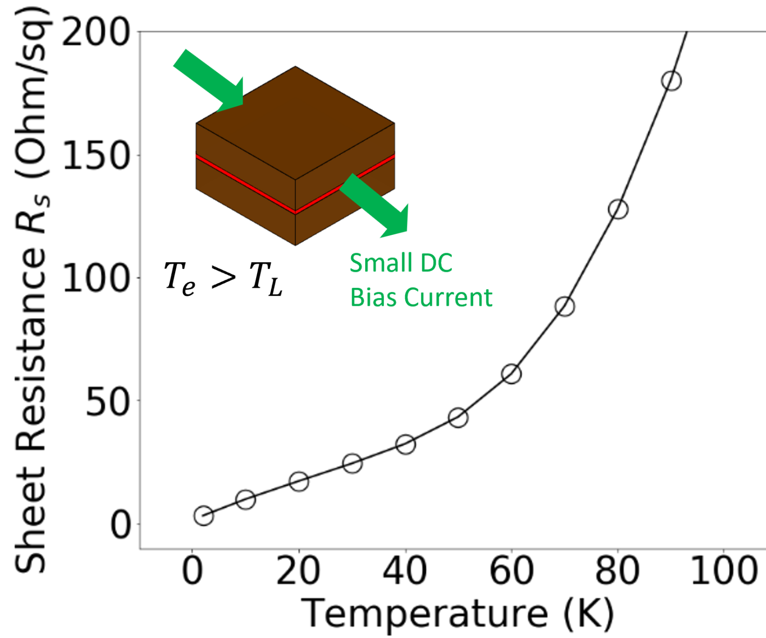

Figure 2.4: Strong bolometric response observed in the in-plane resistance of a 2DEG confined in a 40-nm GaAs/AlGaAs quantum well. The plot shows the sheet resistance of the 2DEG measured in a Hall bar device. The inset shows a schematic for a square sheet of the 2DEG indicating the in-plane direction for the constant current biasing.

Device Operation - Review

Before we move on to the modeling results, we review the device operation for TACIT mixers again using the schematic for the cross-section of a TACIT mixer shown in Figure 2.5. The schematic illustrates the four-terminal geometry of TACIT mixers, with the dual-gate structure consisting of two Schottky gates (top and bottom gates) that enclose the active region of the device (where the RF absorption occurs) and the two Ohmic contacts (source and drain) that couple out the IF response in the in-plane resistance of the 2DEG. The dual-gate structure is integrated with a THz antenna that orients the THz electric fields of RF and LO along the growth direction of the QW to satisfy the selection rule for the intersubband absorption [53, 40, 39].

The operation of TACIT mixers begins with the tuning of the detection frequency ν_{ISBT} by independently controlling the charge density and the DC electric field (along the

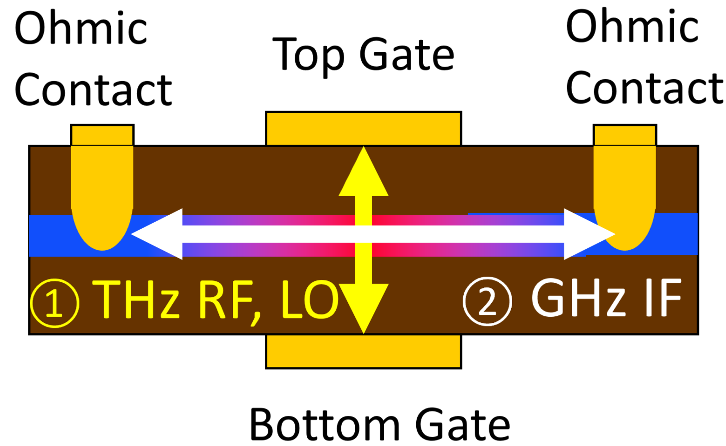

Figure 2.5: Schematic for the cross-section of a TACIT mixer.

growth direction of the QW) in the active region. To do this, DC voltages are applied to the top and the bottom gates (V_T and V_B) in terms of the sum and the difference voltages ($V_{Sum} = V_T + V_B$ and $V_{Diff} = V_T - V_B$) that control the charge density and the DC electric field, respectively.[11] The optimal DC bias conditions for these voltages can be determined experimentally, by mapping out the "tuning curves" by measuring the device response to monochromatic THz radiation as a function of V_{Sum} and V_{Diff} (that is, as a function of the DC electric field and the charge density). However, numerical modeling for these tuning curves (or numerically calculating the intersubband absorption frequency as a function of the DC electric field over different charge densities in the well) is also possible, and useful for the initial guessing of the optimal bias points as well as for evaluating the absorption behavior in the device; this will be our first topic in the next section on modeling results.

Once we tune the detection frequency of TACIT mixers near the target THz frequency for the RF and LO, the electrons in the active region absorb the THz energy and can

[11] The sum and the difference voltages are related to the charge density and the DC electric field based on a simple parallel-plate capacitor model and will be introduced in detail in the next section.

heat up rapidly, with the electron temperature modulated at the IF frequency in the GHz range. This IF response is then coupled out from the source-drain channel through the two Ohmic contacts (see Figure 2.5). At these stages, impedance matching for the RF and the IF channels is important in minimizing unwanted loss for the IF response. As we briefly discussed in Chapter 1, the use of intersubband transition naturally separates the RF absorption channel from the IF read-out channel for TACIT mixers (Figure 2.5), and the RF impedance and the IF impedance for TACIT mixers can be individually optimized to match the relevant impedance values (typically 80 Ω for the RF impedance and 50 Ω for the IF impedance). For both the RF and the IF impedances of TACIT mixers, simple equivalent-circuit models with lumped elements can be introduced; the modeling results for the RF and the IF impedances will be another topic in the next section.

Lastly, the predicted high RF coupling efficiency and the IF response from strong, fast bolometric response in TACIT mixers predict that the TACIT mixers can be very sensitive THz mixers, with SSB mixer noise temperature of $\sim 1,000$ K, operating at relatively high temperatures (20–60 K) with a small ($< 1\mu$W) required LO power. These mixer characteristics are evaluated based on hot-electron bolometer mixer theory [55, 56, 57]; these modeling results will be our last topic in the next section.

2.2 Modeling Results

Detection Frequency

The detection frequency of TACIT mixers is determined by the absorption frequency for the intersubband transition between the first and the second subbands for the 2DEG confined in single QWs. The intersubband absorption frequency is primarily determined

by the width of the quantum well, and, for TACIT mixers described in this work, we use a 40-nm square GaAs/AlGaAs quantum well, in which the intersubband absorption frequency is near 2.5 THz in the absence of the external electric field at a typical charge density of $n_s \sim 2.0 \times 10^{11}$ cm^{-2} at low temperatures. As described in the previous section of the chapter, this intersubband absorption frequency can be further tuned in-situ by applying an external electric field perpendicular to the 2DEG plane (along the growth direction of the quantum well) and by varying the charge density. The intersubband absorption frequency for a given electric field, charge density and temperature can be numerically calculated by self-consistently solving the Schrödinger equation and Poisson's equation for a given QW structure, taking into account Fermi-Dirac statistics, and including the effect of the electrostatic potential from the charge density (self-consistent Hartree potential), many-body effects on the energy of the 2DEG (the exchange and correlation energies), and collective effects on the absorption (depolarization and exciton shifts) [39].

For the calculation of the intersubband absorption frequency, we use a home-built QW solver that self-consistently solves Schrödinger equation and Poisson's equation.[12] Figure 2.6 shows the calculated intersubband absorption frequency for the intersubband transition between the first and the second subband for a 40-nm QW at 20 K and 60 K. This absorption frequency is the detection frequency for TACIT mixers based on a 40-nm square GaAs/AlGaAs QW, and each curve calculated at a given charge density serves as a tuning curve for the TACIT mixers at a given charge density. The plots show that these tuning curves at various charge densities show wide tunability (2–5 THz) in the detection frequency. For each curve, the symmetric quasi-parabolic dependence is a result of the DC Stark shift (induced with the DC electric field) on the intersubband energy spacing. At 20 K, near the zero DC electric field, there are competing effects of

[12] See Appendix B for additional information.

the blue shifts due to depolarization shifts [39, 58] and the red shifts due to other effects on the absorption frequency [39]. The effect of the blue shifts seems to be more dominant at lower temperatures (for example, see the calculation result for 2.3 K in Appendix B) and becomes less important for higher temperatures (see the result for 60 K in Figure 2.6) and for the DC electric fields away from the zero field where the subband energy spacing becomes a lot greater than the effect of the depolarization shifts.

As we discussed earlier, we control the charge density in the well and the DC electric field (applied along the growth direction of a QW) by applying DC voltage biases to the top and the bottom gates (V_T and V_B). This is best done in terms of the sum and difference voltages ($V_{Sum} = V_T + V_B$ and $V_{Diff} = V_T - V_B$) which can be related to the charge density n_s and the DC electric field E based on a parallel-plate capacitor model:

$$n_s = n_0 + \frac{c}{e}(V_T + V_B) \tag{2.2}$$

and

$$E = \frac{1}{d}(V_T - V_B) \tag{2.3}$$

where n_0 is the intrinsic charge density in the well, c is the capacitance per unit area between each gate and the 2DEG, e is the elementary charge, and d is the distance between the top and the bottom gates. Using V_{Sum} and V_{Diff} allows us to independently control n_s and E and achieve robust gating operation (such as sweeping E while fixing n_s) possible for TACIT mixers.

Based on Eq. 2.2 and Eq. 2.3, we can estimate how much DC voltage biases are necessary to achieve the tunability shown in Figure 2.6 in TACIT mixers. For our 40-nm QW structure used for the prototype TACIT mixers in this work, we have $d \sim 660$ nm, and we need the difference voltage $V_{Diff} = \pm 1.3$ V to achieve the maximum electric field

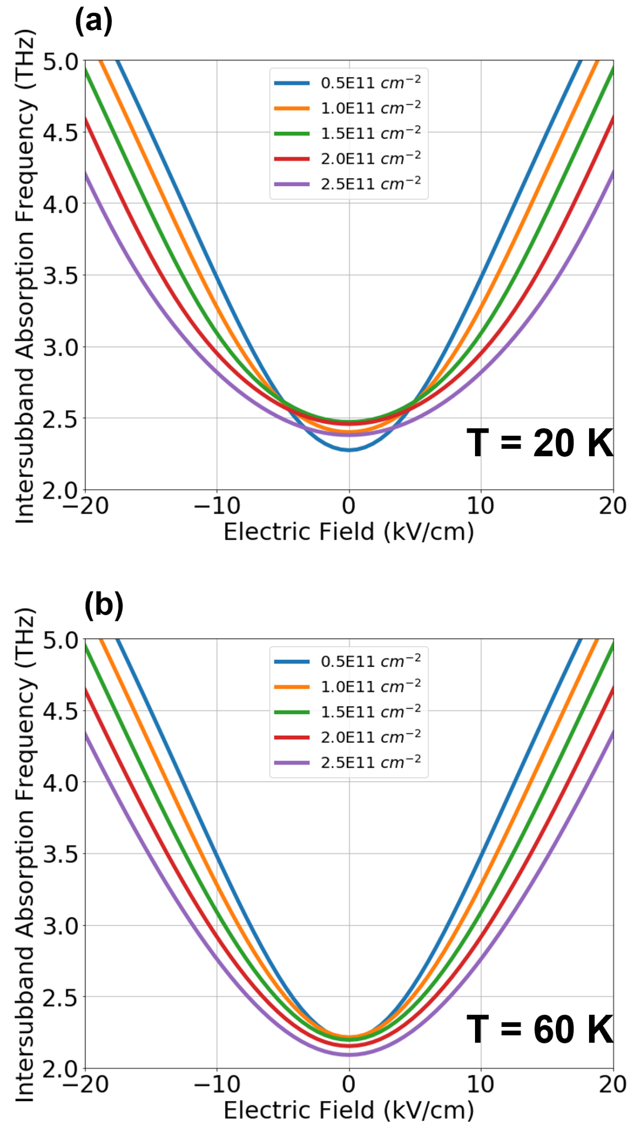

Figure 2.6: Calculated intersubband absorption frequency for the transition between the first and the second subbands in a 40-nm single, square GaAs/AlGaAs quantum well at 20 K (a) and at 60 K (b). This absorption frequency is equivalent to the detection frequency of a TACIT mixer. Each "tuning curve" shows how the detection frequency varies with the DC electric field at a given charge density indicated in the legend.

value $E_{max} = \pm 20$ kV/cm (shown in Figure 2.6) based on Eq. 2.3. For the charge density, since we have the capacitance per unit area $c = \epsilon_r \epsilon_0 / d$, we have $c/e \sim 2.1 \times 10^{11}$ cm^{-2}/V and a typical intrinsic charge density of $n_0 \sim 2.0 \times 10^{11}$ cm^{-2}, varying the sum voltage (V_{Sum}) from -1 V to 0.4 V is sufficient to tune the charge density to the values shown in Figure 2.6. These numbers suggest that relatively small DC voltage biases ($|V_{T(B)}| < 1.5$ V) can be used to achieve the tunability in Figure 2.6.

RF Impedance

The RF impedance for TACIT mixers can be calculated based on the impedance model for intersubband absorption first worked out by Sherwin et al. [41]. In [41], the RF impedance for TACIT mixers (that is, the impedance of the active region of TACIT mixers seen by THz antenna structures) is calculated by considering a THz current oscillating between the top gate and the bottom gate (see Figure 2.7) and the corresponding voltage drop caused by the polarization of the 2DEG. The expression for the RF impedance $Z_{RF}(\omega)$ is then given by

$$Z_{RF}(\omega) = \frac{1}{i\omega\epsilon_r\epsilon_0 A}\left(d - \frac{\chi_{2DEG}(\omega)}{\epsilon\epsilon_0}\right) \tag{2.4}$$

where ω is the angular frequency of incoming radiation, ϵ_r is the dielectric constant for GaAs, ϵ_0 is the permittivity of free space, A is the area of the metal gates, d is the distance between the top gate and the bottom gate, and $\chi_{2DEG}(\omega)$ is the 2D susceptibility of the 2DEG associated with intersubband transitions in QWs.

For TACIT mixers, the 2D susceptibility $\chi_{2DEG}(\omega)$ is associated with the intersubband transition between the first and the second subbands. The theory for $\chi_{2DEG}(\omega)$ [52, 58] takes into account the effects of the dynamic screening and the electron-electron interaction through two simple parameters, the absorption frequency ω^* for the intersub-

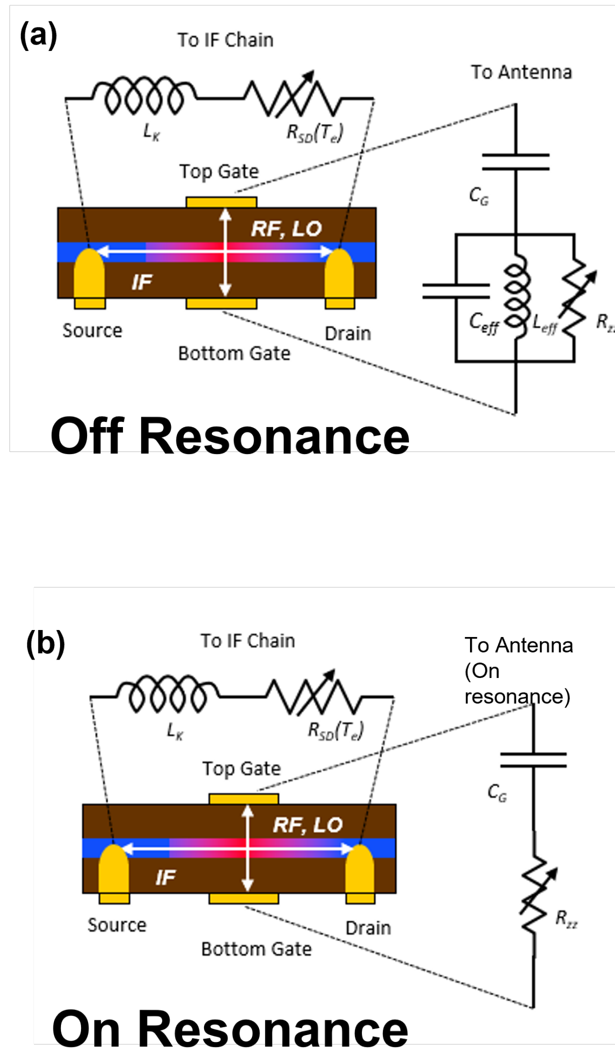

Figure 2.7: Equivalent circuit models for the RF channel and the IF channel in TACIT mixers (a) at off-resonance conditions and (b) on-resonance conditions. Reproduced from [59], with the permission of AIP Publishing.

band transition and the oscillator strength $f_{12} = 2m^* z_{12}^2 E_{12}/\hbar^2$ where m^* is the effective mass of an electron in GaAs, z_{12} is the matrix element of the position operator applied on the wavefunctions for the first and the second subbands, E_{12} is the energy spacing between the subbands, and $\hbar$ is the reduced Planck's constant. The expression for $\chi_{2DEG}(\omega)$ is given in [41] and [52]:

$$\chi_{2DEG}(\omega) = \frac{N_s e^2 f_{12} n(T_e)}{m^*} \frac{1}{{\omega^*}^2 - \omega^2 + i2\omega\Gamma} \tag{2.5}$$

where N_s is the total sheet charge density, e is the electron charge, $n(T_e)$ is the normalized population difference $n(T_e) = \frac{N_1(T_e)-N_2(T_e)}{N_s}$ where $N_{1(2)}(T_e)$ is the population of the first (second) subband at an electron temperature T_e, and $\Gamma/2\pi$ is the HWHM of the intersubband absorption.

With this expression for $\chi_{2DEG}(\omega)$, the device RF impedance $Z_{RF}(\omega)$ can be modelled with an equivalent circuit of a capacitor with the geometric capacitance $C_G = \epsilon_r \epsilon_0 A/d$ (formed by the two gates) in series with an effective resonator circuit that represents the intersubband absorption (Figure 2.7). At off-resonance condition (see Figure 2.7(a)), the resonator circuit consists of an inductive element with the effective inductance L_{eff}, a capacitive element with the effective capacitance C_{eff}, and a resistor with the resistance R_{zz} presented to the current oscillating between the top gate and the bottom gate. On resonance, the effective inductance tuned out the effective capacitance, and the RF impedance can be represented by a simpler circuit of R_{zz} connected in series with C_G (see Figure 2.7(b)). It is important to note that the resistance R_{zz} is different from the source-drain resistance $R_{SD}(T_e)$ (this is responsible for the IF response of TACIT mixers).

When the frequency of the incoming radiation ω matches the absorption frequency for the intersubband absorption ω^* ($\omega = \omega^*$), the reactive elements, C_{eff} and L_{eff}, in

the effective resonator circuit (see Figure 2.7(a)) tune each other out, and the resonator impedance become purely resistive (see Figure 2.7(b)). Hence, on resonance, the RF impedance $Z(\omega = \omega^*)$ can be modelled by a capacitor with the geometric capacitance C_G in series with a resistor with the resistance R_{zz}:

$$Z_{RF}(\omega^*) = \frac{d}{i\omega^* \epsilon\epsilon_0 A} + \frac{N_s e^2 f_{12} n(T_e)}{\epsilon^2 \epsilon_0^2 A m^* \omega^{*2} 2\Gamma} = \frac{1}{i\omega^* C_G} + R_{zz} \tag{2.6}$$

where R_{zz} is the effective resistance to the current oscillating between the top gate and the bottom gate. In a real device, the resistance R_{zz} is tunable as the charge density in the active region can be varied by applying small DC voltage biases to the top and bottom gates. With a combination of optimized design parameters (the gate metal area A and the gate distance d) and the tunable R_{zz}, the RF impedance of a TACIT mixer can be matched very closely to the antenna impedance for a high coupling efficiency, with $\alpha > 80\%$ [41].

With Eq. 2.6, we can estimate the RF impedance for one of the prototype TACIT devices in this work (for a resistively-coupled prototype TACIT mixer that will be introduced in Chapter 4). The device has a gate area $A = 20$ μm^2 and the gate distance $d =$ 660 nm, and the charge density is varied in the range practically achievable in this prototype device (0.5×10^{11} cm^{-2} $< N_s < 2.5 \times 10^{11}$ cm^{-2}). For the calculation, the effective oscillator strength $f_{12}n(T_e)$ was calculated for each charge density by numerically solving the Schrodinger's equation and the Poisson's equation self-consistently using our home-built QW solver introduced earlier in this chapter. The HWHM for the intersubband transition was assumed to be 33 GHz ($\Gamma/2\pi = 33$ GHz) based on [41]. On resonance at 2.52 THz, the real part of the RF impedance for the prototype device is estimated to be 6–11 Ω in the given range for the charge density, and the imaginary part is estimated to be -18Ω. At 3.11 THz, the real part is 5–8 Ω and the imaginary part is -15Ω. The

non-zero values for the imaginary part are due to the geometric capacitance and can be tuned out with an inductive element in the antenna circuit in a future device. While the values for R_{zz} in this prototype device are much smaller than typical values (50-70 ohm) for the resistive impedance of a planar antenna on a Si substrate, further optimization in the design parameters A and d can make the R_{zz} to be close to 50-70 Ω (see Figure 2.8). Note that decreasing the gate area of the device leads to an increase in the capacitive component in the device RF impedance as well, which may require the integration of a tuning circuit (with inductive element) with THz antenna structures in these optimized TACIT mixers for more efficient RF coupling.

Before we move on, it is worth providing general expression for the device RF impedance $Z_{RF}(\omega) = R_{RF} + iX_{RF}$ for future reference later in the dissertation. This can be simply derived by plugging Eq. 2.5 to Eq. 2.4 and reduces to Eq. 2.6 with $\omega = \omega^*$:

$$R_{RF} = \frac{e^2}{\epsilon_r^2 \epsilon_0^2 m^*} \frac{1}{A} \frac{2\Gamma N_S f_{12} n(T)}{\left(\omega^{*2} - \omega^2\right)^2 + 4\omega^2\Gamma^2} \tag{2.7}$$

and

$$X_{RF} = -\frac{1}{\epsilon_r \epsilon_0 \omega} \frac{d}{A} + \frac{1}{\epsilon^2 \epsilon_0^2 \omega A} \frac{e^2 N_s f_{12} n(T)}{m^*} \frac{\omega^{*2} - \omega^2}{\left(\omega^{*2} - \omega^2\right)^2 + 4\omega^2\Gamma^2}. \tag{2.8}$$

As in the calculation result shown in Figure 2.8, the numerical values for the real and imaginary components of the device RF impedance can be calculated once the absorption frequency and the effective oscillator strength are calculated and some reasonable value is assumed for the HWHM. Also, the calculate RF impedance can be used to calculate the RF impedance matching effiency, useful for the evaluation of the absorption behavior of TACIT mixers. In Chapter 4, we will use the calculation results based on Eq. 2.7 and Eq. 2.8 to simulate model responses for the direct detection results measured in the resistively-coupled TACIT mixers.

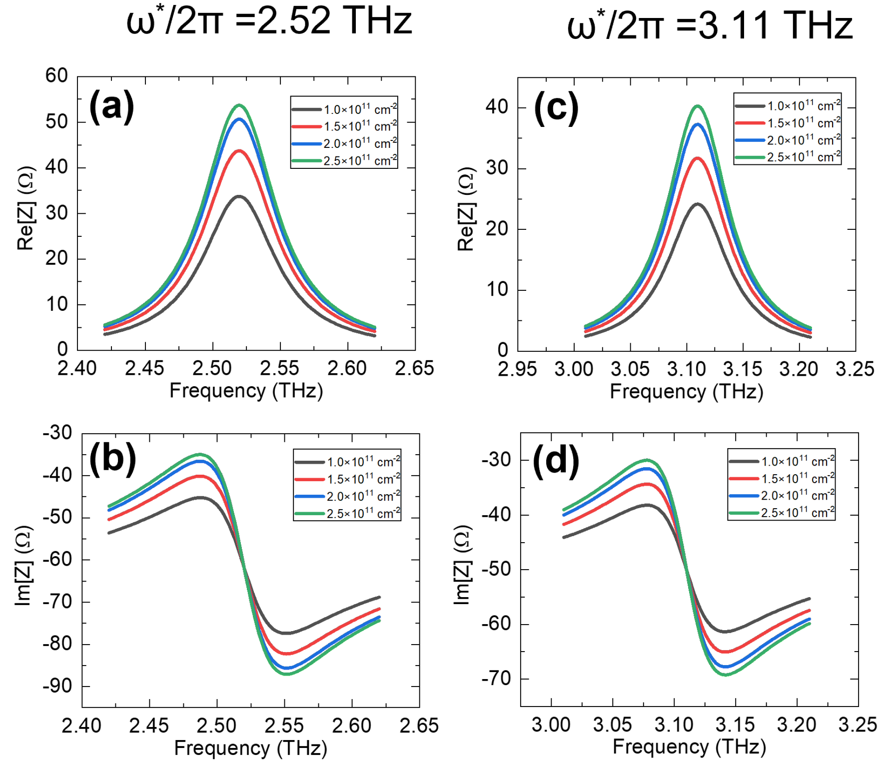

Figure 2.8: Calculated RF impedance of an optimized TACIT mixer with a gate area of $A = 4\ \mu\text{m}^2$ and a gate distance of $d = 450$ nm when the device is tuned to near 2.52 THz (subplots (a) and (b)) and near 3.11 THz (subplots (c) and (d)). For the calculation, the effective oscillator strength $f_{12}n(T_e)$ was numerically calculated for each charge density at the electron temperature of 85 K, which is the estimated temperature at the optimal bias point at the lattice temperature of 60 K. $\Gamma/2\pi =$ 33 GHz was used. With the optimization of the design parameters A and d, the resistive part of the RF impedance can be designed to be near 50-70 Ω, which are the typical values for the resistive impedance of planar antenna structures on a Si substrate. The large capacitive component in the device RF impedance may require an inductive tuning circuit in the antenna structure for better impedance matching to the antenna. Reproduced from [59], with the permission of AIP Publishing.

IF Impedance

We take a similar equivalent-circuit approach to model the IF impedance for TACIT mixers. In an ideal TACIT mixer where the device consists of a single square of 2DEG, the device IF impedance can be simply represented by a variable resistor in series with an inductor[13] as depicted in Figure 2.7. However, in real devices (as we will see in Chapter 4 and Chapter 5), the active region must be connected with extra 2DEG contacts for DC biasing and IF read-out (see Figure 2.9(a)). These 2DEG contacts add parasitic impedance to the overall IF impedance of TACIT mixers, and, for more realistic modeling of the IF impedance, the effect of the 2DEG contacts also has to be included in our equivalent-circuit model (see Figure 2.9(b)). While these 2DEG contacts can add significant parasitic impedances to the IF impedance, we will show that most of these parasitic impedances can be tuned out by capacitively coupling out the IF response from the 2DEG at the IF frequency range of interest (1–2 GHz).

In modelling the device IF impedance, we will use an equivalent circuit model based on lumped elements. Note that such lumped element model is valid only when the relevant length scale (the length of a TACIT mixer for our case) is sufficiently smaller than the relevant wavelength (of 1–2 GHz in our case) and when the frequency range of interest is within the frequency limits set by either energy relaxation time or the momentum relaxation time of the 2DEG. For the IF impedance at higher frequencies above these frequency limits, one needs to use transmission line model that accounts for the ballistic transport of the 2DEG [37], with additional frequency dependence associated with the fast energy relaxation. In our case, the device length (< 1 mm) is a lot shorter than the relevant wavelength for 1–2 GHz (~ 79 mm for 1 GHz in GaAs). The frequency range (1–2 GHz) is also well within the frequency limits set by the typical values for the energy

[13] This is from the kinetic inductance L_k of 2DEG given by $L_k = m^*/(n_s e^2)$. For a charge density of $\sim 2 \times 10^{11}$ cm^{-2}, the inductance is ~ 1 nH/$\square$.

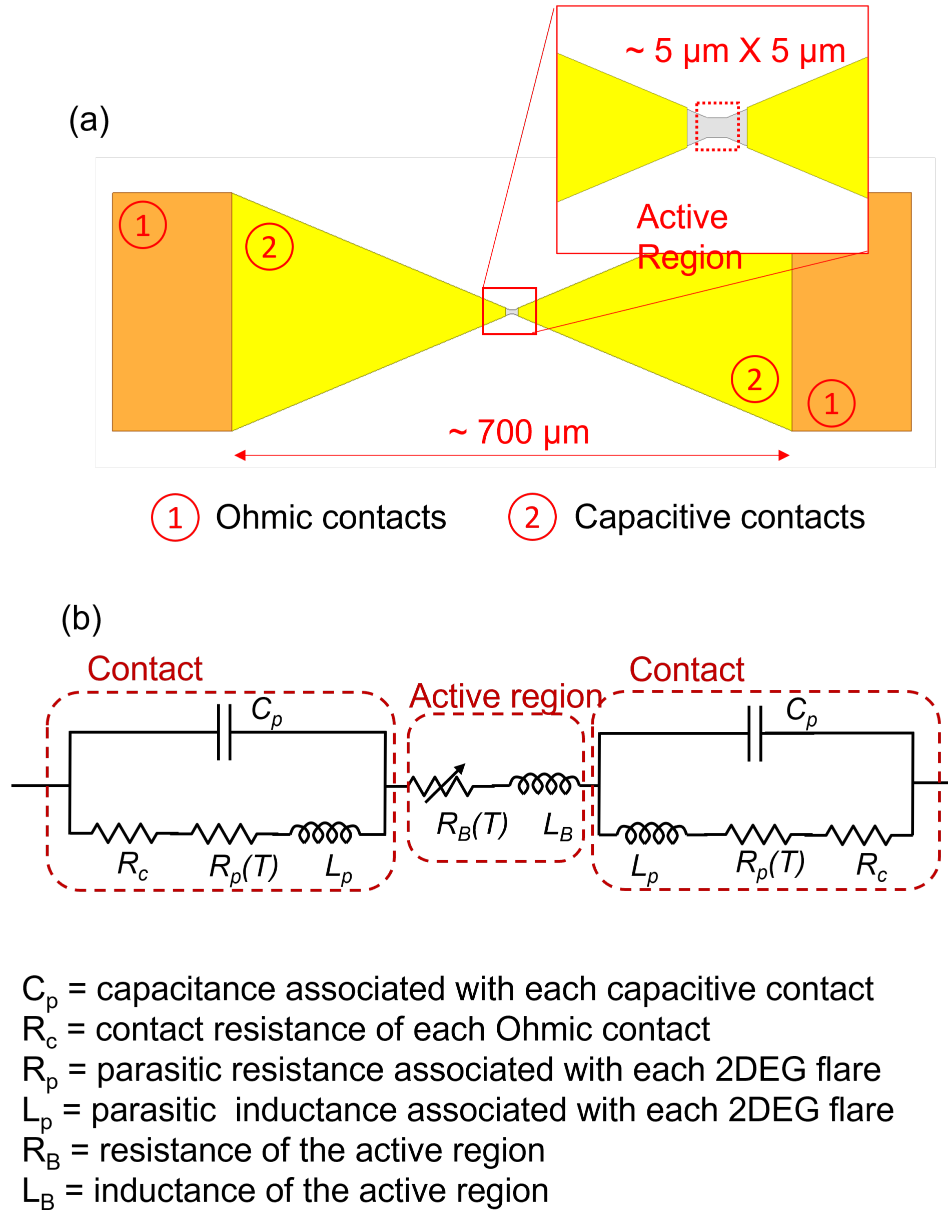

Figure 2.9: IF impedance model for TACIT mixers. (a) 2DEG mesa design for a capacitively-coupled TACIT mixer. The inset shows the active region where THz radiation is coupled to (the THz antenna structure is not shown in this schematics). Here, two Ohmic contacts (circled 1) are used to apply constant DC bias to the source-drain channel. The capacitive contacts (circled 2) are Schottky contacts on the 2DEG contact area that capacitively couple out the IF response from the 2DEG. (b) Equivalent-circuit model for the IF impedance of a capacitively-coupled TACIT mixer. The capacitive contacts add a capacitor in parallel with the 2DEG contacts that are mostly resistive and inductive to tune out the parasitic contact impedance, significantly reducing the IF impedance at 1–2 GHz.

relaxation time or the momentum scattering time at 20–60 K.[14]

Figure 2.9(a) shows the device design for the IF channel of a prototype TACIT mixer (this is a capacitively-coupled TACIT mixer introduced in Chapter 5, but we present the design here to introduce the IF impedance model in more general terms). The IF channel for this prototype device has a ribbon-shaped mesa (note that the THz antenna structure is omitted here for visual simplicity) consisting of a small (5μm $\times 5\mu$m) active region at the center (see the inset) connected with two rather large 2DEG contacts ($\sim 350\mu$m long flares on both sides of the active region). Each of these 2DEG contacts has an Ohmic contact (circled 1 in orange) contacting the 2DEG and an Schottky contact (circled 2 in yellow) covering the most of the 2DEG contact area. The two Ohmic contacts are used to DC bias the IF channel and the capacitive contacts are used to couple out the IF response.

As we can see in Figure 2.9(a), the device design has wide (~ 300 μm) Ohmic contacts that add rather large 2DEG contacts to the device. The reason for this is to minimize the parasitic resistance from the Ohmic contacts, which if made small to match the active region directly, can add significantly large contact resistance to the device IF impedance.[15] To illustrate this point better, a typical value for the specific contact resistance is in the order of 1–2 Ωmm[16] [35], resulting in a parasitic resistance of 200–400 Ω for each Ohmic contact for a 5-μm contact. With a wider ($\sim 300\mu$m) Ohmic contact, this can be reduced to 3.3–6.6 Ω for each contact. Of course, this adds yet another parasitic impedance from each 2DEG contact. However, this impedance becomes small at low temperatures (thanks to high mobility of a 2DEG) and can be further tuned out with capacitive coupling at the 1–2 GHz range.

[14] The frequency limit for the lumped element model is roughly estimated to be ~ 6 GHz at 60 K and ~ 2 GHz at 20 K based on the relevant energy relaxation and momentum scattering rates.

[15] Also, small (in the order of a few μm) Ohmic contacts suffer from reliability problems as well.

[16] With optimized processing, we may achieve $\sim 10\times$ improvement on this [60].

Figure 2.9(b) shows the equivalent circuit for the IF channel with the variables defined in the figure. The 2DEG contacts present parasitic impedances consisting of the 2DEG resistance in series with the kinetic inductance of the 2DEG. The capacitive layers form parallel capacitor with these parasitic impedances and tune them out. Based on this equivalent circuit, derivation for the overall IF impedance ($Z_{IF} = R_{IF} + iX_{IF}$) is trivial. After some algebra, we get

$$R_{IF} = \frac{2\left(R_c + R_p\right)}{\left(1 - \omega_{IF}^2 L_p C_p\right)^2 + \omega_{IF}^2 \left(R_c + R_p\right)^2 C_p^2} + R_B \tag{2.9}$$

and

$$X_{IF} = \frac{2\omega_{IF}\left[L_p\left(1 - \omega_{IF}^2 L_p C_p\right) - \left(R_c + R_p\right)^2 C_p\right]}{\left(1 - \omega_{IF}^2 L_p C_p\right)^2 + \omega_{IF}^2 \left(R_c + R_p\right)^2 C_p^2} + \omega_{IF} L_B \tag{2.10}$$

where $\omega_{IF} = 2\pi f_{IF}$ is the angular IF frequency and the rest of the variables are defined in Figure 2.9(b).

The values for the lumped elements shown in Figure 2.9(b) can be numerically calculated based on the device geometry and 2DEG parameters (charge density and mobility). Figures 2.10 and 2.11 show the calculated IF impedance as a function of the frequency at 20 K and 60 K along with the calculated matching efficiency with a 50-ohm load (the input impedance of the first IF amplifier). For the calculation, we used $n_s = 2 \times 10^{11}$ cm^{-2} for both temperatures and $\mu = 1.85 \times 10^6$ cm^2/Vs for 20 K and $\mu = 5.0 \times 10^5$ cm^2/Vs for 60 K. As shown in the figures, at low frequencies ($f_{IF} << 1GHz$), the parasitic impedances dominate the IF impedance ($\sim$ 0.3–1 kΩ). At $f_{IF} \sim$ 1 GHz, the capacitive coupling can tune out most of the parasitic impedances, resulting in the device IF impedance mostly following the impedance from the active region (50–100 Ω) and thus achieving high IF coupling efficiency over 90% (see Figures 2.10(b) and 2.11(b)).

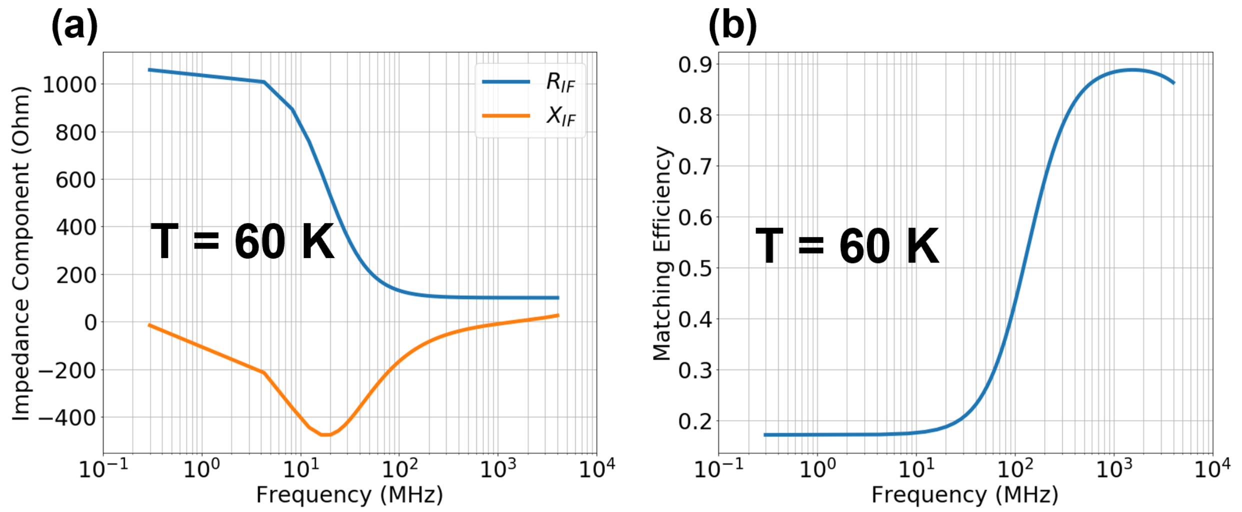

Figure 2.10: Calculated IF impedance and matching efficiency with a 50-ohm load at 60 K. (a) Device IF impedance. (b) Matching Efficiency. The peak response occurs due to the kinetic inductance that no longer gets canceled out at $\nu_{IF} >\sim 1$ GHz.

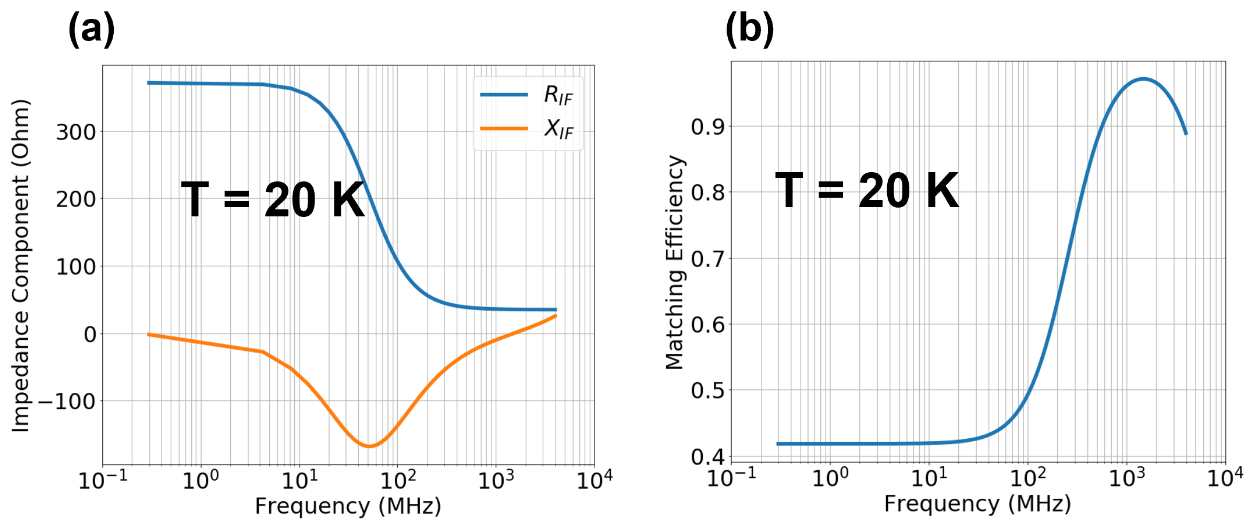

Figure 2.11: Calculated IF impedance and matching efficiency with a 50-ohm load at 20 K. (a) Device IF impedance. (b) Matching Efficiency. The peak response occurs due to the kinetic inductance that no longer gets canceled out at $\nu_{IF} >\sim 1$ GHz.

Mixer Characteristics

Finally, we present the modeling results for various mixer characteristics including conversion efficiency, mixer noise temperature, and required LO power. In modeling these mixer characteristics, we will assume that the IF response of TACIT mixers is bolometric in nature[17] and apply HEB mixer theory [55, 56, 57]. The HEB mixer theory was originally developed for bulk InSb HEB mixers [55] and further modified by Karasik et al. [56, 57] for superconducting HEB mixers, and can be applicable to 2DEG-based HEB mixers. The model assumes the bolometric medium as a lumped element (in our case, 2DEG in the active region) where the temperature distribution is uniform. We include the effect of the intersubband absorption in terms of an RF coupling efficiency. Also, we will turn off any frequency dependence in our calculation as this is a relatively small effect at the IF frequency range of interest (1–2 GHz). For the rest of the section, we will focus on providing the modeling results—for full details on the mixer theory, see [55, 56, 57].

In applying the HEB mixer theory, we first start by simulating the IV curves for our bolometric medium—a 5μm $\times$5μm square patch of 2DEG—by scaling the IV curves measured from a Hall bar fabricated from the same 40-nm GaAs/AlGaAs QW. Figure 2.12 shows the IV curves at 10 K – 100 K measured in the Hall bar device with a 2DEG channel dimension of 40 μm W $\times$ 620μm L. For the modeling, we choose the IV curves at 20 K and 60 K, the low and high temperature limits within the proposed operating temperature for TACIT mixers.

The IV curves in Figure 2.12 were taken with two-terminal measurements that in-

[17] As we briefly discussed earlier in the chapter, the IF response of TACIT mixers may be caused by a combination of both bolometric effect (due to electron heating) and other non-bolometric effects (e.g. difference in mobility between two subbands). In this section, we only present the modeling results based on the bolometric effect. For the modeling results based on the other non-bolometric effects, refer to [45, 44]

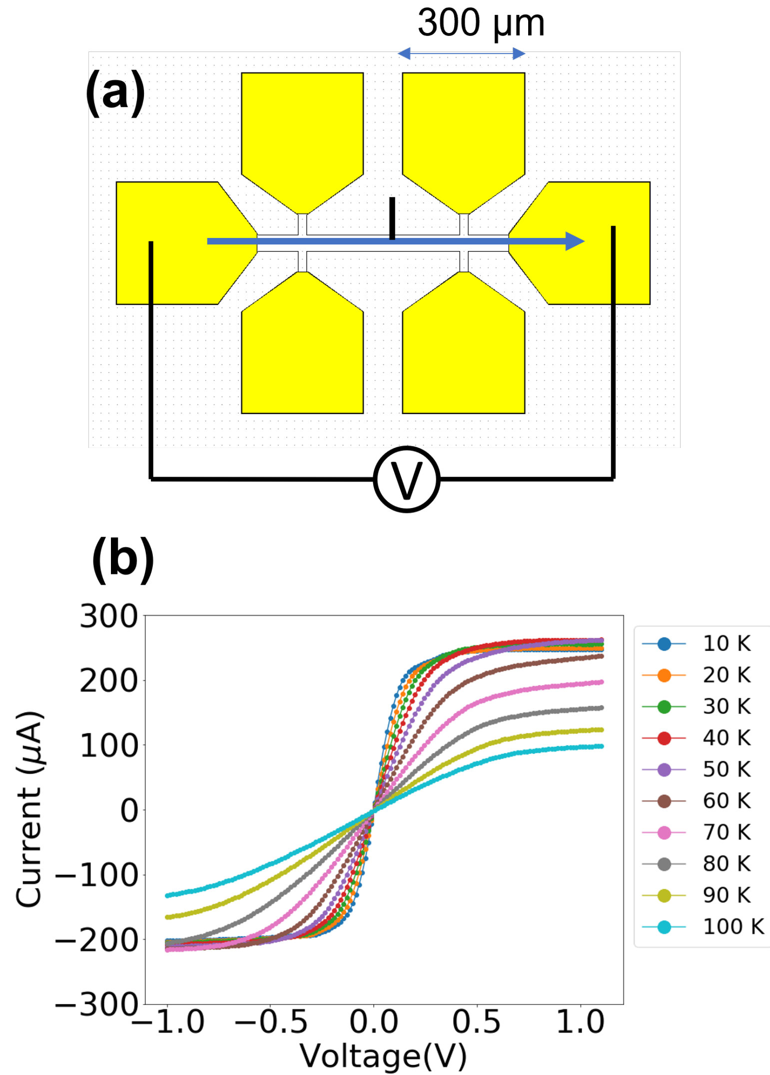

Figure 2.12: Hall bar design and the IV curves measured at 10 – 100 K. (a) Schematic showing the Hall bar for the IV curve measurements. The 2DEG channel dimension is 40 μm W $\times$ 620μm L between the left and the right Ohmic contacts in the Hall bar. The IV curves were measured across these two terminals indicated in the schematic. (b) Measured IV curves at 10 – 100 K. These IV curves include the effect of contact resistances of $\sim 100\Omega$.

clude the effect of the contact resistance of the Ohmic contacts in the measured resistance.[18] The total contact resistance is assumed to be $\sim 100\Omega$, and remained relatively temperature-independent over 10–100 K. This contribution is subtracted from the measured resistance such that the modified resistance reflects only the resistance of the 2DEG channel. To scale the IV curves for the single square of 2DEG, we divide this resistance by the number of squares in the 2DEG channel ($\sim$ 15.5) to get the sheet resistance R_s. To calculate the expected voltage drop $V = IR_s$, we use the current I expected for 5μm-wide 2DEG assuming the same current density from the IV curves in Figure 2.12. The scaled IV curves at 20 K at 60 K are shown in Figure 2.13 in blue dotted lines. For simplicity in modeling, we fit these IV curves to a hyperbolic tangent function $I(V) = a \tanh bV + cV + d$, which fits the data curves reasonably well (see the orange solid lines in Figure 2.12).

First, we calculate the conversion efficiency. The conversion efficiency of a mixer is defined as the ratio between the output LO power divided by the input RF power. The expression for the conversion efficiency η for a hot-electron bolometer can be derived by considering an equivalent circuit model for the bolometer [55]. The expression (excluding the frequency dependence) is given by

$$\eta = 2\alpha C^2 \frac{R_L R}{(R+R_L)^2} \frac{\alpha P_{LO}}{P_{DC}} \frac{1}{(1 + C\frac{R-R_L}{R+R_L})^2} \tag{2.11}$$

where α is the RF coupling efficiency, $C = \frac{Z-R}{Z+R}$ is the self-heating parameter where Z is the differential resistance and R is the linear resistance that can be extracted from an IV curve of the bolometer, R_L is the load resistance for an IF amplifier (typically 50 Ω), P_{LO} is the local-oscillator power, and P_{DC} is the DC power dissipated in the bolometer

[18]Four-terminal measurements are possible to eliminate the effect of the contacts but were not carried out with this device.

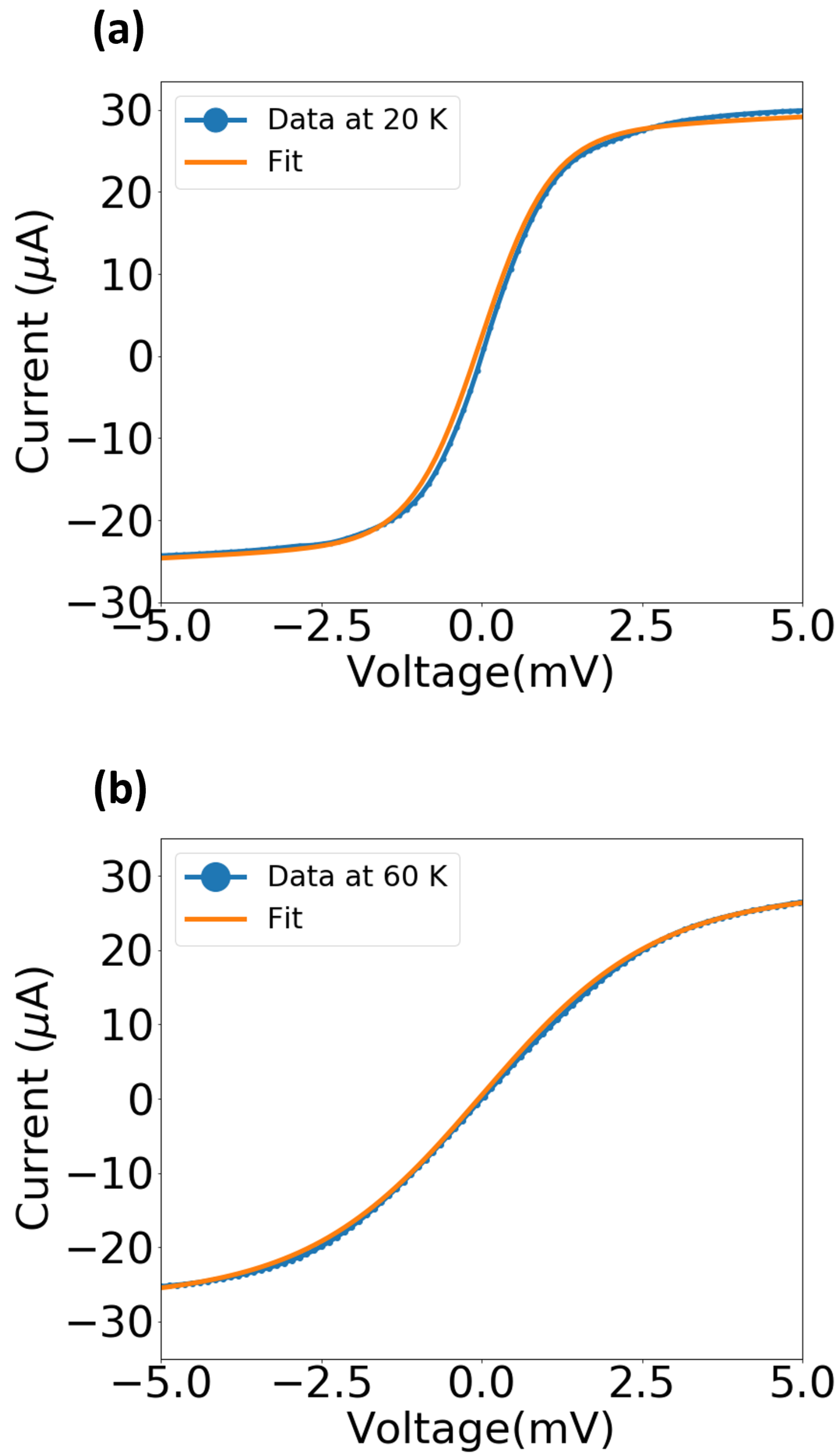

Figure 2.13: IV curves scaled for a 5μm $\times$ 5μm active region with hyperbolic tangent fits. (a) IV curve and the fit at 20 K. (b) IV curve and the fit at 60 K. The fitted functions were used for numerical simulations of the mixer characteristics.

[56].[19] We assume $\alpha = 0.8$ and $P_{DC} = P_{LO}$ for our modeling, and we can extract the rest of the variables from the IV curves in Figure 2.13. The calculated conversion efficiency is plotted in Figure 2.14(a) for 20 K and in Figure 2.15(a) for 60 K, along with the scaled IV curves.

Next, for the single-sideband (SSB) noise temperature, the two dominant noise contributions in an HEB mixer are the Johnson noise and thermal fluctuation (TF) noise. The first comes from the random motion of electrons in the bolometer that results in the random change in its output voltage for the load. The latter refers to the noise from the random exchange of energy between the lattice and the bolometer, resulting in fluctuation in its temperature. The expression for the SSB Johnson mixer noise temperature, T_m^J and the thermal energy fluctuation mixer noise temperature T_m^{TF} (again ignoring any frequency dependence) are given in [56]:

$$\mathrm{T_m^J} = \frac{2T_e \mathrm{P_{DC}}}{\alpha^2 \mathrm{C}^2 \mathrm{P_{LO}}} \tag{2.12}$$

$$T_m^{TF} = \frac{2T_e^2 G}{\alpha^2 P_{LO}} \tag{2.13}$$

where T_e is the electron temperature in the bolometer and α is the RF absorption efficiency. The electron temperature can be estimated based on the IV curves with the known temperature dependence of the resistance on the electron temperature (in our case, we have the temperature coefficient of resistance $\alpha_{TCR} \sim 0.03\mathrm{K}^{-1}$, which is roughly constant up to 100 K). We again assume $P_{DC} = P_{LO}$ and $\alpha = 0.8$ for the modeling. Each noise contribution and the total SSB mixer noise temperature ($T_m = T_m^J + T_m^{TF}$) are plotted in Figure 2.14(b) for 20 K and in Figure 2.15(b) for 60 K, along with the

[19] For the differential resistance at high IF frequency $Z(\infty)$ in the original expression in [56], we assume $Z(\infty) = R$.

scaled IV curves.

Figures 2.14 and 2.15 show that at optimal bias points near the knee of the IV curve (where the non-linearity due to the electron heating becomes the maximum), the calculated conversion efficiency and the total SSB mixer noise temperature are ~ -9 dB and ~ 400 K for 20 K, and ~ -12 dB and $\sim 1,000$ K for 60 K.[20] Also, the local oscillator power P_{DC} based on the relation $P_{DC} = P_{LO}$ remains small ($< 0.1\mu$W) over the DC bias range shown in the figures. These modeling results suggest that TACIT mixers can be very sensitive THz mixers at high operating temperatures, with small ($< 1\mu$W) required LO power.

Before we conclude the chapter, we also present the calculation results for the output noise temperature. This is the noise temperature for the output noise power of an HEB mixer delivered on the load and will be referred to when we study the output noise power of a capacitively-coupled TACIT mixer in Chapter 5. The output noise temperature is calculated by dividing the SSB mixer noise temperature by the conversion efficiency (see [56] for the details), and Figure 2.16 and Figure 2.17 show the calculated output noise temperature for 20 K and 60 K, respectively.

The output noise temperature shown in Figure 2.16 and Figure 2.17 is first dominated by the Johnson noise contribution (see the blue dashed line) near zero DC bias (where there is no electron heating) and peaks near the knee of the IV curve (where there is most heating) with the contribution from the thermal fluctuation (see the orange dashed line) becoming larger than that from the Johnson noise. This is consistent with what we would expect as we have the Johnson noise contribution $T_J^{out} \sim T_e$ and the thermal fluctuation output noise temperature $T_{TF}^{out} \sim T_e^2 dR/dT$. Note that the output noise temperature also

[20]This, in fact, doesn't include the effect of the contacts in real TACIT mixers. However, we already showed that we can make the IF impedance closely follow the resistance of the active region by capacitively reading out the IF response. We predict that this will make the effect of the contacts negligibly small on the calculated mixer characteristics.

includes the effect of the coupling efficiency between the bolometer and the load; this leads to reduction of the Johnson noise contribution (blue dashed line) at a higher DC bias at both temperatures.

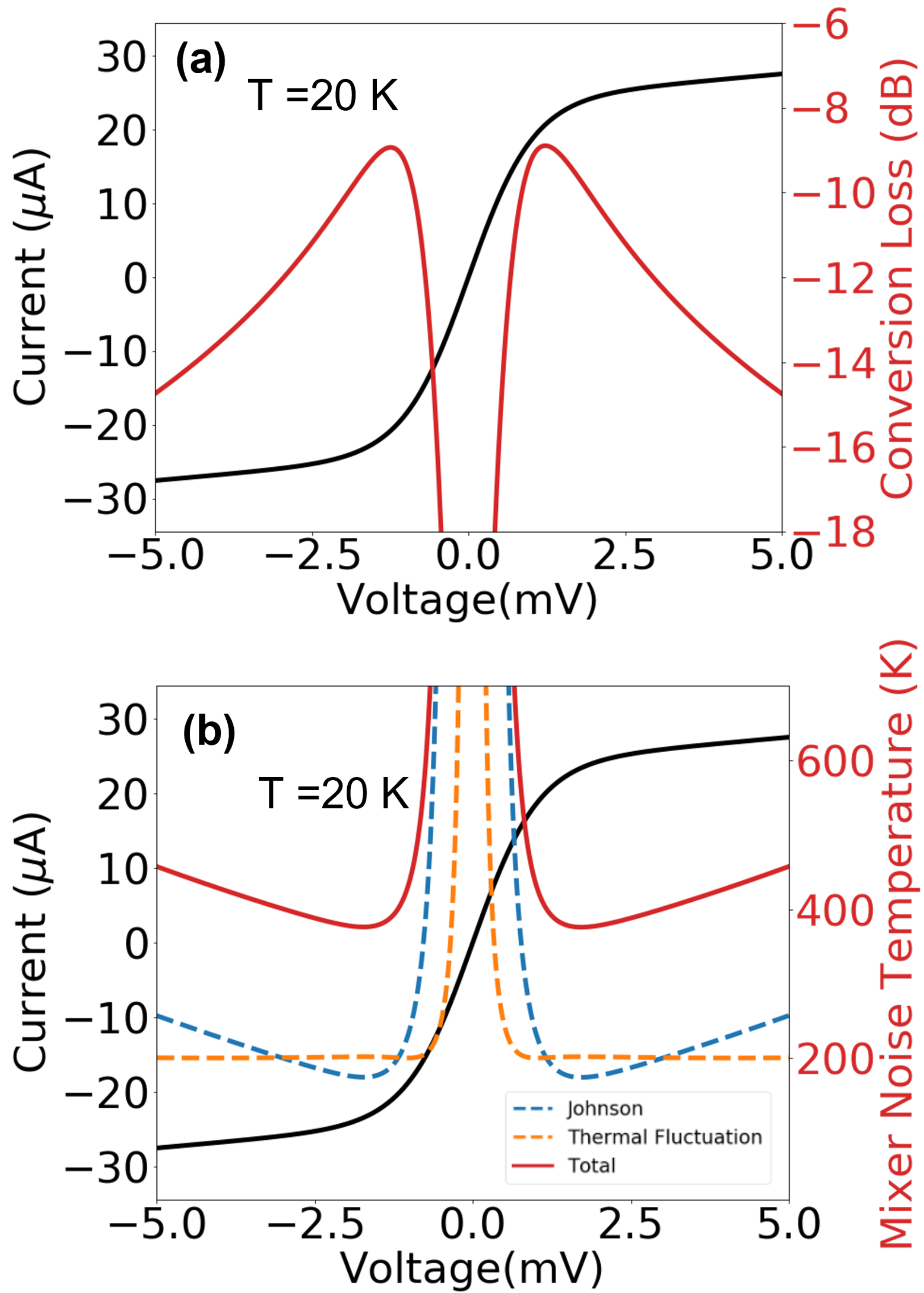

Figure 2.14: Conversion efficiency and mixer noise temperature at 20 K. THz absorption efficiency of 0.8 was assumed for the calculation. (a) Conversion efficiency. (b) Mixer noise temperature.

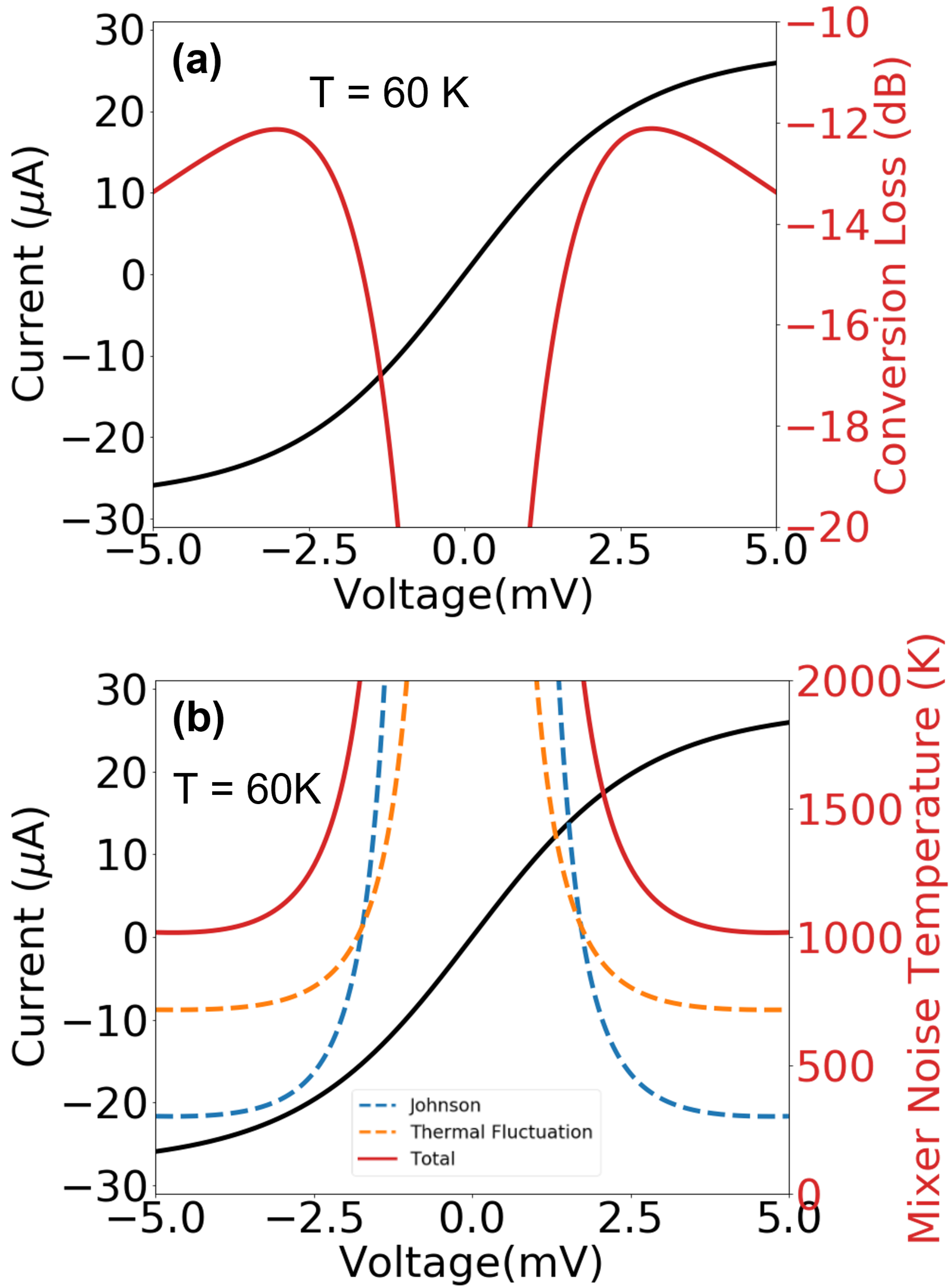

Figure 2.15: Conversion efficiency and mixer noise temperature at 60 K. THz absorption efficiency of 0.8 was assumed. (a) Conversion efficiency. (b) Mixer noise temperature.

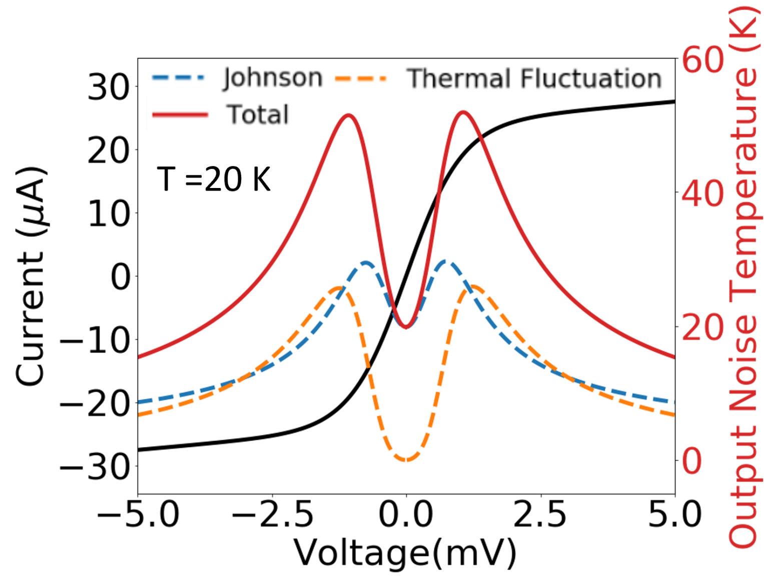

Figure 2.16: Output noise temperature at 20 K.

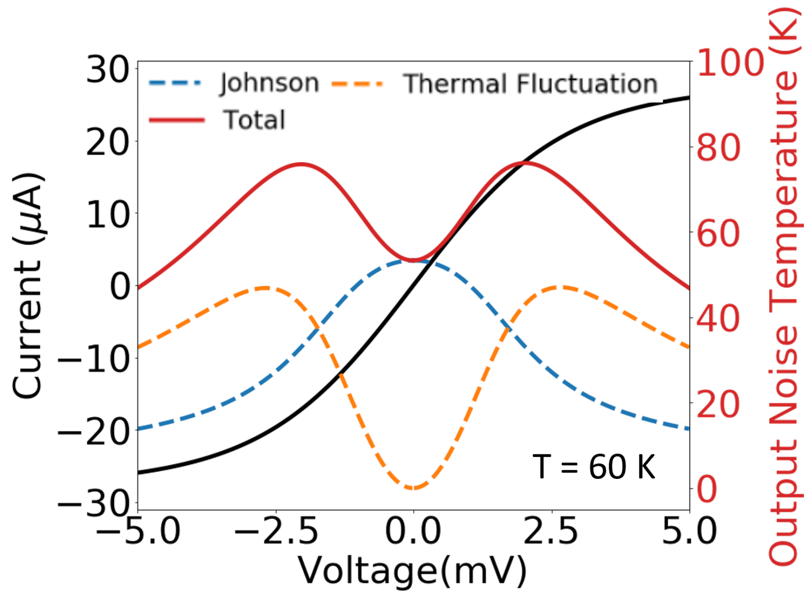

Figure 2.17: Output noise temperature at 60 K

Chapter 3

Device Fabrication

For precise tuning of the detection frequency for TACIT mixers, independent control of the charge density and the DC electric field (applied along the growth direction of the QWs) is important. For TACIT mixers, this requires the fabrication of symmetric, well-aligned dual-gate structures on thin (typically less than 1μm) GaAs/AlGaAs heterostructure membranes containing high-mobility 2DEG. Such fabrication can be challenging for a variety of reasons, including the extreme fragility of the thin membranes and difficulties in maintaining the high mobility and charge density of the 2DEG throughout various processing steps. Also, the close proximity of the gates can easily cause leaks in the gates, resulting in reliability problems. In addition, the need to access the terminals defined on both sides of the thin membrane may complicate the processing steps, resulting in low device yields. Despite these challenges, we successfully fabricated prototype TACIT mixers using an advanced flip-chip technique that we developed that enables dual-side processing of thin ($< 1\mu$m) GaAs/AlGaAs heterostructure membranes without sacrificing the high mobility and the charge density of the 2DEG system.

In this chapter, we introduce our Indium-Bond-And-Stop-Etch (IBASE) technique for the fabrication of the dual-gate structures for TACIT mixers and provide characterization

results for charge density and mobility profiles, as well as charge and electric field control with the fabricated dual-gate structures.

3.1 Previous Back-gating Techniques

Before we discuss our IBASE technique in detail, we will briefly review two types of conventional back-gating techniques for high-mobility GaAs/AlGaAs heterostructures: regrowth [61, 62, 63, 64] and flip-chip [65, 62, 66, 67, 68] techniques. In the regrowth techniques, highly-doped conductive layers for back gates are grown first with molecular beam epitaxy (MBE). The conductive layers are then patterned by selectively damaging their conductivity prior to the re-growth of active quantum-well (QW) heterostructure layers. Selective damage can occur either in-situ via focused ion beam[61, 63] or ex-situ via oxygen implantation[64] or selective wet etch[62]. While these regrowth techniques are compatible with high-mobility devices, they require either expensive focused-ion beam equipment for the in-situ method or complex processing steps and extensive cleaning procedures for the ex-situ methods. Additionally, because these regrowth techniques pre-define the patterns for the back gates at the wafer level prior to fabrication of individual devices, they are not robust to design variations after the QW wafer is grown. Furthermore, precise alignment, which is required for the dual-gate structures for TACIT mixers, can be challenging in the absence of alignment features.

In flip-chip techniques, the back side of QW samples is first thinned down to a sufficient thickness, and then standard lithographic patterning and metallization steps are used to define patterned back gates directly on the back side of QW samples. In the early versions of this approach, the back side is thinned down to $\sim 50\mu$m, and then patterned for back gates. However, the thinned QW samples require extreme care in handling without a host substrate, and very a high voltage (~ 100 V) needs to be applied for the

back gate operation [65]. More recent flip-chip techniques solve the handling problem by using a host substrate [66, 68]. In these techniques, the front side of the QW sample is processed first and then flip-chip bonded to the substrate with the entire front-side of the sample glued with epoxy with the host substrate. To avoid possible edge bead problem that makes the back-side patterning difficult, the host substrate is intentionally chosen to be smaller than the QW sample. After the bonding, the back side of the QW samples is thinned down to a very thin (in the order of 1 μm) layer with the help of an etch-stop layer grown during the MBE growth of the QW structure. However, in these techniques, electrically accessing the front-side terminals buried in the epoxy requires either a back-side etch step for making vias [66] or careful alignment of front-side terminals to the sidewalls of the sample and application of silver paste [68], both of which often results in rather complex additional back-side processing steps with unreliable electrical contacts and low yields.

Our IBASE process allows for the dual-side processing of thin ($< 1\mu$m) GaAs/AlGaAs heterostructure membranes without the problems listed above. In our technique, the front-side contacts are selectively indium-bonded to matching electrode patterns defined on a host substrate before the application of underfill epoxy that fills and bonds the rest of the front-side of the sample. The indium bonds provide robust and reliable electrical contacts to the front-side terminals, and the host substrate, chosen to be larger than the QW sample, provides bonding pads for wire bonds for easy electrical access to the front-side terminals. The underfill epoxy has an excellent filling property and fills any gap in the bonded surfaces, offering protection for the indium bonds as well as the rest of the front-side area against any mechanical or chemical damages throughout the back-side processing steps. The cured underfill epoxy can be easily peeled off to avoid any edge bead problem for the patterning of the back side of the QW sample. In addition, with the thin QW membrane, the alignment for the back gates can be done very precisely

with the alignment patterns defined on the front side of the QW sample that are visible through the thin layer. Furthermore, the individual processing of the flip-chip bonded samples also offers robustness against any design variation for individual TACIT mixers.

3.2 Indium-Bond-And-Stop-Etch (IBASE) Process

As with the EBASE process, the IBASE process begins with the growth of QW epilayers containing an etch-stop layer. This etch-stop layer consists of AlGaAs with higher Al content, which provides high selectivity against citric acid solution we use later for the back-side processing. After the growth of the QW sample, the rest of the IBASE processes can be divided into three phases: front-side processing, flip-chip bonding and underfilling, and back-side processing. In this section, we give a brief overview for each phase of the processing steps. For details and step-by-step recipes, see Appendix C.

Sample Growth

While the IBASE process can be applied to any variations of the GaAs/AlGaAs QW structures including bilayer QWs and QW superlattices, the test devices as well as the prototype TACIT mixers presented in this work were fabricated from a modulation-doped single 40-nm QW structure (Figure 3.1(a) shows a simplified version of the QW structure). The QW structure was grown using molecular beam epitaxy (MBE) on an intrinsic GaAs substrate wafer with a diameter of 2" and a thickness of $\sim$500 μm. The detailed structure is like the following (in the order of the growth sequence): a 500-nm GaAs buffer layer and a smoothing layer consisting of 100 periods of 10-nm $Al_{0.3}Ga_{0.7}As$ and 3-nm GaAs, 500-nm of $Al_{0.74}Ga_{0.26}As$ as an etch-stop layer, a 10-nm GaAs cap layer for the QW structure, the first barrier layer consisting of 200-nm $Al_{0.3}Ga_{0.7}As$, a Si modulation doping layer, and 100-nm $Al_{0.3}Ga_{0.7}$, 40-nm GaAs QW layer, the second

barrier layer consisting of a 100-nm $Al_{0.3}Ga_{0.7}As$ layer, a Si modulation doping layer, a 200-nm $Al_{0.3}Ga_{0.7}As$ layer, and finally another 10-nm GaAs cap layer. This created a single 40 nm quantum well with the center of the 2DEG layer 330 nm below the top surface. Hall measurements showed that the 2DEG in the sample has intrinsic charge density $n_0 = 2.2 \times 10^{11}$ cm^{-2} and mobility $\mu = 2.0 \times 10^5$ cm^2 V^{-1} s^{-1} at 77 K, and $n_0 = 2.1 \times 10^{11}$ cm^{-2} and $\mu = 9.4 \times 10^6$ cm^2 V^{-1} s^{-1} at 2 K.

Front-side Processing

After the growth, the QW wafer is diced into smaller samples of desired sizes (typically 10 cm by 10 cm) for front-side processing. During the front-side processing (Figure 3.1(b)), standard lithographic patterning, wet etch, and metallization steps are used to define the 2DEG mesa and the front-side contacts. For TACIT devices, these include two Ohmic contacts and one Schottky gate (to be the bottom gate on the buried side). Standard NiAuGeNiAu sequence is used for the two Ohmic contacts, with annealing at 500 ° C for 60s after the deposition of the metal layers. TiAu metallization is used to define the gated area in the devices. Following the metallization steps, the whole surface is passivated with SiO_2 and vias are made using dry etch to access the Ohmic contacts and the gate metal. In the final metallization step, metal patterns (simple electrodes for the Hall bar and antenna patterns for TACIT mixers) are deposited to contact the gate metal. The entire QW sample at this point contains multiple devices and is diced into smaller dies (2 mm x 2 mm) for flip-chip bonding.

Flip-chip Bonding and Underfilling

A host substrate is prepared for flip-chip bonding, with metal patterns on the host substrate that match the front-side contacts on the QW die (Figure 3.1(c)). This host

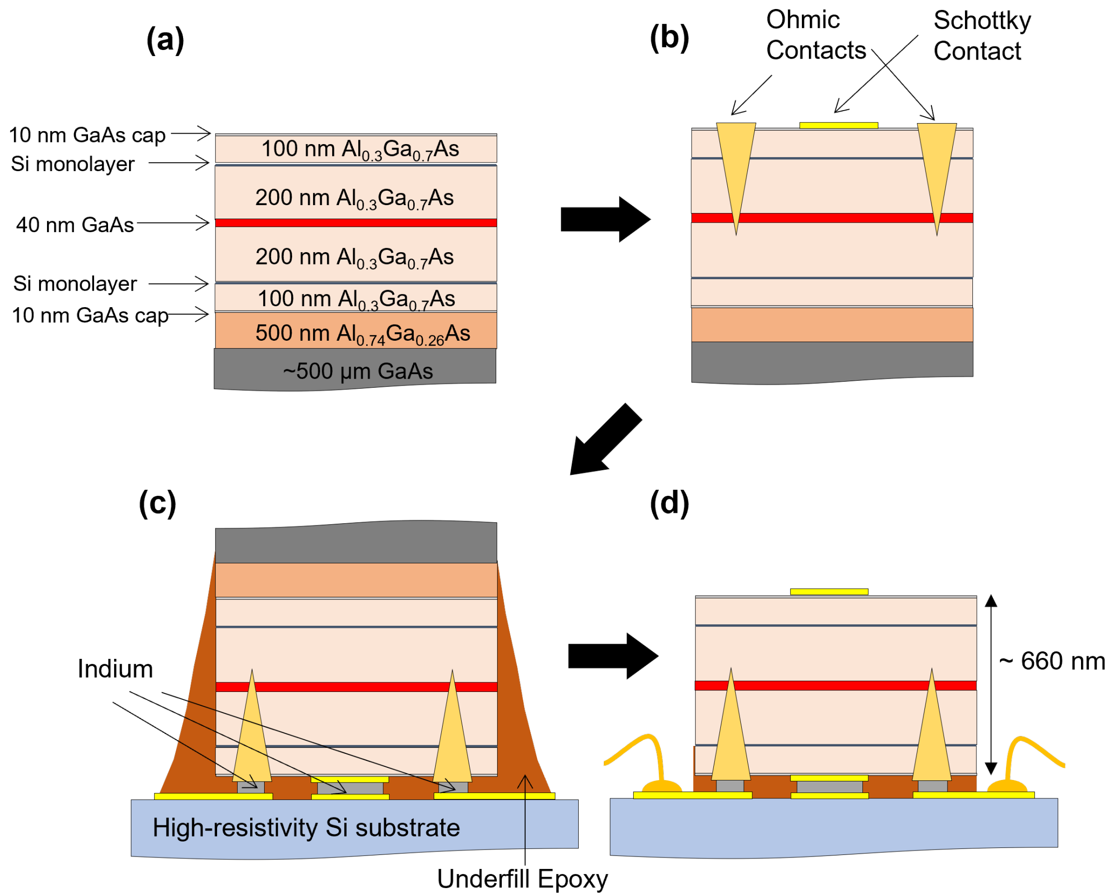

Figure 3.1: Flow diagrams for the Indium-Bond-And-Stop-Etch (IBASE) technique. The schematics show the vertical profiles of a TACIT mixer (or a dual-gated Hall bar) throughout the IBASE process (a) Simplified QW structure (not to scale) grown with molecular beam epitaxy (MBE). The QW epilayer contains a modulation-doped single 40-nm GaAs/AlGaAs QW, as well as an etch-stop layer (orange) required for the IBASE process. (b) Vertical profile of the device after front-side processing. Standard photolithographic patterning and metallization steps are used to define the Ohmic contacts and one of the Schottky gates. (c) Vertical profile after flip-chip bonding with indium and underfilling. The QW die is bonded with a host Si substrate with matching electrodes. To protect the bonded sides for the rest of the processes, underfill epoxy is dispensed and cured at 80°C. (d) Vertical profile after back-side processing. Mechanical lapping and a series of selective wet etches are performed to remove the sacrificial GaAs on the back side as well as the etch-stop layer. After the removal, the back side of the QW epilayer has a mirror finish, and the second Schottky gate is defined using the standard lithographic and metallization steps. To electrically access the top and bottom terminals, wire bonds are made on the bonding pads on the Si substrate.

substrate can be either intrinsic GaAs or Si, but, in our case, we choose high-resistivity Si for its transparency at THz frequencies. The substrate has a larger dimension than the QW die to provide bonding pads on the excess area for wire bonds that electrically access the front-side (now buried) terminals of the QW die. For the electrodes on the Si host substrate, standard lithographic patterning and metallization steps are used. On the bonding sites on the substrate, small indium islands are deposited for the flip-chip bonding. After the host substrate is ready, the QW die is flip-chip bonded to the substrate via heated indium bonding. A constant, uniform force is applied to the flip-chip assembly while both the die and the substrate are pressed against each other and rapidly heated up 160 °C and cooled down for the indium to melt and form reliable bonds with the front-side contacts of the QW die. For good bonding quality, a quick HCl dip is performed before the bonding to remove the indium oxide on the indium islands. After the bonding, a small amount of underfill epoxy (EPO-TEK® 353ND) is dispensed on one side of the flip-chip assembly and cured at low temperature (80 °C) for ∼2 hours. The underfill epoxy has an excellent filling property that completely fills any gap in the bonded surfaces. The cured epoxy provides mechanical stability for the QW die and is highly resistant to chemical etches used later in the back-side processing steps, providing good mechanical and chemical protection for the bonded surfaces against the rest of the back-side processing steps.

Back-side Processing

After flip-chip bonding and underfilling, the back side of the QW die is now ready for further processing (Figure 3.1(d)). All of the sacrificial GaAs on the back side of the QW die is removed, with the bulk ($\sim 450\mu$m) of the GaAs removed with mechanical lapping and the remaining ($\sim 50\mu$m) GaAs removed with a series of selective wet chemical

etches. For the mechanical lapping, Al_2O_2 films of varying grit size are used. For the chemical etches, citric acid solution (H20:citric acid of 1:5.5 solution) is used to remove the remaining GaAs and diluted HF (1:4) solution to remove the etch stop layer. The citric acid solution has a very high selectivity against the designed etch stop layer. Similarly, the HF solution has a high selectivity against the 10-nm GaAs cap layer, allowing for the isolation of very thin QW membrane (containing a single QW epilayer!) and providing a mirror finish on its back side. At this point, the underfill epoxy on the side wall sits taller (typically $\sim 50\mu$m) than the QW membrane and must be removed for contact lithography. Fortunately, the cured epoxy on the side walls can be easily peeled off with either a razor blade or tweezers and doesn't leave any residue on the surface, providing a nice and clean surface ready for the final metallization step. Standard lithography and metallization steps are used for the final metallization step that defines the top (exposed) gate metals with electrode patterns (simple electrodes for Hall devices and the rest of the antenna patterns for TACIT mixers). Finally, wire bonds are made directly on the bonding pads defined on the host substrate, providing easy electrical access to both the front- and back-side contacts of the QW epilayer.

3.3 Characterization Results

A series of Hall measurements were performed to verify the compatibility of the IBASE process with high-mobility 2DEG throughout the IBASE process, as well as to check the charge control of the fabricated dual-gate structure. Both ungated and dual-gated Hall bars were used for the measurements. Furthermore, the independent control of charge density and the electric field (applied along the growth direction) was confirmed with the dual-gate structures in the fabricated TACIT mixers, but the characterization results will be presented in Chapter 4.

Mobility and Charge Density

To verify the compatibility of the IBASE technique with high-mobility devices, we measured the mobility and the charge density of a ungated Hall bar device before and after the IBASE process. The mobility and the charge density were measured using the standard Hall measurements before the IBASE process (Figure 3.2(a)) and after the IBASE process (Figure 3.2(b)). For this ungated device, no further patterning and metallization steps were done on the top (exposed) side of the QW die.

Figures 3.2(c) and (d) show the mobility and the charge density before and after the IBASE process. A slight improvement on the mobility was observed at 2 K likely due to a change in the well potential after surface processing on the top (back) side of the QW epilayer. Figure 3.2(d) shows that most of (95 %) the charge density is preserved throughout the IBASE process.

Charge Control

Figure 3.3(a) shows the dual-gated Hall bar fabricated with the IBASE process. The image shows the thin (< 660 nm) QW membrane (marked by green dotted square) in which a gated Hall bar is defined on the front (buried) side. The terminals of the Hall bar are bonded to the matching electrode patterns defined on the host Si substrate (marked by blue dotted square) via indium bondings (marked by white rectangles). Underfill epoxy was used to fill the rest of the bonded area. The top inset (in red dashed rectangle) shows a Schottky (top) gate defined on the back side of the QW membrane. The good visibility of the alignment marks defined on the front (buried) side of the QW membrane allows for easy, precise alignment for the top gate pattern, as shown in the bottom inset.

Figure 3.3(b) shows the charge tunability in a single gated Hall bar.[1] Charge control

[1]Note that the measurement was done in a single-gated Hall bar after the back-side processing except for the final metallization step. After the final metallization, the top gate started to leak, so no

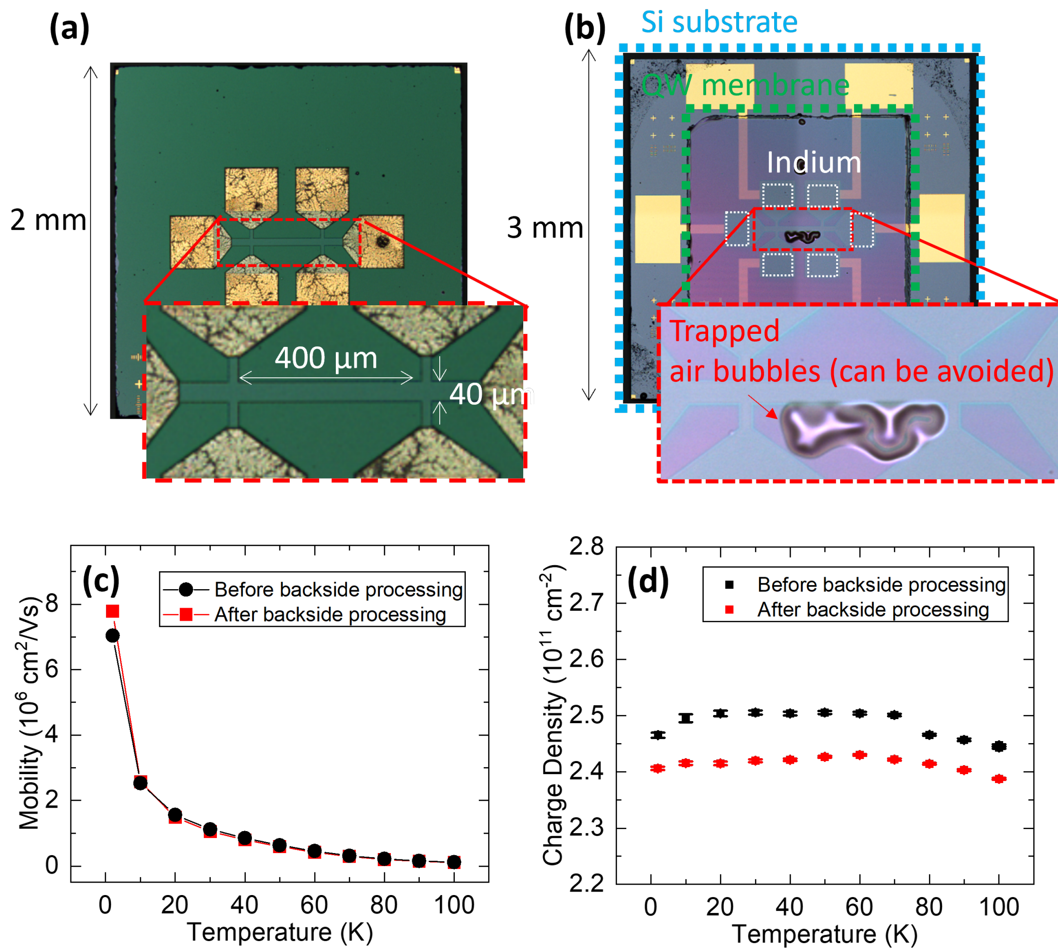

Figure 3.2: Mobility and charge density characterization for the IBASE process. (a) Ungated Hall bar device used for the mobility and charge density characterization before the IBASE process. The inset shows the 2DEG channel that has a dimension of 400μ m L $\times$ $40\mu m$ W. (b) The same undgated Hall bar after the IBASE process. The microscope image shows the thin (< 660 nm) QW membrane (marked by green dotted square) in which the terminals of the Hall device defined on the front side (now buried side) are bonded to the matching electrode patterns on the Si substrate (marked by blue dotted square) via indium bonds (marked by white dashed rectangles). The rest of the QW membrane area is filled with underfill epoxy to protect the bonded sides. Occasionally, air bubbles can get trapped in the bonded sides during the underfilling process (as shown in the inset), but this can be avoided with care during the dispensing process. (c) Mobility of the 2DEG before and after the IBASE process, demonstrating the compatibility of the IBASE technique with high-mobility devices. After backside processing, a slight improvement on the mobility was observed at 2 K, likely due to a change in built-in electric field in the QW after surface processing. (d) Charge density before and after the IBASE process. After the IBASE process, the 2DEG retains most ($\sim$ 95%) of its charge density.

at 77 K and 2 K with the bottom (buried) gate. Linear gating was observed with the charge tunability $\Delta n_s/\Delta V_g$ is $2.00(1) \times 10^{11} cm^{-2}/V$ at 77 K. Based on simple parallel-plate capacitor model, we get $c/e \sim 2.1 \times 10^{11}$ cm^{-2}/V based on Eq. 2.2 with $d = 330$ nm, which agrees well with the measured charge tunability. Extrapolating the linear gating, we estimate the depletion voltage to be -1.0 V.

measurement was done after the final metallization step for this sample.

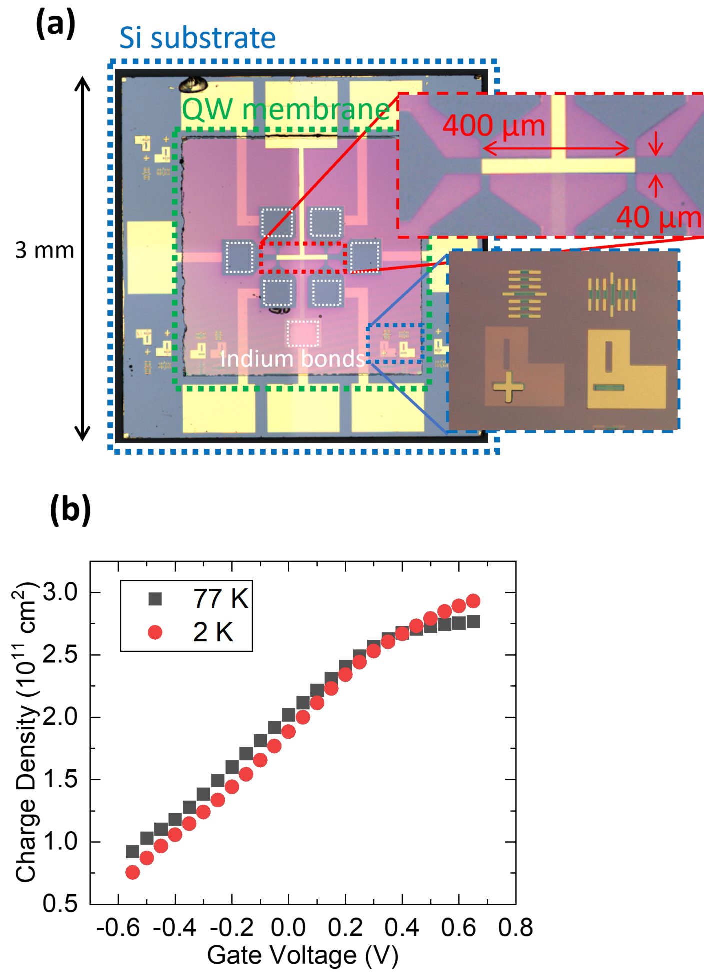

Figure 3.3: Charge control in a gated Hall bar fabricated with the IBASE technique. (a) An optical microscope image showing a dual-gated Hall bar device processed with the IBASE technique. The image shows the thin (< 660 nm) QW membrane (marked by green dotted square) in which a gated Hall bar is defined on the front (buried) side. The terminals of the Hall bar are bonded to the matching electrode patterns defined on the host Si substrate (marked by blue dotted square) via indium bondings (marked by white rectangles). Underfill epoxy was used to fill the rest of the bonded area. The top inset (in red dashed rectangle) shows a Schottky (top) gate defined on the back side of the QW membrane. The good visibility of the alignment marks defined on the front (buried) side of the QW membrane allows for easy, precise alignment for the top gate pattern, as shown in the bottom inset. (b) Charge control at 77 K and 2 K with the bottom (buried) gate. Linear gating was observed with the charge tunability $\Delta n_s/\Delta V_g$ is $2.00(1) \times 10^{11} cm^{-2}/V$. This is consistent with the charge tunability predicted with a simple parallel-capacitor model. Extrapolating the linear gating, we estimate the depletion voltage to be -1.0 V.

Chapter 4

Resistively-coupled Device

The four-terminal geometry and the tunability of TACIT mixers demand careful consideration in designing and characterizing the devices. Unlike two-terminal HEB mixers, TACIT mixers require dual-gate structures with vertical offsets for THz absorption via intersubband transitions, which complicates the integration of THz antenna structures with the rest of the terminals in TACIT mixers. For example, it is difficult to integrate a log-spiral THz antenna, one of the popular THz antenna structures for superconducting HEB mixers, in TACIT mixers simply due to difficulties in laying out the two spiral antenna arms without intersecting the two additional bias lines required for TACIT mixers.

In addition, the tunability of TACIT mixers requires care in characterizing the device performance. This is because most of the device properties for TACIT mixers depend on the combination of three DC voltage biases, including the source-drain bias, and the sum and difference voltages, that control the electron temperature in the source-drain channel, the charge density, and the DC electric field (along the growth direction of the QW) in the active region of TACIT mixers, respectively. The complication is best illustrated in characterizing an IV curve for a TACIT mixer; unlike in two-terminal HEBs where a single IV curve can characterize the device, a TACIT mixer can have multiple

IV curves with drastically different IV behavior depending on the sum and difference voltages (i.e. the charge density and the DC electric field in the active region). Similar tunable behavior is also observed in the RF absorption and the IF read-out in TACIT mixers, so care must be taken in keeping track of and controlling the DC bias conditions for the optimal operation of TACIT mixers.

Despite these challenges, we successfully design, fabricate, and characterize two versions of prototype TACIT mixers. The first device is what we call a resistively-coupled TACIT mixer, in which the IF response is read out by the two Ohmic contacts of the device. This is the very first prototype TACIT mixer, so a simple single-slot antenna was used for its simplicity in design and convenience in integration with the four-terminal geometry of TACIT mixers. As we will see shortly, the first prototype device has a rather large 2DEG mesa with a wide (∼1 mm) contact area that significantly adds parasitic impedance to the overall IF impedance of the device. To remedy this, we designed and fabricated the second prototype TACIT mixer, in which the IF response is capacitively coupled out with the help of two capacitive metal patterns deposited on the 2DEG contact area.[1] For this capacitively-coupled TACIT mixer, a modified bow-tie (resembling a Maltese cross) was used to accommodate the two capacitive metal patterns with the antenna design and also to exploit the broadband operation of the bow-tie antenna. As we discussed in Chapter 2, the idea behind the capacitive coupling is to add a capacitor in parallel with the 2DEG contact area, which is mostly inductive, to reduce the overall IF impedance at GHz frequencies (1–2 GHz). The design, fabrication, and characterization of the capacitively-coupled TACIT mixer will be the main topic of Chapter 5.

In this chapter, we will present the design, fabrication, and characterization results for the resistively-coupled TACIT mixer integrated with a single-slot antenna. In this device, we confirmed the wide tunability in the detection frequency (2.52–3.44 THz) for

[1]We briefly touched on this in Chapter 2 when we discussed the IF model for the device.

TACIT mixers, as well as the heterodyne detection (mixing) capability at 2.52 THz at 60 K. The frequency dependence of the IF response also confirmed the wide IF bandwidth (> 6 GHz) of the device at 60 K. In addition, the tunability shown in the direct detection shows good qualitative agreement with the response model based on the impedance model for the intersubband absorption.

Several limitations, such as poor conversion efficiency and gate degradation, were observed in this first prototype TACIT mixer. Due to the poor conversion efficiency, the sensitivity (mixer noise temperature) was not measured in this device. We attribute such poor conversion efficiency to poor performance of the sub-optimal single-slot antenna and to the large parasitic impedance introduced with the large 2DEG mesa of the device. While we will briefly discuss these factors at the end of the chapter, they will be evaluated more quantitatively in Chapter 5 that discusses the capacitively-coupled prototype TACIT mixer, in which similar poor conversion efficiency was still observed.

4.1 Device Design and Fabrication

Design

Figure 4.1 illustrates the design for a resistively-coupled prototype TACIT mixer integrated with a single-slot antenna. The 2DEG mesa (circled 1) has wide (1 mm) contact areas at its sides for two Ohmic contacts (circled 2) and a narrow (5 μm $\times$ 5μm) bridge in the middle for the active region (in red square box). As we discussed in Chapter 2, in this prototype device, the wide Ohmic contacts were chosen to minimize the contact resistances.[2] To couple THz radiation into the active region, a single-slot

[2] Again, a typical value for the specific contact resistance of an Ohmic contact for a modulation-doped GaAs/AlGaAs QW is 1-2 Ω mm, which yields a contact resistance of 200-400 Ω for a 5μm-wide Ohmic contact. To minimize the contact resistances, we chose a 1-mm wide Ohmic contact that yields a contact resistance of 1-2 Ω for each contact.

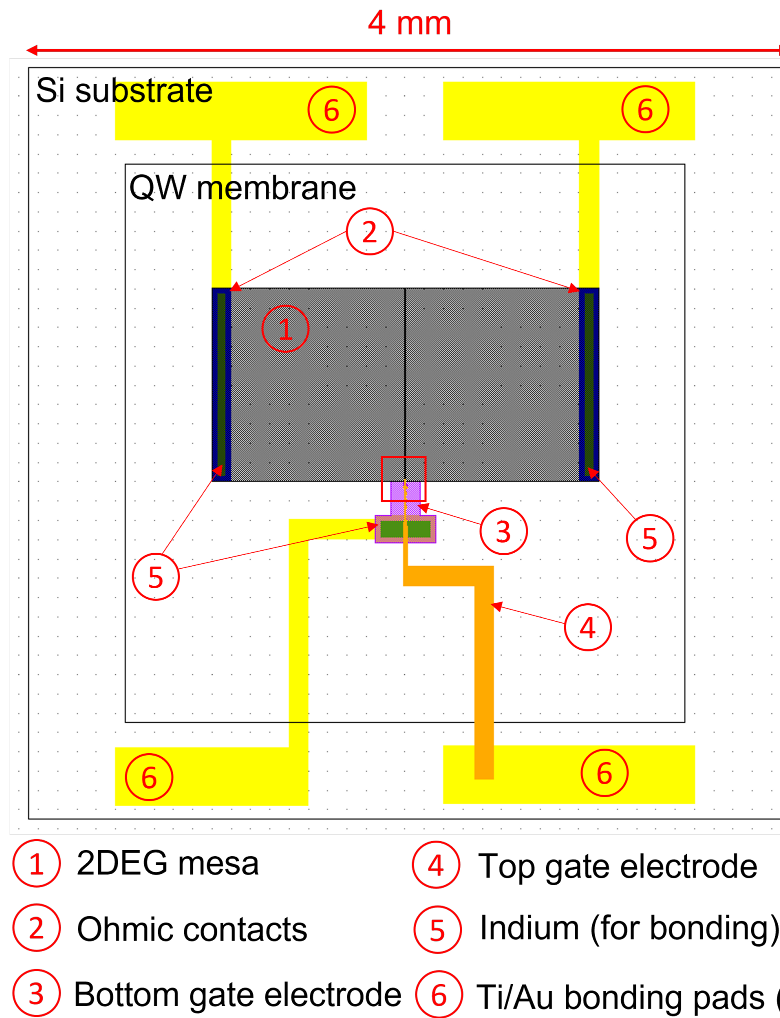

Figure 4.1: Device design for a resistively-coupled TACIT mixer integrated with a single-slot antenna.

antenna is integrated with the bottom-gate electrode (circled 3). The top-gate electrode (circled 4) is aligned with the bottom-gate electrode to form the dual-gate structure required for the tuning of the detection frequency. The two Ohmic contacts and the bottom-gate electrode are defined on the front (buried) side of the QW die and flip-chip bonded to the matching electrodes defined on the Si substrate via indium bonds (circled 5). Finally, wire bonds are made on the bonding pads (circled 6) defined on the Si substrate to electrically access both the front-side contacts (two Ohmic contacts and the bottom gate) and the back-side contact (the top gate).

Figure 4.2 shows the device design near the active region of the device. The slot antenna is integrated with the bottom-gate electrode. To prevent high-frequency current from flowing in the gates, an RF choke is integrated with the top-gate electrode. The top- and bottom-gate electrode patterns are extended to enclose the 5μm $\times$ 5μm active region to provide DC biasing necessary for the tuning of the detection frequency and the device impedance. As we mentioned earlier, the simple design of the single-slot antenna offered straightforward integration with the four-terminal geometry of TACIT mixers.

Fabrication

Figure 4.3 shows a fabricated resistively-coupled prototype TACIT mixer (referred as E2 for the rest of the chapter). The device was fabricated using the IBASE process (see Chapter 3) from a modulation-doped 40-nm square GaAs/AlGaAs QW heterostructures.[3] As we discussed in Chapter 2, the 40-nm QW was chosen to set the intersubband absorption frequency to be near 2.5 THz in the absence of the external DC electric field and without additional charge density in the well (the intrinsic charge density was designed to be near 2×10^{11} cm^{-2}). A Hall measurement on a test Hall bar device later confirmed this charge density, with the measured intrinsic charge density $n_0 = 2.2 \times 10^{11}$

[3]For the details on the QW structure, see Chapter 3.

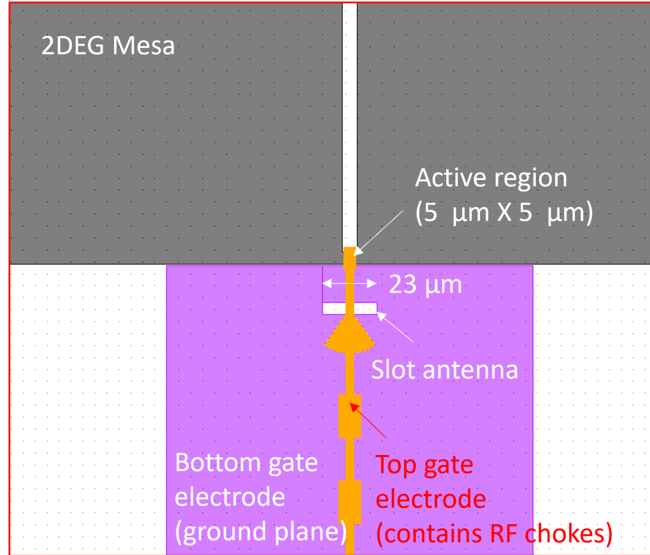

Figure 4.2: Device design near the active region of a resistively-coupled prototype TACIT mixer.

cm^{-2} with high mobility $\mu = 9.4 \times 10^6$ cm^2 at 2 K.

4.2 IV Characterization

After the fabrication, we measured the device current-voltage (IV) curves to check the bolometric response in the device IV curves and to confirm the gating operation of the dual-gate structure. For each IV curve measurement, one of the Ohmic contacts (this will be referred as drain) was grounded, with the other (will be referred as source) being biased with constant DC current. Also, the top gate and the bottom gate were biased to a fixed voltage relative to the drain to avoid fluctuations in the charge density throughout the measurement.

Figure 4.4 shows the IV curves of E2 at 50 K with varying charge density in the active region. The top gate voltage was varied from -2 V to 1 V with the bottom gate fixed to 0 V to effectively vary the charge density set by the sum voltage ($V_T + V_B$; see Eq. 2.2). We observed tunable bolometric response in the IV curves, from being completely

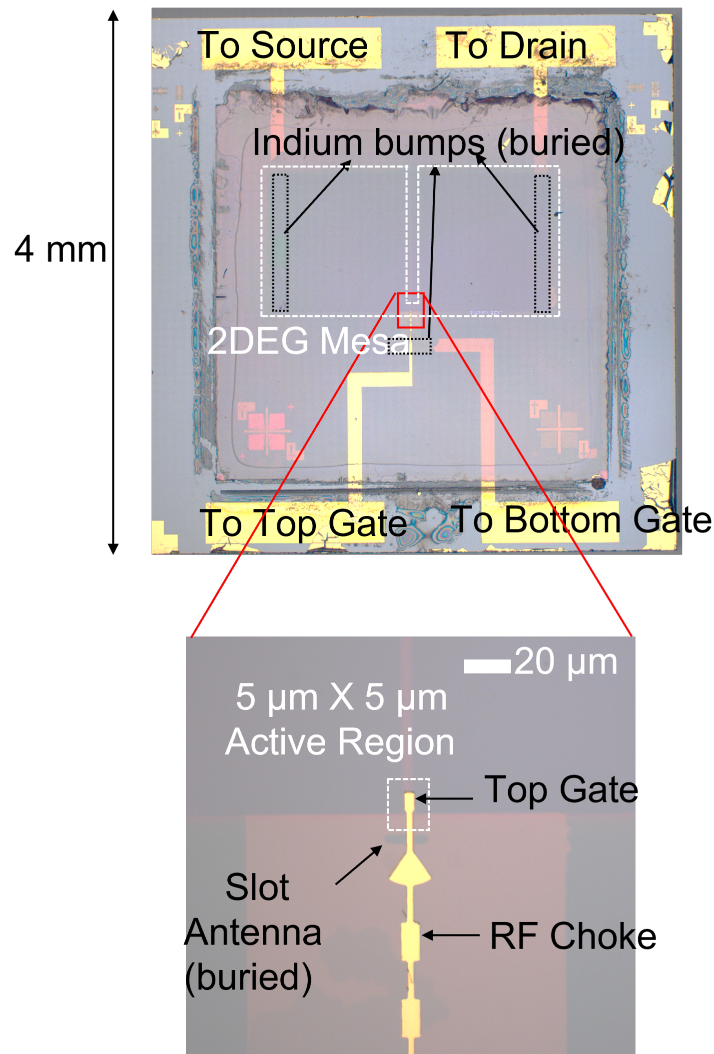

Figure 4.3: Fabricated resistively-coupled prototype TACIT mixer integrated with a single-slot antenna (labelled as E2). The entire device is shown in the top image, with the thin (< 660 nm) GaAs/AlGaAs QW heterostructure membrane (in pinkish color) containing the 2DEG mesa (marked with white dashed lines). The thin QW membrane is bonded to a high-resistivity Si substrate (grey in color). The active region of the device is shown in the inset below, with a slot antenna defined on the bottom-gate electrode and an RF choke on the top-gate electrode. The terminals defined on the front (buried) side of the device were indium-bonded with the matching Ti/Au electrodes defined on the Si substrate. Underfill epoxy was used to fill the rest of the bonded area. Au wire-bonds (not shown) were made to the bonding pads on the Si substrate to electrically access the terminals on the buried side (the source, drain, and bottom gate) as well as the top gate on the back (exposed) side of the QW membrane.Reproduced from [59], with the permission of AIP Publishing.

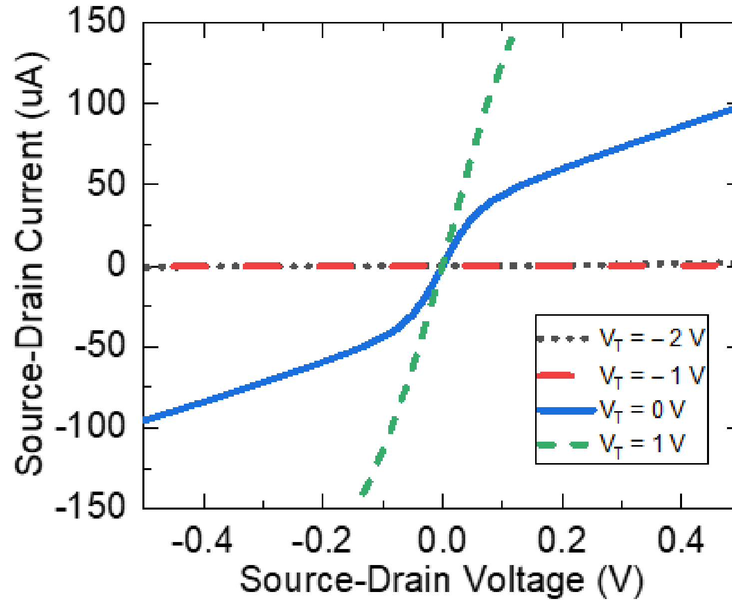

Figure 4.4: Current-voltage (IV) curves of E2 at 50 K showing the tunable bolometric response in the IV curve for TACIT mixers. The charge density in the active region is tuned with the sum voltage $V_{\text{Sum}} = V_T + V_B$, which results in different bolometric response in the device IV curves. Here, only top gate voltage V_T was varied from -2 V to 1 V with the bottom gate voltage V_B fixed to 0 V. Reproduced from [59], with the permission of AIP Publishing.

flat (when the active region is depleted of electrons; see the black and red curves), to showing non-linearity due to electron heating (when there are enough electrons in the active region for heating; see the blue curve), and even to being completely linear (when there are too many electrons to be heated in the given bias range; see the green curve). We observed similar tunability in the IV curve by varying the bottom gate bias voltage, confirming the gating operation of both gates within the tested range of the voltage biases. The device resistance at the source-drain bias of 50 mV was $\sim$500 Ω at $\mathrm{V_T} = 1$ V. Compared with the 2DEG sheet resistance of $\sim$60 $\Omega/\square$ measured at 50 K in a Hall bar sample, the high device resistance at $\mathrm{V_T} = 1$ V is attributed to large 2DEG contacts and to additional parasitic resistance from current crowding near the active region of the device.

4.3 THz Measurements

Direct detection and heterodyne detection were performed to verify the tunability in the detection frequency and the THz mixing capability for TACIT mixers. For direct and heterodyne detection measurements, a hyperhemispherical Si lens was used to quasi-optically couple THz radiation to the slot antenna and the active region of the device. The device was glued on the back side of the Si lens, and the mixer block that contains the Si lens was thermally anchored to a cold plate in a liquid helium cryostat which could be warmed up to 60 K. A bandwidth limiting filter was mounted on the LN_2 (77 K) thermal shield of the cryostat to filter any un-wanted thermal radiation coupling to the device.

For direct detection, a CO_2-pumped molecular gas far-infrared (FIR) laser provided THz signals at 2.52 THz and 3.11 THz. The device response was measured using a lock-in amplifier while chopping the THz signal with a mechanical chopper. The schematics for the direct detection is shown in Figure 4.5. For heterodyne detection, THz RF was provided by a tunable solid-state frequency multiplier built at Jet Propulsion Laboratory, and THz LO was provided by the FIR laser. A bias-tee was used to apply DC bias to the source-drain channel and to couple out the IF response, which was amplified with a low-noise microwave amplifier and detected by a spectrum analyzer. The block diagrams for the heterodyne setup is shown in Figure 4.6.[4] For both THz heterodyne and direct detection measurements, the source was biased to 50 mV with the drain being grounded.

[4]This is from the setup for the heterodyne detection for the capacitively-coupled prototype TACIT mixer that will be introduce in Chapter 5. However, the setup for the resistively-coupled TACIT mixer was similar, so this schematic is provided here.

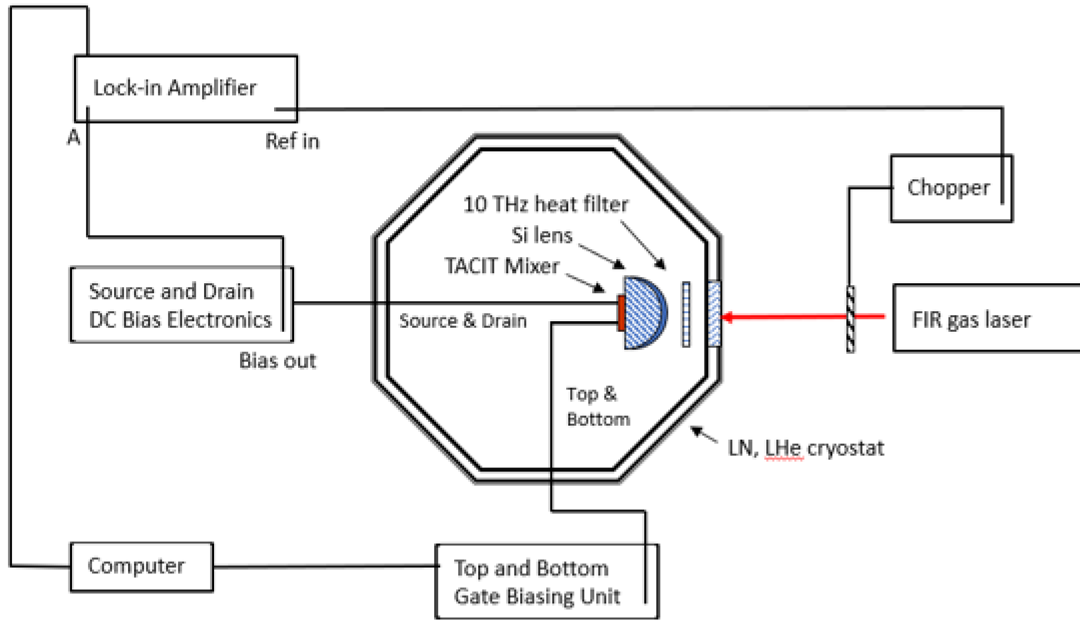

Figure 4.5: Block diagrams for THz direct detection setup.

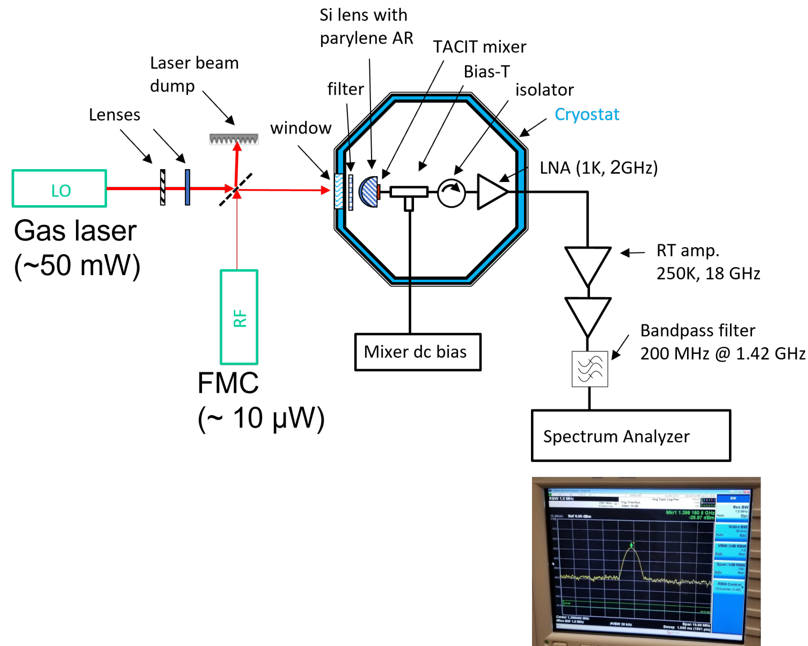

Figure 4.6: Block diagrams for THz heterodyne detection setup.

Direct Detection Results

Figure 4.7 shows the direct detection results for E2 at 2.52 THz and 3.11 THz at 36 K (Figures 4.7(a) and (b)) along with the calculated absorption frequency at the same temperature (Figure 4.7 (c)). Figures 4.7(a) and (b) show the device responsivities at 2.52 THz and 3.11 THz as a function of the effective DC electric field, which was converted from the difference voltage ($V_{Diff} = V_T - V_B$; marked on the top of the plot) using Eq.2.3. The curves were shifted horizontally with an offset of -0.98 mV/nm to cancel out a built-in electric field in the quantum well. Each curve in the plot corresponds to a single charge density value set by the sum voltage ($V_{Sum} = V_T + V_B$). The inset in Figure 4.7(b) shows similar double-peak behavior at 3.11 THz at 60 K. The tuning curves shown in Figure 4.7(c) were calculated by self-consistently solving the Schrödinger equation to calculate the intersubband absorption frequency for the intersubband transition between the first and the second subbands in a 40-nm GaAs/AlGaAs QW (see Chapter 2 and Appendix B for more information on the calculation).

The observed device responses at 2.52 THz and 3.11 THz (Figures 4.7(a) and 4.7(b)) show tunability in the detection frequency consistent with the absorption behavior predicted by the calculation (Figure 4.7(c)). For 2.52 THz, we observed single peaks in the responsivity curves with the width of the peak increasing with increasing charge density. This behavior is consistent with the theoretical model shown in Figure 4.7(c); the bottom dashed line at 2.52 THz intersects the tuning curves near the bottom where there is a range of the field values at which the incoming THz radiation matches the absorption frequency. The range of these field values broadens with the increasing charge density. For 3.11 THz, we observed double peaks with the position of the peak shifting outward in the electric field with increasing charge density. These shifts in the peak position are consistent with the tuning curves in Figure 4.7(c) as the top dashed line at 3.11 THz

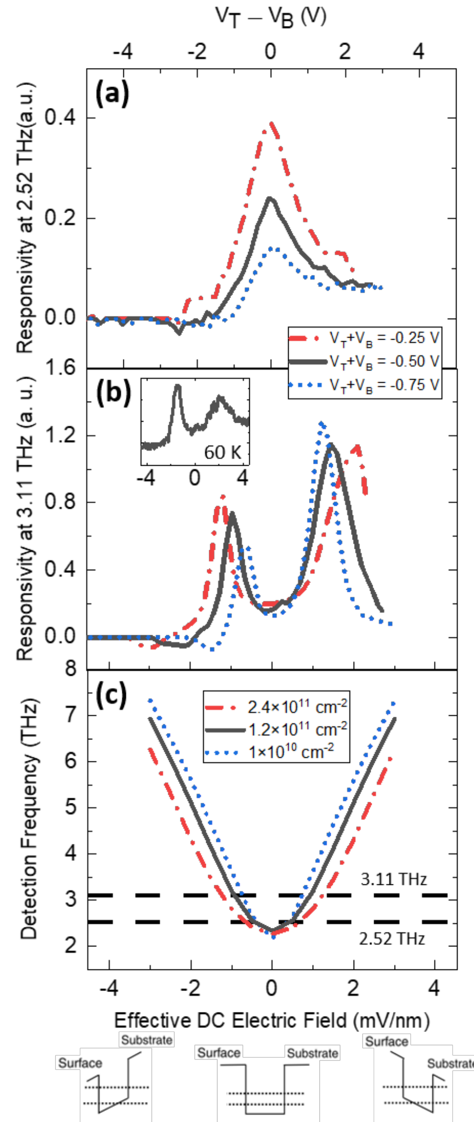

Figure 4.7: Direct detection results for E2 at 2.52 THz and 3.11 THz at 36 K. For the measurement, the charge density in active region was first set by the sum voltage $V_{Sum} = V_T + V_B$, and the response was measured as we sweep the DC electric field (applied along the growth direction of the QW) with the difference voltage $V_{Diff} = V_T - V_B$ while fixing V_{sum}. Each curve in the plots corresponds to a fixed charge density. (a) Responsivity at 2.52 THz at 36 K.(b) Responsivity at 3.11 THz at 36 K. The inset shows the 3.11 THz response at 60 K. (c) Calculated intersubband absorption frequency as a function of the DC electric field at 36 K. The inset shows the charge density values assumed for the calculation. The simplified QW diagrams at the bottom of the figure show the tilting of the QW and the change in the subband energy spacing as a function of the applied field. Reproduced from [59], with the permission of AIP Publishing.

intersects the curves at more negative and more positive electric fields for a higher charge density.

We also observed side peaks at high field biases ($\pm\sim$2 mV/nm) for 2.52 THz and asymmetry in the amplitude of the two peaks at 3.11 THz. The side peak at the positive field bias above 1 mV/nm at 2.52 THz and the asymmetry in the two peaks at 3.11 THz may be associated with the leakage at the top gate. In the fabricated device, the top gate metal was directly deposited on the semi-insulating GaAs cap layer shortly after removing the native oxide layer, and forms a Schottky gate that has a threshold voltage of $\sim$1 V. Above the field value of 1 mV/nm, the top gate bias starts to exceed the threshold voltage, resulting in the gate leakage that leads to small artifacts in the responsivity amplitude.[5] In addition to the side peaks at 2.52 THz and the asymmetry at 3.11 THz, we observed negative values in the responsivity curves for 3.11 THz at negative field biases. While we do not know at the moment what causes the negative values in the device response, it is likely that the negative signal is an experimental artifact due to the phase shift arising from the unfavorable combination of the device impedance and the capacitance of the bandwidth limiting filter as only the in-phase component of the response was recorded using the lock-in amplifier.

Heterodyne Detection Results

Figure 4.8 shows the result of the heterodyne detection at 2.52 THz at 60 K. We observed IF signals in the GHz range, confirming the THz mixing capability of TACIT mixers at 60 K. The frequency dependence of the IF response shows that the -3dB bandwidth exceeds 6 GHz. The frequency spectrum was not fitted with the single-pole Lorentzian because of the 12dB/octave roll-off that suggests the existence of higher-order

[5] In future devices, we may avoid the breakdown of the gate by having a thin oxide layer between the gate metal and the GaAs cap layer.

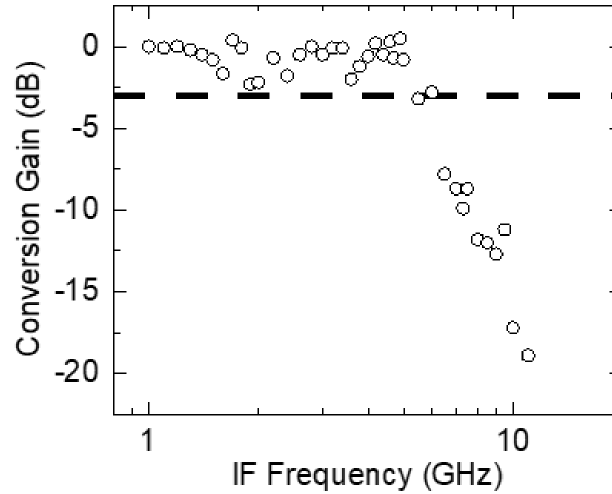

Figure 4.8: Frequency dependence of the normalized IF response for E2 at 2.52 THz at 60 K. The dashed line indicates the -3dB point.

filtering possibly due to parasitic reactance of the on-chip IF circuitry. This essentially limits the observed IF bandwidth of the fabricated TACIT mixer, which we expect to be $\sim$ 10 GHz otherwise based on the previous work by M. Lee et al[35]. In his two-terminal 2DEG-based HEB device, an IF bandwidth of $\sim$ 10 GHz was observed at 77 K for the device with its length similar to the length of the active region ($\sim 5\mu m$) of the prototype TACIT mixer.

Follow-up Direct Detection Results

After the first round of THz characterizations for E2, we performed an additional round of direct detection as a follow-up measurement to further study the tunability in TACIT mixers. The follow-up measurements were done for 2.52 THz, 3.11 THz, and 3.44 THz. The FIR molecular gas laser provided monochromatic radiation at 2.52 THz and 3.11 THz with nominal power of 60 mW for 2.52 THz and 30 mW for 3.11 THz. A Quantum Cascade Laser (QCL), fabricated by Dr. Chris Curwen at Jet Propulsion Laboratory, provided monochromatic radiation at 3.44 THz with a nominal power of 4

mW. For 3.11 THz, the polarization was opposite to the polarization we need for E2, but no attempt was made to rotate the polarization.

Figure 4.9 shows the direct detection results for 2.52 THz, 3.11 THz, and 3.44 THz. Compared with the previous direct detection results, we saw similar absorption behavior, with a notable difference in the gate condition of the device. As in Figure 4.7, we observed a single peak behavior for the response at 2.52 THz and the same trend in the shifts in absorption peaks over different charge densities for all three THz frequencies, with the positions of the peaks shifting outward with increasing charge density with increasing amplitude. This trend is consistent with what we predict with the tuning curves shown in Figure 4.7 (c), as well as the previous direct detection results shown in Figure 4.7. Also, note that, for 3.44 THz, the positions of the peaks are shifted further to the left compared with the peaks for 3.11 THz, which is also predicted with the tuning curves.

One noticeable difference in the second round of direct detection is the absence of the second peaks for the device response for 3.11 THz and 3.44 THz (see Figure 4.9 (b) and (c)). One likely explanation for this is the possible degradation in the gates, which may have caused premature breakdown in the gates before we reach more positive V_{Diff} where we expect the second pair of peaks. This is also supported by the fact that we had to apply roughly twice more negative V_{Diff} than we needed for the previous direct detection to observe the first pair of the peaks for 3.11 THz (the left peaks in Figure 4.7 (b) and the peaks in Figure 4.9 (b)).[6] This gate breakdown is most likely a result of consistently applying difference voltages higher than the threshold voltages over several runs of direct detection sweeps. This is mostly due to the lack of experience in working with the gate structures in TACIT mixers, as E2 was the very first prototype TACIT mixer that we characterized. For more recent capacitively-coupled TACIT mixers, a care

[6] While the two measurements were taken at slightly different temperatures of 36 K and 20 K, we expect the shifts in the peaks associated with the different temperature are small, compared with the observed difference in the required difference voltage.

has been taken by limiting the difference voltage applied to the gates to avoid the possible gate degradation over time, and no sign of gate degradation was observed so far in the capacitively-coupled TACIT mixers.

For this set of direct detection results, we also attempted to reproduce the observed absorption spectra based on the RF impedance model for TACIT mixers (see Chapter 2). In modeling the absorption behavior, we calculated the impedance matching efficiency between the RF impedance of the TACIT mixer ($Z_{RF} = R_{RF} + iX_{RF}$) and the impedance of the THz antenna ($Z_{ant} = R_{ant} + iX_{ant}$), which the response of the device should be proportional to. The matching efficiency α is given by the following formula:

$$\alpha = \frac{4R_{ant}R_{RF}}{(R_{ant} + R_{RF})^2 + (X_{ant} + X_{RF})^2} \tag{4.1}$$

where we will use the calculated values for R_{RF} and X_{RF} based on our RF model (see Chapter 2) and the estimated values for R_{ant} and X_{ant} from a finite-element method (FEM) simulation using ANSYS High Frequency Structure Solver (HFSS).[7] In calculating the RF impedance for the device, we used sub-optimal HWHM values of 100 GHz for 2.52 THz, 200 GHz for 3.11 THz, and 220 GHz for 3.44 THz,[8] which are reasonable considering the fact that the linewidth is likely broader in this prototype device due to its inferior surface.

Figure 4.10 shows the calculated model responses for 2.52 THz, 3.11 THz, and 3.44 THz. Since the conversion of the DC electric field to the difference voltage no longer follows Eq. 2.3 for E2 due to the possible gate degradation, we converted the DC electric fields in the model results to the difference voltages using a linear calibration curve ac-

[7]See Appendix D for the details in the simulation results for the antenna structures. As for the antenna impedance for the single-slot antenna, the geometric capacitance of the active region was detuned from the calculated antenna impedance to avoid double-counting the geometric capacitance (it is already included in the device RF impedance).

[8]These values are roughly twice greater than the optimal values.

quired by comparing the peak positions between the model and the data for the response at 3.11 THz. The model responses reproduce most of the qualitative behaviors of the observed absorption spectra relatively well, including the single/double-peak behaviors (with the absence of second peaks for the experimental curves at 3.11 THz and 3.44 THz due to the gate breakdown), the outward shifts in the peak positions over increasing charge densities, and the increasing amplitudes of the peaks over increasing charge densities. To quantitatively evaluate the calculated matching efficiency, further work on more accurately estimating the antenna impedance may be necessary.

Limitations

As we mentioned earlier in the chapter, this prototype TACIT mixer had a poor conversion efficiency and no attempt was made to measure the noise temperature of the device. We attribute the poor conversion efficiency to the following three factors: poor performance of the sub-optimal single-slot antenna, possible degradation in the IF response due to faster cooling mechanisms including diffusion and ballistic cooling, and the poor IF matching efficiency due to parasitic impedances introduced with the large 2DEG contacts. For the antenna, we later found out that the current design of the slot antenna is resonant at a much lower THz frequency of 1.93 THz[9], resulting in small antenna impedances at 2.52 THz and 3.11 THz (see Appendix D). Also, the single-slot antenna in the current design has poor radiation efficiency (see Appendix D again), which likely resulted in poor coupling of THz RF and LO between the free space and the active region of the device.

Also, the degradation of the IF response is possible with faster cooling mechanisms such as diffusion cooling and even ballistic cooling available for our 2DEG above 20 K.

[9] This is roughly set by the length of the slot $L = \lambda/2$

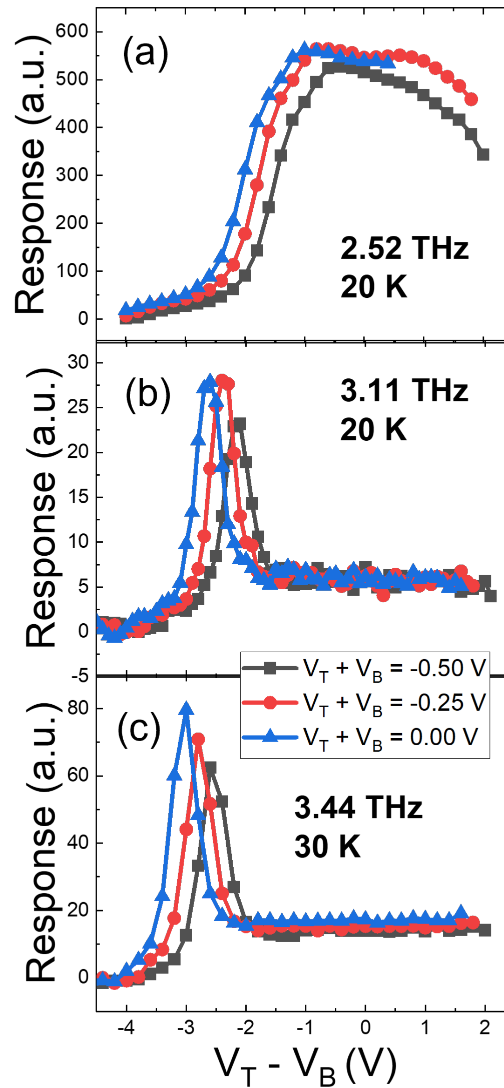

Figure 4.9: Follow-up direct detection results for E2 at 2.52 THz, 3.11 THz, and 3.44 THz. The measurements for 2.52 THz and 3.11 THz were done at 20 K. For 3.44 THz, the measurement was done at 30 K. The legends indicate the sum voltages that correspond to different charge densities in the active region of the device (E2).

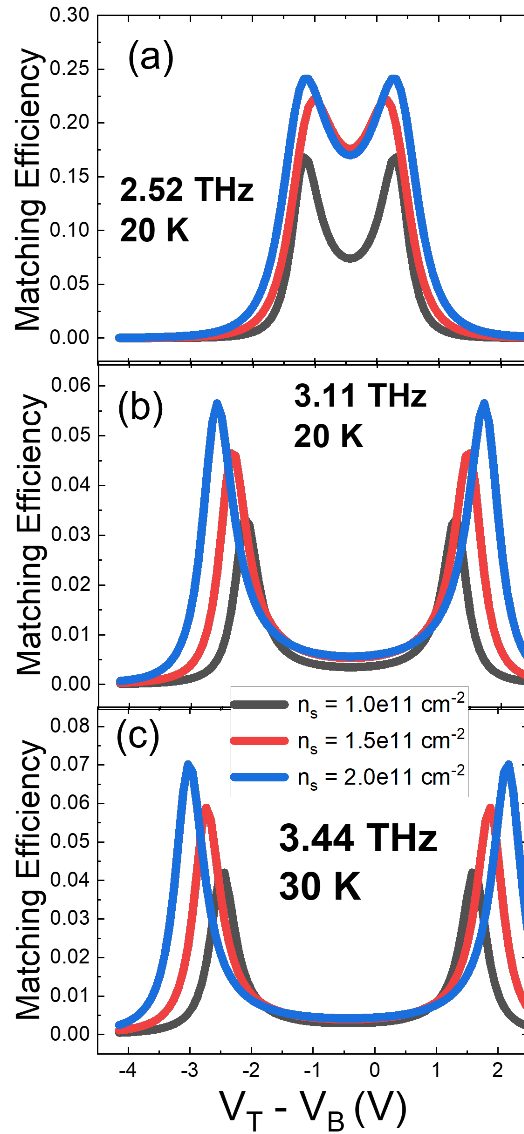

Figure 4.10: Model responses based on the impedance model for intersubband transitions. The impedance matching efficiency was calculated based on the calculated RF impedance of the device and the antenna impedance simulated with a finite-element method (FEM) simulation software (ANSYS HFSS).

We look into this more carefully in Chapter 5.[10] Lastly, the IF impedance matching efficiency is expected to be rather poor for the current resistively-coupled TACIT mixer due to the significant parasitic impedances introduced with the large 2DEG contacts, which adds additional loss to the conversion efficiency. Fortunately, we already saw in Chapter 2 that we can address this by coupling out the IF response capacitively with the help of additional capacitive metals connected with the Ohmic contacts of TACIT mixers; the design, fabrication, and characterization of such capacitively-coupled TACIT mixers will be the main topic of the next chapter.

[10]This is because, (spoiler alert) we saw similar poor conversion efficiency in the capacitively-coupled TACIT mixers.

Chapter 5

Capacitively-coupled Device

In Chapter 2, we first proposed the idea of using capacitively coupling to read out the IF response of TACIT mixers to reduce the parasitic contact impedances of the 2DEG. In Chapter 4, we showed that these parasitic impedances can be indeed one of the factors that may have degraded the conversion efficiency of the resistively-coupled TACIT mixers. In this chapter, we finally introduce capacitively-coupled TACIT mixers in full detail by exploring their design, fabrication, and characterization results. These capacitively-coupled TACIT mixers are integrated with bow-tie antenna structures modified with the addition of two capacitive metals on the 2DEG contacts. As a result, the capacitive contacts also constitute a part of the antenna structures, resulting in shapes resembling Maltese crosses.[1]

The characterization results for the capacitively-coupled TACIT mixers include those from IV measurements and THz direct and heterodyne measurements already introduced in Chapter 4, as well as those from additional measurements, including microwave and noise power characterization. For the IV characterization and THz direct and heterodyne measurements, we generally observed similar device responses consistent with the

[1] This design allows for the integration of the additional capacitive contacts without sacrificing the self-complementary (thus broadband) nature of the bow-tie antenna.

previous results in Chapter 4 and with what we expect from the modeling results. One new result for the direct detection includes the confirmation of the polarization of our antenna structure. In addition, for the heterodyne measurement, the tunability in the heterodyne signal was measured from the bias dependence study of the IF signal at 2.52 THz. These two new results will be discussed in more detail later in the chapter.

One notable difference that we observed for the capacitively-coupled TACIT mixers is unexpected sharp, asymmetric non-linear behavior in their IV curves. We later found out that this is an artifact of providing the DC gate biases (V_T and V_B) relative to the drain of the device (instead of referencing them relative to the potential at the 2DEG in the active region), which causes unwanted charge depletion in the active region that leads to the non-linearity. While this is a very sharp non-linearity, it is too slow to follow the IF response in the GHz range. To address this issue, a new gating technique using an analog circuit was developed to reference the gate voltages relative to roughly the potential of the 2DEG at the active region. Additional information on this will be provided in the section that discusses the IV measurements.

The additional characterization results include those from microwave characterization, noise power measurements, and system noise calibration. From the microwave measurements, we extracted the device IF impedance and confirmed that the capacitive contacts indeed substantially reduce the parasitic impedances in the device IF impedance. The shunting operation agrees well with the IF model that we developed in Chapter 2. In addition, the output power at 1.4 GHz was measured as a function of the source-drain bias; its qualitative behavior agrees well with the behavior of the output noise temperature we presented at the end of Chapter 2. Lastly, the IF system noise was calibrated for our heterodyne setup (shown in Figure 4.6); unfortunately, a rather large IF matching loss (-14 dB) was measured near 1.4 GHz at 10 K. This was a bit unexpected as we already confirmed that the IF impedance becomes small at 1–2 GHz with the help of the

capacitive contacts. While we are still investigating this, sub-optimal gate bias condition for the device used for the calibration and possible electrical problems in the IF line are two likely causes of such high IF loss.

As we alluded in Chapter 4, we still observed large conversion loss in the capacitively-coupled TACIT mixers. As a result, the mixer noise temperature was again not measured in these devices. We attribute this to the same three factors introduced in Chapter 4: the poor performance of the antenna, possible degradation in the IF response due to diffusion and ballistic cooling, and mismatches in IF and RF impedances. We will evaluate these more quantitatively at the end of this chapter and briefly discuss plans to address these issues.

5.1 Device Design and Fabrication

Design

Figure 5.1 illustrates the device design for a capacitively-coupled TACIT mixer integrated with a modified bow-tie antenna. The device has a ribbon-shaped 2DEG mesa (circled 1) with two $300-\mu$m wide Ohmic contacts (circled 2) and a $5\mu\text{m}\times5\mu\text{m}$ active region at the center of the device.[2] To reduce the IF impedance at GHz frequencies, capacitive contacts (circled 3) are placed to cover most of the 2DEG contact areas. The two bows of the bow-tie antenna are integrated with the bottom gate electrode (circled 4) and the top-gate electrode (circled 5). Together with the two capacitive contacts, they form a self-complementary structure (in the form of a Maltese cross) intended to preserve the self-complementary nature of the antenna for its broadband operation. The two Ohmic contacts and the bottom-gate electrode are defined on the front (buried) side

[2] As we discussed in Chapter 2, the wide contacts are chosen to reduce the contact resistance of the Ohmic contacts (see Chapter 2 for more detail).

of the QW sample and flip-chip bonded to the matching electrodes on the Si substrate via indium bonds (circled 6). Finally, the bonding pads (circled 6) defined on the substrate provide electrical access to both the front(buried)-side contacts (two Ohmic contacts and the bottom gate) and the back-side contact (the top gate).

Figure 5.2 shows the device design near the active region of the device. The design shows the two bows of the antenna integrated with the top-gate and the bottom-gate electrodes (orange and violet) and the capacitive contacts (green) covering most of the area in the 2DEG mesa. The top- and bottom-gate electrode patterns are extended to enclose the 5μm $\times$ 5μm active region to provide DC bias voltages necessary for the tuning of the detection frequency in the TACIT mixers.

Fabrication

Figure 5.3 shows a fabricated capacitively-coupled TACIT mixer (this device will be referred as 5505B for the rest of the chapter). The device was fabricated using the IBASE technique based on a similar single 40-nm square GaAs/AlGaAs QW with slightly higher doping density in the Si doping layers. Further optimization in the back-side processing steps (epoxy underfill and backside GaAs removal) led to improvement on the stability and the operation of the gates in this device, requiring smaller (< 1 V) DC voltage biases to access all the DC electric field (applied along the growth direction of QW) and the charge density values required for the tuning of the detection frequency.

An additional device (labelled as 3305A) was fabricated before 5505B, but it turned out that the dual gates in this device only work within a narrow range of the bias points. This device was used only for the microwave measurements.

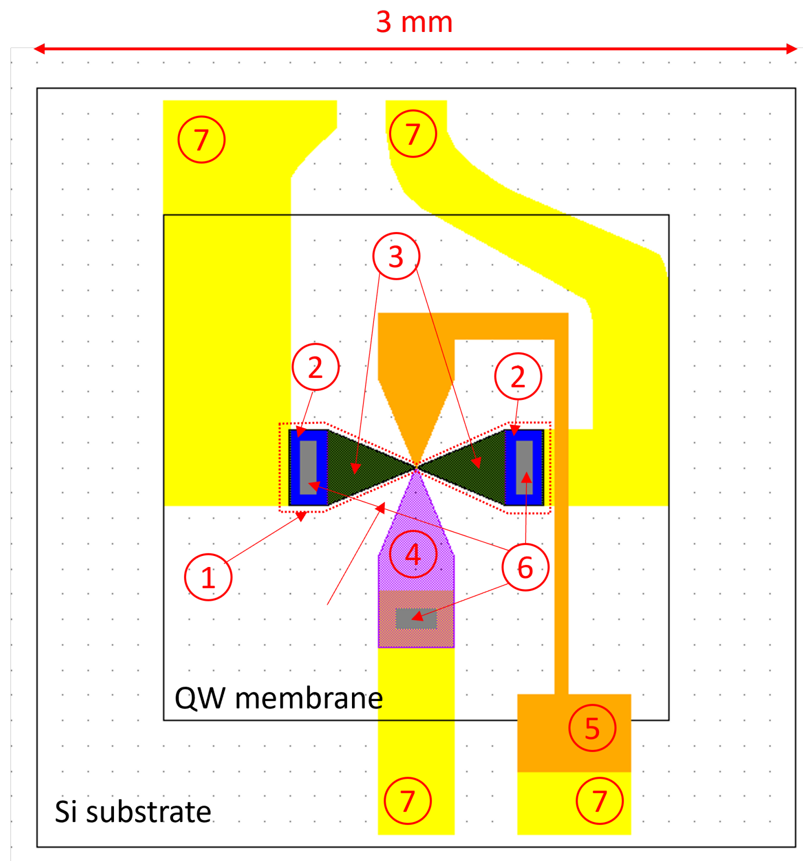

1 2DEG mesa
2 Ohmic contacts (blue)
3 Capacitive contacts (green)
4 Bottom gate electrode (violet)
5 Top gate electrode (orange)
6 Indium (grey)
7 Ti/Au bonding pads (on Si)

Figure 5.1: Device design for a capacitively-coupled TACIT mixer integrated with a modified bow-tie antenna.

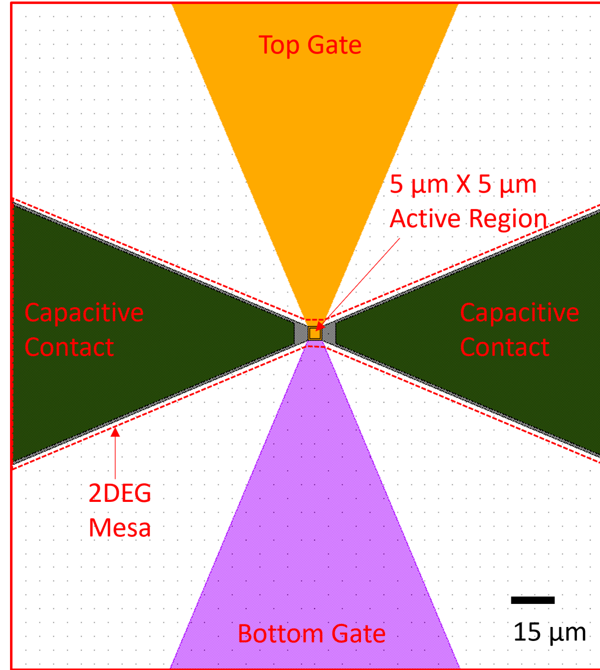

Figure 5.2: Device design near the active region of a capacitively-coupled TACIT mixer integrated with a modified bow-tie antenna.

5.2 IV Characterization

After the fabrication of 5505B, we measured the device IV curves to check its bolometric response and its gating operation. As mentioned in Chapter 4, the gate voltages (V_T and V_B) were initially applied in terms of the sum and the difference voltages ($V_{Sum} = V_T + V_B$ and $V_{Diff} = V_T - V_B$) with respect to the ground (drain; one of the Ohmic contacts), and the source (the other Ohmic contact) was biased with constant DC current to measure the DC voltage across the source and the drain.

Figure 5.4(a) shows the IV curve from the initial measurement at 10 K with $V_T \sim 0$ V and $V_B = -0.40$ V. Unexpectedly, we saw a sharp non-linearity in the IV symmetric about the zero bias-point. We later found out that this unwanted flattening of the IV curve occurs due to the discrepancy between the nominal voltage biases that we apply relative to the ground of the device and the actual voltages biases "seen" by the 2DEG

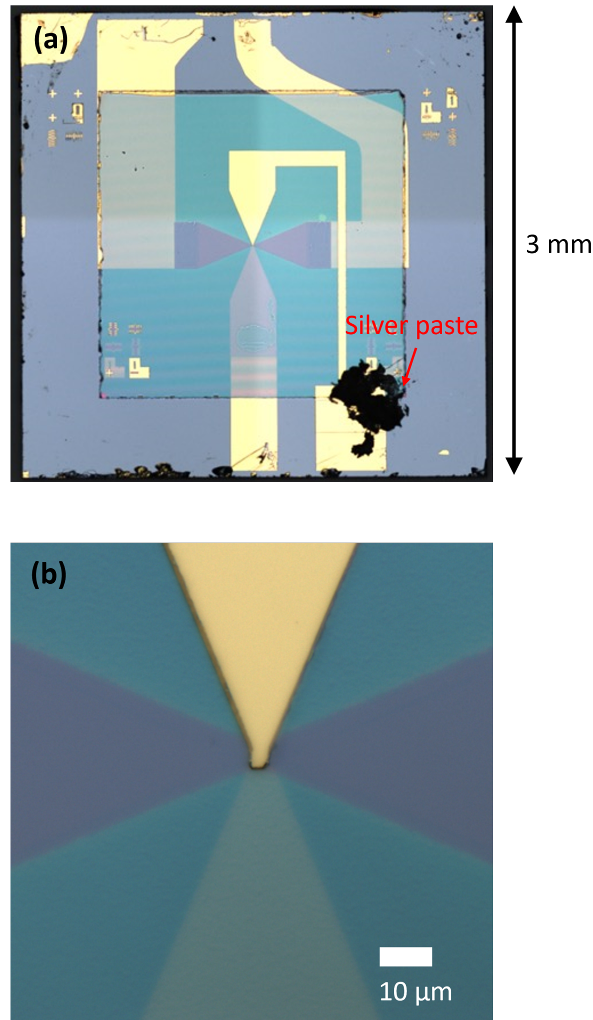

Figure 5.3: Optical microscope images showing a fabricated capacitively-coupled TACIT mixer (labeled as 5505B) (a) Image showing the entire TACIT device, with the thin (660 nm) GaAs/AlGaAs membrane (green) containing the 2DEG mesa flip-chip bonded to the high-resistivity Si substrate (grey). The dark blob on the bottom right bonding pad is a drop of silver paste to ensure the electrical connection between the top gate metallization and the bonding pad. (b) Image showing the active region of the device.

at the active region.

To illustrate this point better, notice that the sum and difference voltage in Eq.2.2 and Eg.2.3 are defined in terms of V_T and V_B relative to the potential of the 2DEG in the active region. In real devices, however, we reference the DC gate biases relative to the drain of the device. The expression for these nominal DC gate biases (V_T' and V_B') can be related to V_T and V_B in Eq.2.2 and Eg.2.3 by recognizing that the potential of the 2DEG at the active region is roughly a half of the source-drain DC bias V_{DS} that we apply due to the symmetry of the device. Then, we have

$$V_{T(B)} = V_{T(B)}' - \frac{1}{2}V_{DS} \tag{5.1}$$

where $V_{T(B)}$ is the DC gate bias seen by the 2DEG at the active region (or the voltage difference between the top (bottom) gates and the active region) and $V_{T(B)'}$ is the nominal DC gate bias we apply relative to the drain of the device in the experiments. In addition, for the sum voltage, we have

$$V_{Sum} = V_{Sum}' - V_{DS} \tag{5.2}$$

where we have $V_{Sum}' = V_T' + V_B'$. The second terms in Eq. 5.1 and in Eq.5.2 explain why we see the asymmetric clipping in the IV curve in Figure 5.4(a); the charge density in the active region is not only affected by the two nominal biases that we apply, but also by the source-drain voltage. For the positive SD bias, this leads to unwanted depletion of the electrons in the active region, causing the sharp flattening behavior (complete depletion in the active region) in the IV. For the negative SD bias, this leads to addition of charge density in the well, causing the asymmetry in the IV in Figure 5.4(a).

While this non-linearity in the IV is very sharp, it is caused by a rather slow process that cannot follow the IF response.[3] To address this issue, we developed a new gating

[3] Indeed, we weren't able to measure the IF response of the capacitively-coupled TACIT mixers

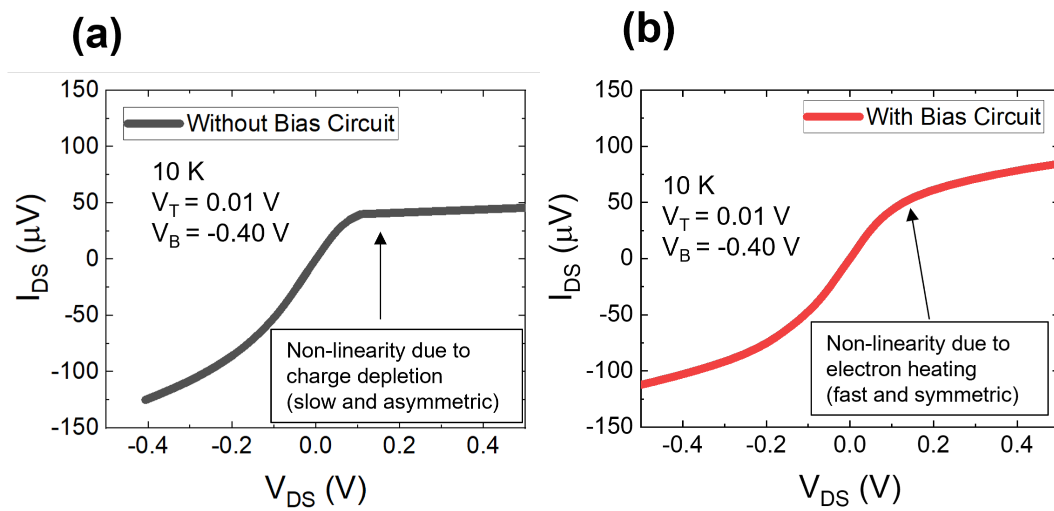

Figure 5.4: IV curves of 5505B measured before and after using a bias circuit. The measurement was done at 10 K with the gate voltages indicated in the plots. (a) Initial device IV curve before using the bias circuit. The sharp, asymmetric non-linearity in the IV is due to the charge depletion in the active region in the conventional biasing scheme. This non-linearity is too slow to follow the IF response in the device. (b) IV curve measured after using the bias circuit. With the new biasing scheme, the charge density in the active region stays the same and we recover the symmetric, fast non-linearity from the bolometric response of the device.

technique in which we use an analog circuit to add the 2DEG potential expected at the active region (which is assumed to be $1/2V_{DS}$ based on the symmetry of the device[4]) to the nominal voltages $V'_{T(B)}$. Figure 5.5 shows the circuit design for the analog circuit consisting of simple voltage dividers and adders; the input for the voltage divider takes in the source-drain voltage and divides it by half to provide new reference voltage (the estimated 2DEG potential at the active region) at one input of the adder circuits; the other two inputs of the bias circuit takes in $V'_{T(B)}$ and feed it to the other input for the adders; the outputs of the adder circuits are then fed into the top and the bottom gates such that we now have

$$V_{T(B)} = (V'_{T(B)} + \frac{1}{2}V_{DS}) - \frac{1}{2}V_{DS} = V'_{T(B)}. \tag{5.3}$$

While the use of the bias circuit varies the DC biases that the gates see with V_{DS}, [5], this fixes the potential differences between the gates and the 2DEG, and hence the charge density in the well throughout the IV measurements. Figure 5.4 (b) shows the IV curves measured with the bias circuit that recovers the non-linear effect due to the electron heating.[6] In addition, with the bias circuit, robust tuning of the charge density became possible again and the tunable bolometric responses for TACIT mixers were confirmed (see Figure 5.6).

initially.

[4]This is technically not true as we have capacitive contacts that makes the charge density along the device length non-uniform. But this small non-uniformity is ignored here.

[5]In this regard, the circuit outputs have a rise time of only 120 μs and are fast enough to be used with a typical V_{DS} scan (1ms delay added at each V_{DS} point in the measurement.

[6]IF signal at 1.4 GHz was also observed once we started using the bias circuit for THz heterodyne measurements.

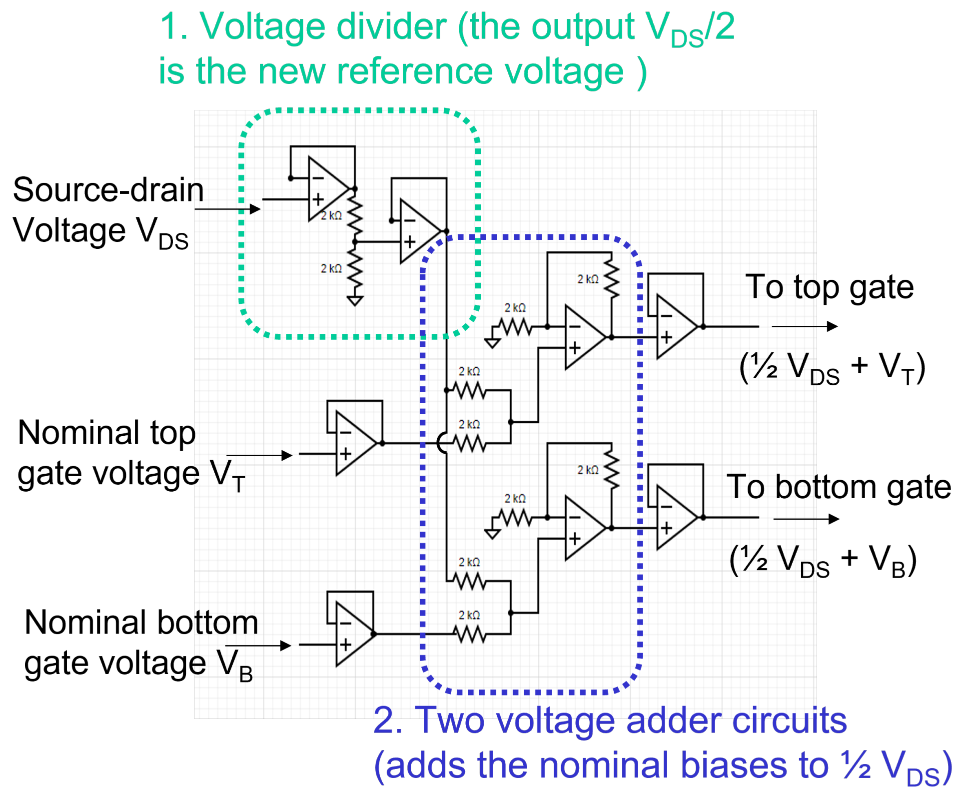

Figure 5.5: Circuit diagram for the bias circuit. One input of the circuit takes the source-drain voltage and divides it by half to provide reference voltage (estimated voltage at the active region). The other two inputs of the circuit take the nominal gate voltages and add them to this reference voltage to keep the voltage difference between the gates and the active region constant throughout the source-drain voltage sweeps.

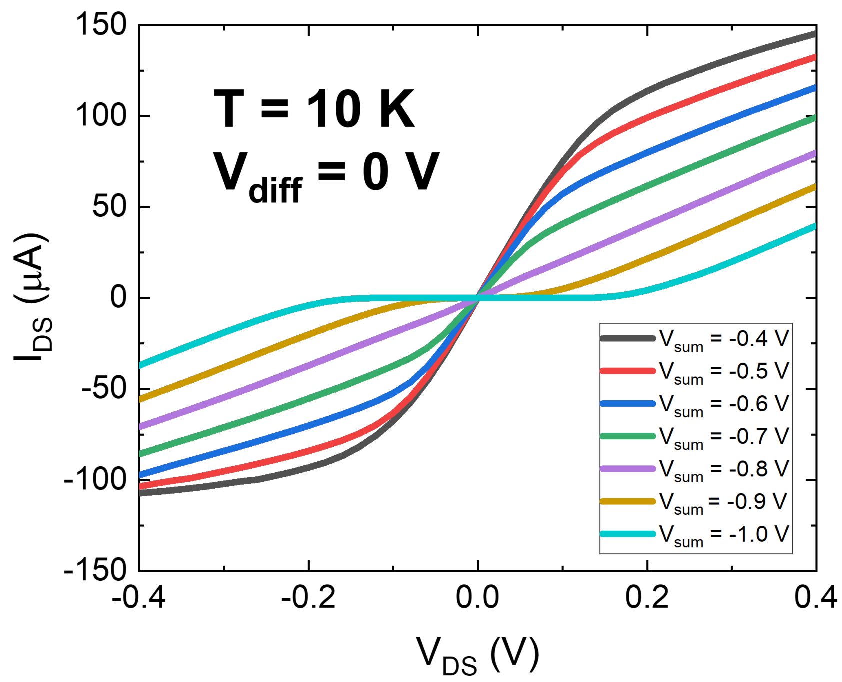

Figure 5.6: Tunable bolometric response in the IV curves of 5505B at 10 K.

5.3 Microwave Characterization

We performed S21 measurements on a capacitively-coupled TACIT mixer (3305A) to study the frequency dependence of the device IF impedance. For the measurements, we used a dip-stick apparatus shown in Figure 5.7. The TACIT mixer was mounted at the bottom end of the dip-stick, and the source-drain channel was connected to the micro-strip lines on the sample mount (shown in the bottom inset in Figure 5.7), with the top and the bottom gates accessed via the DC bias lines. Device 3305A was tuned to the bias points at which the device DC resistance is reasonably stable.[7] Also, the bias circuit introduced in the previous section was not used as relatively small source-drain bias was used for the measurements. For the calibration, a shorting wire was placed in the source-drain channel to measure 100 % transmission and later disconnected for the S21 measurements.

Figure 5.8(a) and Figure 5.9(a) show the frequency dependence of the IF impedance measured at 60 K and 16 K, respectively. These impedance values were extracted from the S21 coefficient using the standard expressions. As shown in the figures, the device IF impedance contains parasitic impedances that significantly contribute to the overall IF impedance at the low-frequency range ($<<$ 1 GHz). These parasitic impedances are shunted out at the higher frequency ($>$ 1) GHz, substantially reducing the overall IF impedance. This shunting behavior agrees well with the model response of the IF impedance simulated with $R_s = 200\Omega/\Box$ for 60 K and $R_s = 150\Omega/\Box$ for 16 K, as shown in Figure 5.8(b) and Figure 5.9(b), respectively. We also highlight that, even after we tune out the parasitic impedances of the 2DEG contacts, the device IF impedance is still rather high compared with 50 Ω, the input impedance for the first IF amplifier. We attribute this large device IF impedance above 1 GHz to the sub-optimal bias points

[7] Device 3305A had somewhat defective gates that only operated well within a narrow range of bias points.

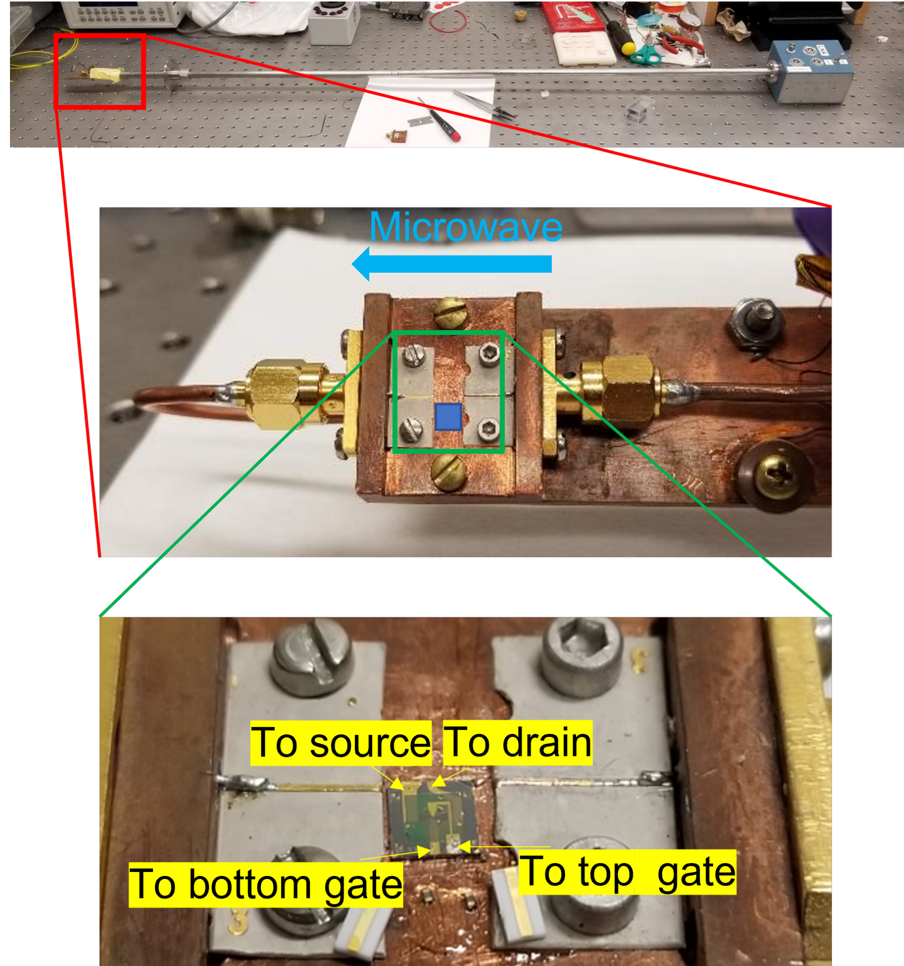

Figure 5.7: Dip-stick apparatus used for S21 measurements for 3305A. The inset in the middle shows the sample holder with the blue square showing the dimension of the TACIT mixer device. The bottom inset shows how we wire-bonded the four terminals of the TACIT mixer with the micro-strip line and the DC bias lines.

we used for the measurements[8] and to the fact there are contributions from the 2DEG contacts that are not covered by the capacitive contacts.

[8]Typically, we measure $R_s \sim 50\Omega at 60K$ with our QW structure. Note that R_s values of 3-4 $\times$ this typical had to be used for the simulation results.

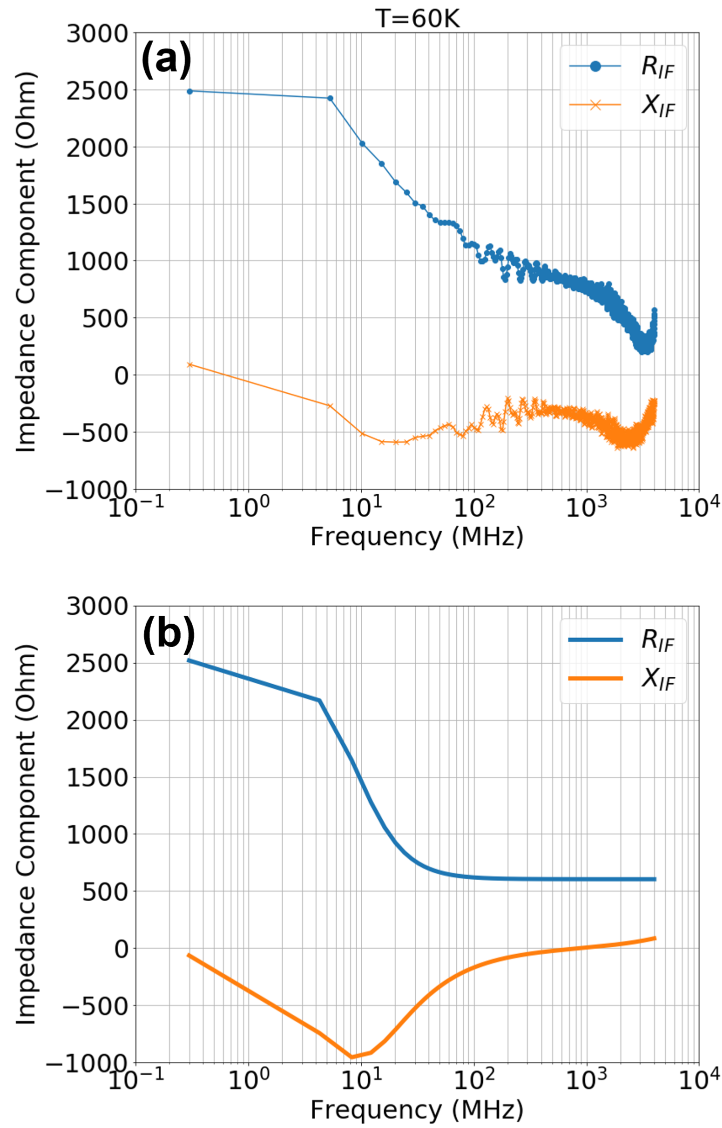

Figure 5.8: (a) IF impedance measured in Device 3305A at 60 K. The IF impedance was extracted from S21 measurements. (b) IF impedance calculated from the IF model with sheet resistance $R_s = 200\Omega/\square$. The coupling efficiency with a $50-\Omega$ load is 28% at ~ 1 GHz.

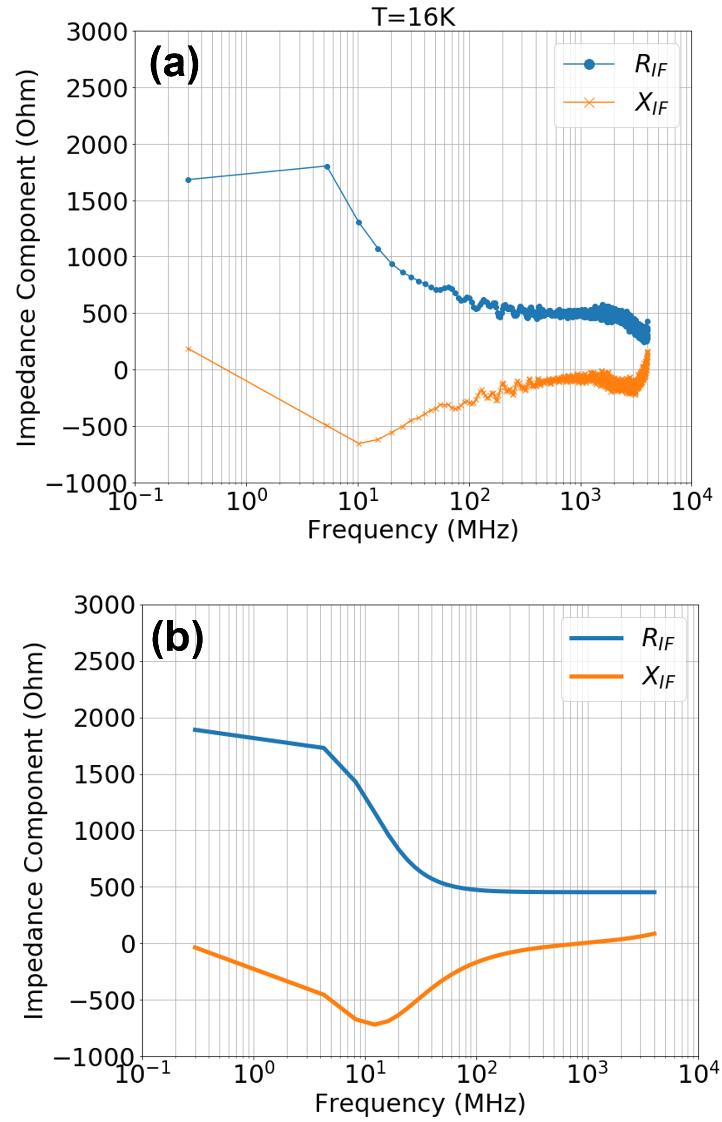

Figure 5.9: (a) IF impedance measured in Device 3305A at 60 K. The IF impedance was extracted from S21 measurements. (b) IF impedance calculated from the IF model with sheet resistance $R_s = 150\Omega/\Box$. The coupling efficiency with a $50-\Omega$ load is 35% at ~ 1 GHz.

5.4 THz Measurements

Both direct detection and heterodyne detection introduced in Chapter 4 were performed for 5505B. The setups for both measurements closely follow those described in Chapter 4, so the description of the experimental setup is omitted here (see Chapter for the details on the setup).

Most of the THz measurements were performed at 10 K, which was the base temperature of our cryostat after LHe fill, with a mylar film inserted between the cold plate and the mixer block.

Direct Detection Results

Direct detection measurements in response to a monochromatic radiation at 2.52 THz and 3.11 THz at 10 K showed the tunability in the detection frequency of TACIT mixers consistent with the previous results presented in Chapter 4 (see Figure 5.10); the direct detection response for 2.52 THz (Figure 5.10(a)) showed the single-peak absorption behavior, and the direct detection for 3.11 THz (Figure 5.10(b)) showed the double-peak absorption behavior with the absorption peaks shifting outward over increasing charge density. No attempt was made yet to reproduce these absorption spectra based on the device RF model as in the follow-up measurements for E2 in Chapter 4. Simulating the model responses are currently underway, especially to understand the decreasing peak response over increasing charge density as seen in Figure 5.10(b).

We also confirmed the polarization of the bow-tie antenna in the direct detection measurements in response to a monochromatic radiation at 2.52 THz. Figure 5.11 shows the direct detection results with cross-polarized beams at 2.52 THz. The results show that the device response for the correctly polarized beam (black curve) is $\sim 57\times$ greater than that for the cross-polarized beam (red curve), confirming that the antenna is polarized

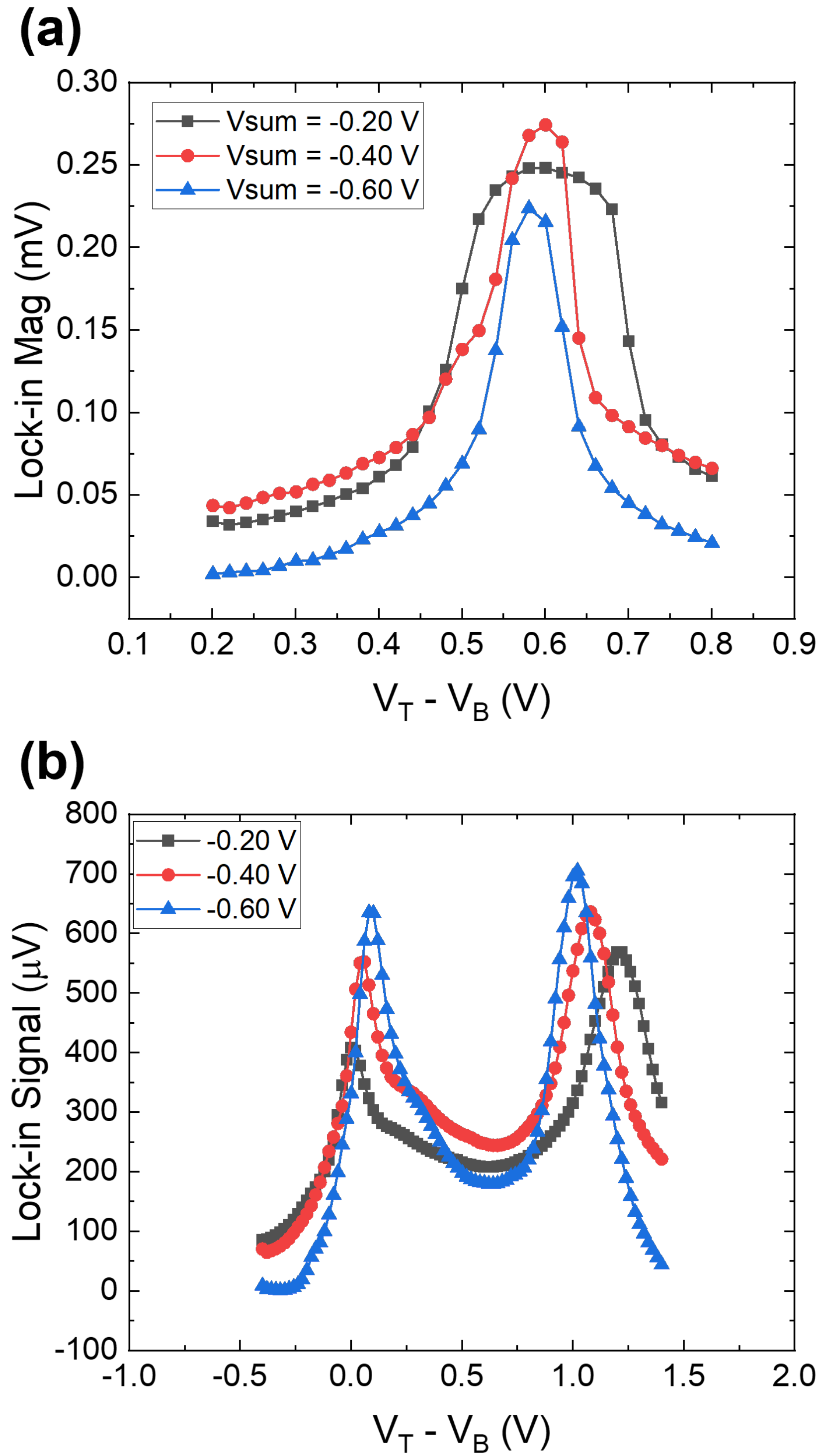

Figure 5.10: Direct detection results for 5505B at 10 K (a) Direct detection results for 2.52 THz (b) Direct detection results for 3.11 THz.

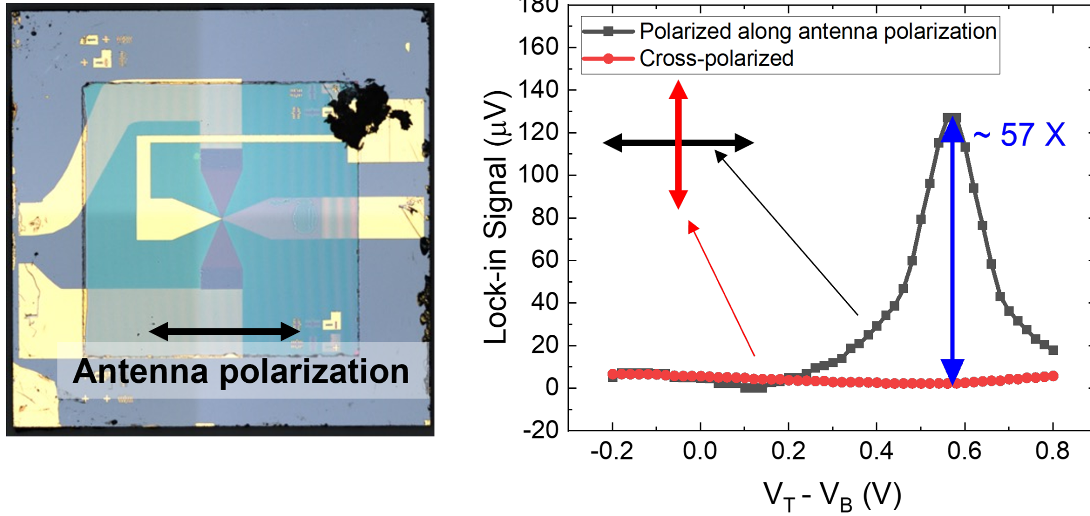

Figure 5.11: Cross-polarization measurements for 5505B with 2.52 THz at 10 K.

as intended.

Heterodyne Detection Results

We performed heterodyne detection near 2.52 THz at 10 K, with the RF and LO $\sim$ 1.4 GHz apart, and observed the corresponding IF response at $\sim$1.4 GHz (Figure 5.12). For the measurement, Device 5505B was biased at $V_{Sum} = 0.00$ V and $V_{Diff} = 0.60$ V based on the direct detection response of the device, and the IF response near 1.4 GHz was monitored with a spectrum analyzer with the THz LO turned on (see the red curve) and off (see the black curve). As shown in the plot, we observed the IF signal near 1.4 GHz, confirming the THz mixing capability of TACIT mixers again.

The dependence of the IF signal on the DC biases (V_{Sum}, V_{Diff}, and V_{DS}) was studied at 10 K. Figure 5.4 shows the peak amplitude of the IF signal near 1.4 GHz as a function of V_{Diff} over three different V_{Sum} values. The observed responses show that the IF signal at 2.52 THz peaks at $V_{Diff} \sim 0.60$ V at which we also saw the maximum direct detection

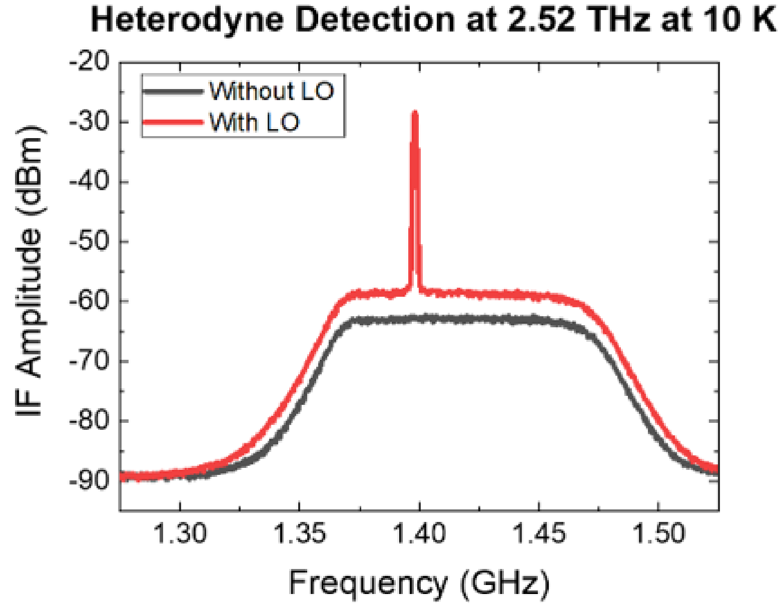

Figure 5.12: Heterodyne detection of 2.52 THz at 10 K, with $V_{Sum} = 0.00V$ and $V_{Diff} = 0.60V$.

response for 2.52 THz. The single-peak behavior in Figure 5.4 is also consistent with the single-peak behavior we observed in the direct detection at 2.52 THz. Note that the IF signal here also depends on the IF coupling efficiency which changes with varying charge density; this is why we see the maximum IF peak amplitude at much higher charge density (see Figure 5.4) than the value at which we saw the maximum RF absorption in the direct detection (see Figure 5.10(a)). Lastly, the tunability in the IF signal shows that the IF signal is quite sensitive to the gate condition, with the peak amplitude varying more than $\sim$ 6 dB with 0.2 V difference in V_{Sum}, highlighting the importance of the precise tuning of the DC gate biases for the optimal operation of TACIT mixers.

5.5 Noise Power Measurements

We performed output noise power measurements to study the dependence of the output noise power on V_{DS} as well as to calibrate the IF system noise. The dependence

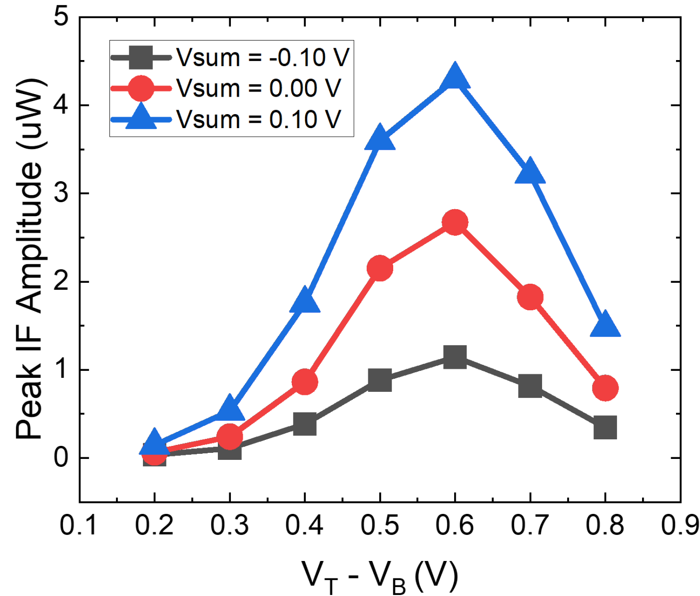

Figure 5.13: Tunability in the IF signal near 1.4 GHz at 10 K.

of the output noise is in good qualitative agreement with what we expect from the output noise power behavior predicted for a HEB mixer in Chapter 2. The IF system noise calibration shows that we still have a high IF coupling loss of roughly -14 dB with Device 5505B.

Dependence of Output Noise Power on V_{DS}

Figure 5.14 shows the output noise power measured at 1.4 GHz (with 100 kHz bandwidth) as a function of V_{DS} at 10 K. The output noise power peaks at the source-drain DC biases near the knee of the current-voltage (IV) curve (see the inset) at which the contribution of the thermal fluctuation noise is expected to be maximum, as expected from our modeling results in Chapter 2. By measuring the noise power at zero source-drain DC bias with and without 2.52 THz LO, we observed the change in the noise power that corresponds to $\sim$ 20 K of electron heating with the THz LO with a nominal power

of $\sim$ 50 mW.[9]

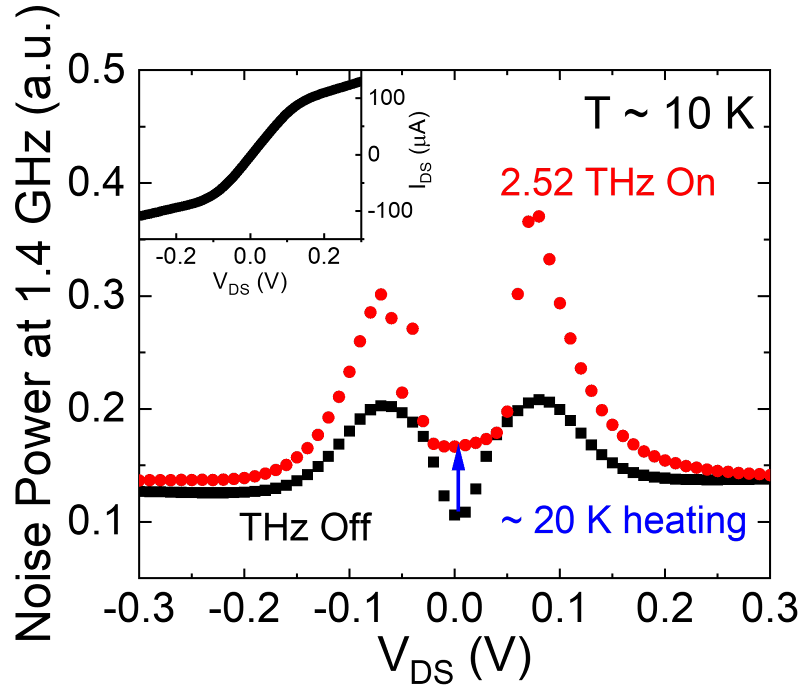

Figure 5.14: The dependence of the output noise power at 1.4 GHz on V_{DS} at 10 K.

Calibration of IF System Noise

The calibration of the IF system noise was performed to evaluate the IF impedance mismatch. The calibration is based on the linear temperature dependence of the output noise power at the IF frequency (1.4 GHz in our case) at $V_{DS} = 0$ V without THz Lo. In this condition, the x-intercept of the linear dependence is related to the IF system noise T_{LNA}/η_{IF} where T_{LNA} is the noise temperature for the low-noise amplifier and η_{IF} is the IF impedance matching efficiency.

Figure 5.15 shows the measurement of the noise power at 1.4 GHz with $V_{DS} = 0$V over different temperatures. The DC gate condition is shown in the plot, with $V_{Sum} = 0.00$ V

[9]This large nominal power implies that the RF coupling efficiency is rather poor in this prototype device.

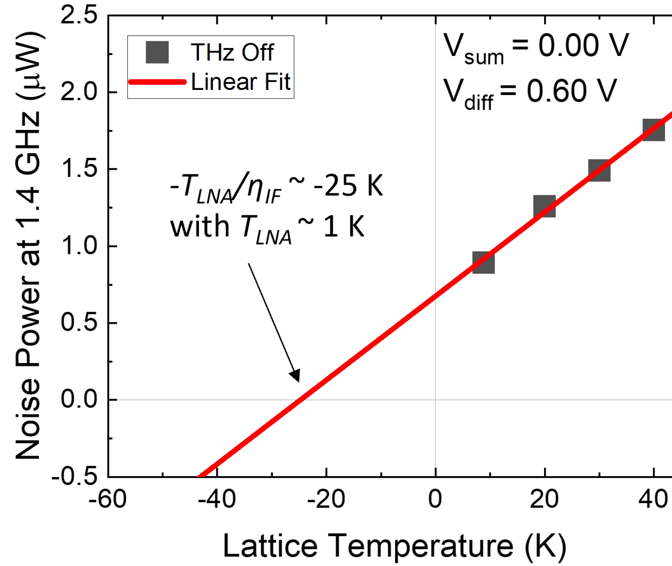

Figure 5.15: Calibration of the system IF noise. An IF coupling efficiency of ~ 0.04 (-14 dB) was estimated from the linear fit.

and $V_{Diff} = 0.10$ V. These gate biases tune the device to its optimal bias point for near optimal IF response. The four data points between 10 K and 40 K (black squares) were fitted with a line (red solid line). The x-intercept from the linear fit was -25 K. With $T_{LNA} \sim 1$ K, we estimate a rather large IF loss of -14 dB. This IF impedance mismatch may imply that the gates were not tuned well enough to their optimal operating points for the maximum IF coupling efficiency (roughly a 3 dB improvement seems possible at a slightly higher V_{Sum} just by looking at the IF peak amplitudes shown in Figure 5.4) or potentially related to the recently observed grounding issue in our IF chain and in our DC biasing setup. We are currently investigating these electrical/grounding issues to address the problem. Also, performing additional calibration runs for at various gate conditions (studying their gate dependence) as well as with additional devices with slight design variations may be helpful in checking if the mismatch originates from the device quality and its operating conditions.

Limitations

As we alluded in Chapter 4 and at the beginning of this chapter, we still observed a poor conversion efficiency in this capacitively-coupled TACIT mixer and no attempt was made to measure the noise temperature in this prototype device. We attribute the poor conversion efficiency to the following two factors: poor performance of our current antenna structures and possible degradation in the IF response due to faster cooling mechanisms including diffusion and ballistic cooling.

To estimate unexplained losses in our system, we indicate the expected or measured losses in our heterodyne system in Figure 5.16. Starting with a nominal RF power of -20 dBm, we expect 10 dB loss in our RF coupling optics. We also estimate -10 to -20 dB loss for the internal loss of TACIT mixers[10]. In addition, we measured roughly -15 dB loss due to IF impedance mismatch. After the mixing, the IF signal is amplified with the low-noise amplifier and the room-temperature amplifiers with a total nominal gain of 75 dB. With these estimated or measured losses in the system, the output power for the IF signal is estimated to be 10–20 dBm. However, we observed a maximum IF power of $\sim$ -25 dBm, resulting in an additional, unexplained loss of 35–45 dB.

To account for this large loss, we first consider the performance of our antenna structures. For the case of single-slot antenna, we already mentioned that the antenna has a poor radiation efficiency (see Appendix D). In addition, the slot antenna with the current design is resonant at 1.93 THz, resulting in a small antenna impedance at 2.52 THz (see Appendix D again), which may also contribute to the poor THz coupling into the device. For the bow-tie antenna, we found out that the radiation pattern with the current design (with a bow length of $\sim 350\mu$m) is highly directional, with most of the radiation

[10]While smaller conversion loss is predicted based on the HEB mixer theory, these values are reasonable and more realistic based on the sub-optimal design for our prototype devices and based on the conversion losses measured in two-terminal 2DEG-based mixers [35, 36].

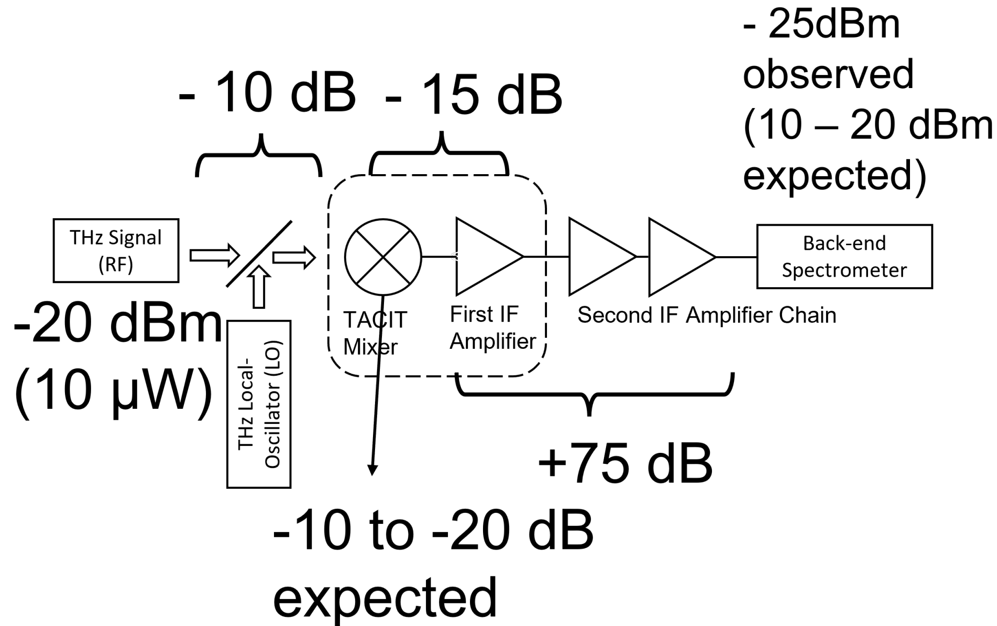

Figure 5.16: Schematic for our heterodyne setup with expected or measured losses in the system.

occurring at an angle greater than 60° from the optical axis. In our quasi-optical setup in which a Si lens typically couple out the radiation from the antenna within the 120° angle centered at the optical axis, this meas that a significant portion of the antenna radiation is not coupled out very well. In terms of a receiving antenna, this means that the THz coupling between the free space and the device is rather poor. For our case, based on the beam pattern provided in Figure 5.17(b), we can estimate that roughly more than 80 % of the radiation occurs outside this 120° angle and is lost. In addition, we expect roughly 7 dB loss from the RF impedance mismatch. [11] Based on these numbers, we expect that we can improve on this RF loss by 10 dB with a further optimized antenna structure.

Also, the degradation of the IF response is possible with faster cooling mechanisms such as diffusion cooling and even ballistic cooling. Indeed, for the critical length L_{crit}

[11]The device RF impedance is estimated to be less than 10 Ω based on the RF model (see Chapter 2) and the antenna impedance is estimated to be roughly 80 Ω (see Appendix D).

at which the diffusion cooling starts to dominate over phonon-cooling for our 2DEG, we have $L_{crit} \sim 5\mu$m, which is comparable to the length of the active region in our current device design. Also, we have the mean free path $L_{mfp} > 10\mu$m for our 2DEG at 20 K, indicating that even ballistic transport is possible in our devices. While it is still hard to put a number on this loss as we are currently investigating this, we expect that this loss is likely the most dominant loss in our device. To address this issue, we are working on using different geometries for the 2DEG in the active region (to trap the electrons longer) as well as using different read-out mechanism based on thermoelectric effect of a 2DEG.

Lastly, a few more words can be added to the IF impedance mismatch that we observed in our device. Although this is already a known loss and not part of the unexplained loss of 35–45 dB, we expect that we can significantly improve on this by improving the quality of the Ohmic contacts to make the overall size of the device a lot smaller; an order of magnitude of improvement on the contact resistance for the Ohmic contacts seems possible, and, with this improvement, we may be able to achieve 10-μm contact that yields only 10 Ω of contact resistance, which can significantly reduce the size of the device. With such small device size, we may expect the possible degradation due to diffusion cooling and the ballistic cooling to be substantially smaller. Lastly, we also learned that precise tuning of the DC gate biases is important not only for the tuning of the detection frequency, but also for the IF coupling efficiency. Also, we learned that the bias condition optimal for the RF absorption may not be the optimal bias point for the IF coupling efficiency. As a result, a care must be taken in the design process to achieve a sweet spot in the bias points that result in good RF as well as IF coupling in the device.

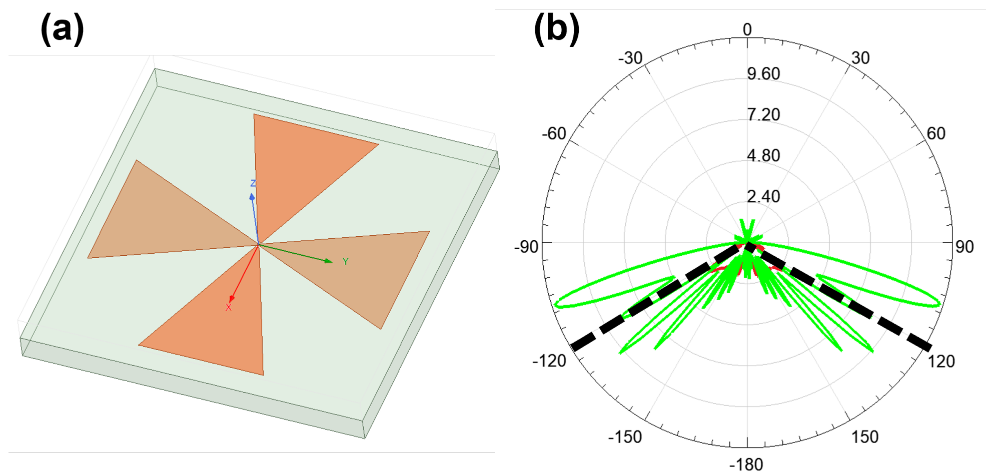

Figure 5.17: Finite-element method (FEM) simulation results for the bow-tie antenna. (a) 3D model of the antenna. (b) Gain pattern for the E-plane (red) and the H-plane (green).

Chapter 6

Conclusions and Outlook

In conclusion, we have demonstrated a novel THz heterodyne detector based on intersubband transitions of a single QW heterostructure. Named as Tunable Antenna-Coupled Intersubband Terahertz (TACIT) mixer, our detector is predicted to be a sensitive THz mixer with wide tunability in the detection frequency (2–5 THz for a 40-nm QW). In Chapter 2, we showed that, based on the HEB mixer theory, our device is predicted to be as sensitive as the current state-of-the-art superconducting HEB mixers, with a SSB mixer noise temperature of $\sim 1,000$ K at much higher operating temperatures of 20– 60 K with a required LO power less than 1μW with a wide IF bandwidth of ~ 10 GHz.

To realize the well-aligned dual-gate structure (enclosing < 1 um QW membrane!) required for TACIT mixers, we developed a flip-chip technique that allow robust dual-side processing of QW membranes. Using the technique, we successfully fabricated and characterized two versions of prototype TACIT mixers.

In our resistively-coupled TACIT mixer integrated with a single-slot antenna, we confirmed the tunability in the detection frequency as well as the THz mixing capability of TACIT mixers at high operating temperature (60 K). The frequency dependence of the heterodyne signal also showed that TACIT mixers can have a wide IF bandwidth of ~ 6

GHz at 60 K. Also, the tunable THz absorption behavior studied in the direct detection mode of TACIT mixers shows good qualitative agreement with the model response we simulated based on the RF impedance model for TACIT mixers.

In our capacitively-coupled TACIT mixer integrated with a modified bow-tie antenna, we found out that new gating scheme was necessary to operate this type of TACIT mixers for proper biasing of the gates. A new gating technique using an analog electronic circuit was developed and verified to work well. We confirmed that the new IF read-out scheme based on the capacitive coupling is effective at reducing the parasitic impedances in the overall IF impedance of TACIT mixers. The frequency dependence of the IF impedance was characterized and demonstrated good agreement with our IF model based on lumped elements. The tunability in detection frequency as well as the THz heterodyne mixing capability were also confirmed in this type of TACIT mixers.

For future work, sensitivity characterization remains our top priority as we didn't measure the mixer noise temperature of TACIT mixers due to unexpectedly large conversion losses observed in both of the prototype devices fabricated for this work. To this end, we plan to further optimize our antenna structure and experiment with different device design as well as different IF read-out mechanism to improve on the conversion efficiency. A further optimized TACIT mixer with improved conversion efficiency and with the SSD mixer noise temperature close to its predicted value of 1,000 K will open up a new, exciting route in developing a sensitive THz mixer operating at high operating temperatures and will be a significant step forward in THz heterodyne instrumentation for planetary applications.

Appendix A

Heterodyne Detection Theory

In this appendix, we briefly review heterodyne detection theory. This appendix follows [19] and [69]. For more information, please refer to these two references.

Theory

The down-conversion process of a mixer is straightforward to understand in terms of simple trigonometry. Consider a mixer with a non-linear current-voltage (IV) characteristics. Then, the IV curve can be expanded with a power series:

$$I(V) = a_0 + a_1 V + a_2 V^2 + a_3 V^3 + \cdots = \sum_{n=0}^{\infty} a_n V^n. \tag{A.1}$$

Now consider a voltage input induced by the electric fields of a local-oscillator (LO) and a signal (RF):

$$V = V_{LO} \sin(\omega_{LO} t) + V_{RF} \sin(\omega_{RF} t) \tag{A.2}$$

where we have $\omega_{LO} = 2\pi f_{LO}$ and $\omega_{RF} = 2\pi f_{RF}$. Now plugging Eq. A.2 into Eq. A.1 and expanding, we get (we only consider up to the V^2 term here)

$$\begin{aligned} V = a_0 + a_1\{V_{LO}\sin(\omega_{LO}t) + V_{RF}\sin(\omega_{RF}t)\}+ \\ a_2\{V_{LO}^2\sin^2(\omega_{LO}t) + V_{RF}^2\sin^2(\omega_{RF}t)\}+ \\ 2a_2V_{LO}V_{RF}\sin(\omega_{LO}t)\sin(\omega_{RF}t) + \cdots . \end{aligned} \tag{A.3}$$

Using the trigonometry identity ($\sin x \sin y = \frac{1}{2}[\cos(x-y) - \cos(x+y)]$), we get

$$\begin{aligned} V = a_0 + a_1\{V_{LO}\sin(\omega_{LO}t) + V_{RF}\sin(\omega_{RF}t)\}+ \\ a_2\{V_{LO}^2\sin^2(\omega_{LO}t) + V_{RF}^2\sin^2(\omega_{RF}t)\}+ \\ a_2V_{LO}V_{RF}\cos{(\omega_{LO}-\omega_{RF})t} - a_2V_{LO}V_{RF}\cos{(\omega_{LO}+\omega_{RF})t} + \cdots \end{aligned} \tag{A.4}$$

where we get the IF response at an angular frequency $|\omega_{LO} - \omega_{RF}|$ or at a frequency $f_{IF} = |f_{LO} - f_{RF}|$. As we can see, the RF signal can be either in the upper sideband (USB) relative to the LO where we have $f_{RF} = f_{LO} + f_{IF}$ or in the lower sideband (LSB) where we have $f_{RF} = f_{LO} - f_{IF}$. Depending on whether the mixer is configured to measure both sidebands or not, the mixer is called a double-sideband (DSB) mixer or a single-sideband (SSB) mixer [26, 27].

Appendix B

Calculation of Intersubband Absorption Frequency

In this appendix, we provide additional information for the calculation of intersubband absorption frequency for TACIT mixers. The calculation is performed with a home-built quantum-well solver that self-consistently solves the Schrödinger equation and Poisson's equation. The solver calculates the absorption frequency for the intersubband transition between the first and the second subbands for a given QW structure at a given charge density, external DC electric field (along the growth direction of the QW), and temperature. In addition, the solver calculates the effective oscillator strength for the transition, which is useful for the evaluation of the device RF impedance based on Mark's impedance model [41]. The solver takes into account the effect of the electrostatic potential from the charge density (self-consistent Hartree potential), many-body effects on the energy of the 2DEG (the exchange and correlation energies), and collective effects (depolarization and exciton shifts) on the absorption frequency.

The solver was originally developed in C++ by Dr. Bryan Galdrikian and modified by Dr. Chris Morris, and later further modified by me to include temperature and electric

field sweeps. For further details on the solver and its hierarchy, refer to Appendices B and C in Dr.Bryan Galdrikian's dissertation [70] and Appendix B in Dr. Chris Morris' dissertation [71].

Simulation Results for a 40-nm QW at 2.3 K

To evaluate the accuracy of the calculation results from our QW solver, we present the calculation results for the intersubband absorption frequency for a 40-nm GaAs/AlGaAs QW at 2.3 K. The intersubband absorption frequency here refers to the absorption frequency for the intersubband absorption between the first and the second subbands in the QW. The temperature of 2.3 K was chosen to match the temperature for the available experimental data (acquired by Dr. Jon Williams [54]). Also, the charge density and the DC electric field values of the data set were used for the calculation.

Figure B.1 shows the experimental data and the calculation results for the intersubband absorption frequency for a 40-nm single GaAs/AlGaAs QW at 2.3 K. For the experimental data (see Figure B.1(a)), the frequency at which peak intersubband absorption occurs is plotted as a function of the difference voltage over different charge densities values extracted from capacitance measurements [54].[1] For the calculation results, the calculated absorption frequency for peak intersubband absorption is plotted as a function of the difference voltage converted from the DC electric field values with the thickness of the QW structure given in [54].

As shown in Figure B.1, the calculation results can reproduce both the qualitative and quantitative features of the experimental data relatively well, with a minor difference for the overall horizontal shift of the experimental over increasing charge density. The calculation results show roughly symmetric parabolic tuning curves about the zero DC

[1]For other experimental details, refer to [54].

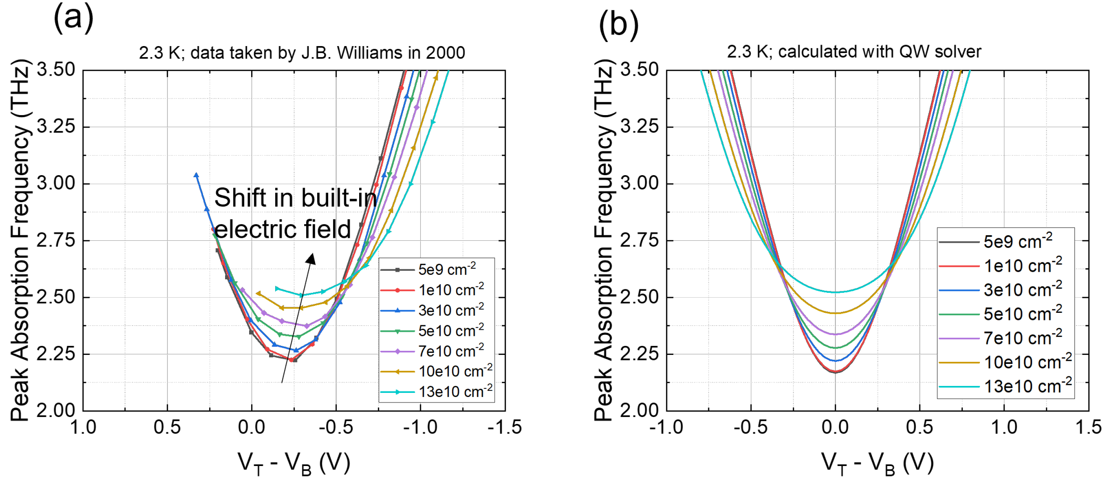

Figure B.1: Peak intersubband absorption frequency as a function of the applied difference voltage from (a) experiments and (b) model at 2.3 K. For the experiments, the built-in electric fields shift with varying charge densities.

electric field, which is the effect of the DC Stark shift on the absorption frequency. Near the zero DC electric field, the absorption frequency increases with increasing charge density due to the depolarization shifts, the effect of which become less important far away from the zero DC electric field at which the subband energy spacing becomes greater. The overall horizontal shifts in the experimental curves are due to the built-in electric fields in real GaAs/AlGaAs quantum wells that also depend on the charge density, and the effect of this is not included in our simulation.

For more quantitative evaluation of the calculation results, we artificially add horizontal shifts to our calculated tuning curves to match the symmetry point in the tuning curves with the experimental curves. Figure B.2 shows the results for each tuning curve with the artificial horizontal shifts. The results show that the calculated absorption frequency show excellent agreement for charge densities above 1.3×10^{11} cm^{-2} and only $\sim$ 5% discrepancies at charge densities less than 1.3×10^{11} cm^{-2}.

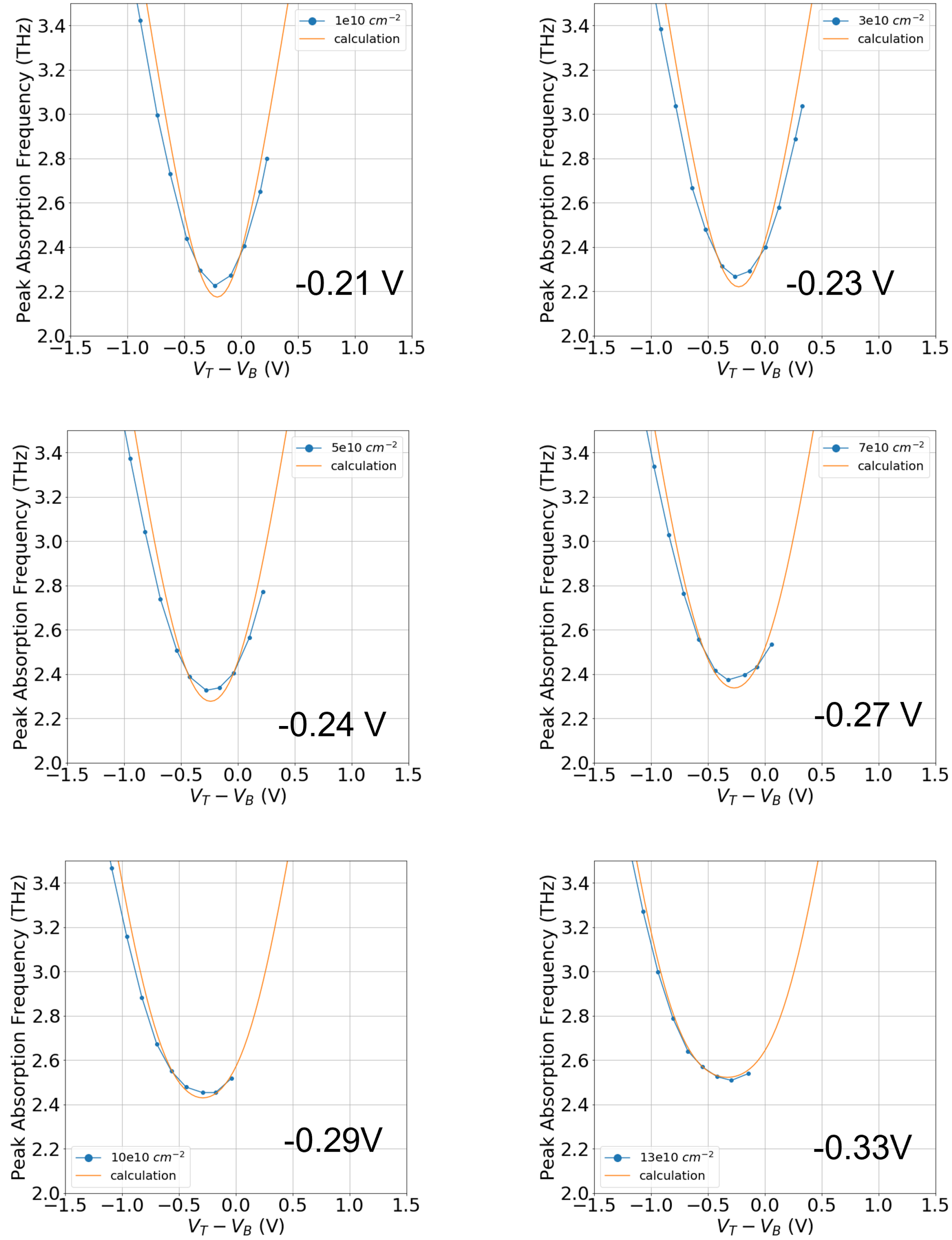

Figure B.2: Comparing the experimental (blue dots with solid line) and the calculated (orange solid line) tuning curves for a 40-nm GaAs QW at 2.3 K. A varying degree of horizontal shifts (indicated as a voltage value on each plot) were applied to the calculation results to account for the different built-in electric fields in the data. The results show good agreement at charge densities above 1.3×10^{11} cm^{-2} and shows $\sim 5\%$ discrepancies at charge densities less than 1.3×10^{11} cm^{-2}.

Appendix C

Indium-Bond-And-Stop-Etch (IBASE) Process Details

In this appendix, I provide a practical step-by-step guide for the Indium-Bond-And-Stop-Etch (IBASE) process used for the fabrication of the TACIT mixers described in this dissertation. As introduced in Chapter 3, the IBASE process is an adaptation of the well-known Epoxy-Bond-And-Stop-Etch (EBASE) technique originally developed for double quantum-well (QW) devices [66]. While both techniques use a flip-chip process in which a QW "die" is flip-chip bonded to a host substrate for the back-side processing for the QW die, an important difference for the IBASE process is the use of indium bonds (instead of vias and subsequent metallization used in the EBASE technique) to establish electrical contacts to the front-side contacts buried in the bonded surfaces of the QW die and the host substrate. Such use of indium as active bonding material offers robust, reliable electrical contacts with a high yield and great flexibility in back-side patterning.

The following recipe was originally conceptualized by a former post-doc Dr. Megnchen Huang and Prof. Mark Sherwin and further developed and optimized by me. While the current recipe is good enough to fabricate working TACIT devices, there are several

steps (e.g. formation of Ohmic contacts and Schottky contacts) that can be improved for better device characteristics (e.g. lower contact resistances, higher gate breakdown voltage, etc) for future TACIT devices.

Finally, the following recipe serves as a practical guide, so I avoided discussing fundamental background for each semiconductor process. However, it is important to have such fundamental knowledge on each process you do, especially in the context of GaAs device processing for successful fabrication of TACIT devices. For such information, I strongly recommend to read through and refer to these two very useful textbooks on the fabrication of GaAs devices [72, 73].

C.1 Front-side Processing

The IBASE process is divided into three phases: front-side processing, flip-chip assembly and underfilling, and back-side processing. Throughout the front-side processing, we define the device mesa and fabricate front-side contacts on the QW die (i.e. two Ohmic contacts for the source and drain and one of the Schottky gate that will be the bottom gate after the flip-chip process).

Back-side Ga Removal, Cleaving, and Cleaning

We first start by preparing the QW wafer for the front-side fabrication. The QW wafer is grown with molecular beam epitaxy (MBE) technique and contains residues of Ga metals on the back side of the wafer as a by-product of the mounting mechanism for the MBE growth. These Ga residues must be removed before we start the processing of the QW sample. We do wet etch with diluted HCl solution to remove the Ga residues. For more details on this chemical process, refer to [72] and [73].

1. Mount a quarter-piece (recommended) or a full QW wafer on a 4” Si carrier wafer with the back side of the QW wafer exposed to the air. First, spin-coat AZ4620 photoresist on the Si carrier wafer at 4,000 rpm for 30 seconds and soft-bake it at 95 °C for 6 minutes. The photoresist here is used as an adhesive. Place the QW sample with the front side facing down (so that the back side with the Ga residues is exposed to air). This way, the front side of the QW wafer is protected throughout the wet etch process. Gently push the QW sample with a tweezer to confirm that the QW sample is mounted firmly on the carrier wafer.

2. Wet etch with diluted hydrochrolic acid (HCl) acid. Prepare HCl solution diluted with de-ionized (DI) water with a mix ratio of HCl:DI = 1:1 in a 1 L beaker. Place a 5 mL beaker (as a place holder) and a stirring bar. Place the Si carrier wafer carrying the QW sample with the back side of the QW sample facing down. Etch for an hour. Set the rpm of the stirring plate to 150 rpm. After an hour, visually inspect if there are still Ga residues on the back side of the QW sample. If there are still some residues left, refresh the HCl solution and etch for additional 30 minutes or an hour.

3. Stop the etch by soaking the carrier wafer in DI water. Rinse with running DI water for 1 minute.

4. Soak the carrier wafer in acetone overnight to dissolve the photoresist. This will detach the QW sample from the carrier wafer. Be careful not to contaminate or scratch the front side of the QW sample while doing this step.

5. Clean the QW wafer following the standard solvent clean recipe (3-min clean with sonication in acetone, followed by 3-min clean with sonication in methanol, and another 3-min clean with sonication in isopropanol).

6. Cleave the QW sample into smaller pieces with desired sizes. Use the blue cleanroom tape to protect the front side while cleaving. Clean the cleaved samples following the standard solvent clean recipe.

Metallization for Alignment Marks

After we prepare the QW sample, we proceed to our first metallization step that defines alignment marks for future photolithography. This step can be skipped but can be useful in testing the recipes for photolithography and metallization especially if the recipes have not been used for a while.

1. Photolithography using either a contact aligner (e.g. Suss MA-6) or a maskless aligner (e.g. Heidelberg MLA150). For the contact aligner, prepare a 3" Si carrier wafer to mount the QW sample. The following recipe is for the contact aligner: spin-coat AZ4210 on the QW sample at 4,000 rpm for 30 s; soft-bake it at 95 °C for 1 minute; mount the QW sample on the Si carrier wafer using the blue cleanroom tape (place the adhesive side of the blue tape facing up and tape on its edges with Kapton tape and place the QW sample); expose with CH2 (intensity $\sim$ 15 mW/cm^2) for 6 seconds; develop with diluted AZ400K developer (AZ400L:DI = 1:4) for 70 seconds. For the maskless aligner, follow the standard recipe provided by the UCSB Nanofab.

2. Inspect the exposed pattern under a microscope. Use green filter to avoid exposing the photoresist.

3. O_2 plasma cleaning (O_2 descum) at 100 W power, 0.3 torr for 30 seconds.

4. Deposit Ti/Au (4 nm/50 nm) using a metal deposition tool (e.g. Ebeam 1 or Ebeam 3 in UCSB nanofab). The thickness of the metal is not very important.

5. Soak the sample in acetone for 10 to 30 minutes and do a lift-off with light sonication.
6. Standard solvent clean with light sonication.
7. Inspect the sample under a microscope.

Mesa Etch

Next, we define the device mesa. After this step, the 2-dimensional electron gas (2DEG) of the QW sample is confined to the device area defined by the mesa.

The following wet etch recipe is based on sulfuric acid (H_2SO_4), but phosphoric acid (H_3PO_4) can be used alternatively, perhaps for better results in terms of reproducibility and uniforminty [73]. Due to poor reproducibility of H_2SO_4-based etchant, it is required to calibrate the etch rate each time before an actual run. Typically, an etch time of ~ 3 mins 40 seconds results in an etch depth of ~ 400 nm, which is a good number to target for the current QW sample structure.

1. Photolithography following the step descrbied in A.1.2. Inspect the exposed pattern under a microscope.
2. O_2 plasma cleaning at 100 W power, 0.3 torr pressure for 30 seconds.
3. Remove the native oxide layer in diluted HCl solution (HCl:DI = 1:20). This step is important to achieve some level of reproducibility.
4. Wet etch a test sample with diluted H_2SO_4 solution (H_2SO_4:H_2O_2:DI = 1:1:60). Etch for 3 minutes and 40 seconds.
5. Rinse with DI water for 1 minute.

6. Clean the test sample with acetone and isopropanol to remove the photoresist. Measure the etch depth using either a confocal microscope (e.g. Olympus LEXT) or a step profiler (e.g. Dektak 6M).

7. If necessary, adjust the etch time to etch roughly 400 nm for the actual run.

8. Inspect the wet etch result under a microscpe and measure the etch depth uisng the confocal microscope. Avoid using the step profiler to prevent the surface damage.

9. Standard solvent clean with light sonication.

Metallization for Ohmic Contacts

This is the metallization step for the Ohmic contacts of TACIT devices and other test devices. In this step, we deposit Ni/AuGe/Ni/Au which is typically used for the Ohmic contacts of the modulation-doped 2DEGs in GaAs/AlGaAs quantum wells[74, 75, 60, 76]. The following recipe can produce Ohmic contacts with a contact resistance of $\sim$ 1 - 2 $\Omega \cdot mm$ at low temperatures (100 K - 2 K). Depending on the thickess of each metal and annealing sequence, the contact resistance can be further decreased by a factor of $\sim$ 10 [76] or even $\sim$ 100 [74, 60]. Also, it is important to know that there is an anisotropy effect on the contact resistance of these Ohmic contacts [75, 76], so orienting the Ohmic contact patterns along the preferred direction is important.

1. Photolithography and O_2 plasma descum. Inspect the exposed pattern under a microscope.

2. Remove the native oxide layer by dipping the QW sample in diluted HCl solution with a mix ratio of HCl:DI = 1:20 for 30 seconds.

3. Use E-beam deposition tool 1 to deposit 4 nm Ni, $\sim$ 440 nm AuGe (use 6 pellets), 105 nm Ni, and finally 100 nm Au. Start the depositoin when the ion guage reading is $\sim$5 - 8 $\times$ 10^{-7} torr.

4. Soak the sample in acetone for an hour and do a lift-off.

5. Solvent cleaning with light sonication.

Rapid Thermal Annealing

Once we deposit the metal sequence for the Ohmic contacts, we rapidly anneal the sample for the deposited metal to form Ohmic contacts with the buried 2DEG. The sample is first heated up to 370 °C and annealed for 1 minute to melt the metal layer. The, the sample is further heated up to 500 °C and annealed for 5 minutes for the melted alloy to penetrate the sample. The quality of the Ohmic contacts heavily depends on the annealing temperature (as well as anneal time), so it's important to make sure that the temperature control is accurate. Do a test run before an actual run to confirm the temperature calibration. If the calibration is off, contact a cleanroom staff and ask for the installation of a new thermocouple and the temperature calibration.

1. Make sure the sample surface is clean. Do solvent clean if necessary.

2. Do a test run of the recipe without the QW sample. Confirm that the thermocouple (TC) reading follows the temperature set point closely. If there is a discrepancy, ask a staff for a new thermocouple and temperature calibration.

3. Run the annealing recipe for the sample. Place the sample close to the thermocouple. Make sure that the thermocouple is contacting the Si carrier wafer. After the run, use a metal tweezer to take out the sample.

4. Inspect the sample under a microscope. After annealing, NiAuGeNiAu Ohmic contacts show their characteristic “burn” marks [72].

Metallization for Bottom Gate and Additional Metal Patterns

After we define the Ohmic contacts, we define one of the Schottky gates along with additional metal patterns (e.g. additional alignment marks, dicing lanes, and, for capacitive TACIT devices, capacitive contacts).

1. Photolithography and O_2 descum. Inspect the pattern under a microscope. The gate metal can be quite small ($\sim 5\ \mu m \times 5\ \mu m$), so make sure that the gate metal pattern is aligned well with the device mesa.

2. Use either Ebeam 1 or Ebeam 3 to deposit 4 nm Ti and 100 nm Au. Native oxide removal doesn’t seem to affect the quality of the Schottky contact here, so the oxide removal step can be skipped.

Device Passivation

After the metallization, we deposit a thin dielectric layer ($\sim$500 nm SiO_2) on the entire front surface of the QW sample to passitvate the devices. It is important to remove the native oxide before the deposition for strong adhesion of the dielectric film to the GaAs surface. Otherwise, the dielectric layer can be peeled off during the dicing step, and it’s very difficult to have good surface quality for the backside processing.

It is recommended to do a test run before doing an actual run, and also to use a dummy piece for the characterization of the film thickness after the deposition.

1. Do a test run. Use a plasma-enhanced chemical vapor deposition tool (e.g. PECVD 1) to deposit $\sim$500 nm SiO_2 on a dummy GaAs or Si piece. Measure the film

thickness using a film thickness measurement tool (e.g. Filmetrics 20).

2. Remove the native oxide by dipping the QW sample in diluted NH_4OH solution (NH_4OH:DI = 1:20) for 30 s.

3. Do the actual run. Adjust the deposition time based on the test run if necessary. Use a new dummy Si piece along with the QW sample to use it as a test sample to measure the thickness after the deposition.

4. Inspect the surface under a microscope.

5. Standard solvent clean with light sonication.

Dry Etch for Dielectric Openings

After the device passivation, the entire front surface of the QW sample is covered with the dielectric layer. To electrically access the Ohmic contacts and the Schottky gate, we need to make openings on the dielectric layer to expose the metal contacts for subsequent metallization in the next step. To do this, we dry-etch the SiO_2 layer with CHF_3 using a plasma etch tool (e.g. ICP1). It is important to calibrate the etch rate before an actual run. Typically, the etch rate is $\sim$ 150 nm/min for the etch recipe that we use.

1. Photolithography and O_2 descum. For spin-coating photoresist, make sure to apply HMDS before applying the phoroesist for better adhesion of the photoresist to the SiO_2 layer of the QW sample.

2. Test run to calibrate the etch rate. Use ICP 1 and the slanted SiO_2 etch recipe (CHF_3 etch with 40 sccm, 5 Pascal, and 900 W/200 W power, etc). Etch a test

sample with SiO_2 layer for 1 min and use a step profiler (e.g. Dektak 6M) to measure the etch depth.

3. Dry etch the QW samples with the etch time calculated based on the film thickness and the measured etch rate.

4. Measure the source-drain resistance of any device at 300 K in a probe station to confirm the etch result. Typically, the source-drain resistance for a Hall device (40 μm $\times$ 400 μm) is $\sim$ 20 - 30 kohm.

5. Solvent clean the QW sample with light sonication.

Metallization for Bottom Gate Electrode

This is the final metallization step for the front side processing where we define electrodes for the gate.

1. Photolithography and O_2 descum. Apply HMDS before spin-coating photoresist.

2. Use either Ebeam 1 or Ebeam 3 deposition tool to deposit 4 nm Ti and 100 nm Au.

3. Lift-off and inspect under a microscope.

4. Solvent clean with light sonication.

Dicing

In this step, the processed QW sample is diced into smaller pieces following the dicing lane defined in step A.1.6. Typically, the "die" has a dimension of $\sim$ 2 mm $\times$ 2 mm and contains a single device.

1. Coat the front side of the QW sample with HMDS and then with photoresist (e.g. AZ4210). Soft-bake it at 90 °C for one minute. This is to protect the front side during the dicing process.

2. Use a dicing saw (e.g. ADT dicing saw) to dice the sample.

3. Solvent clean each die with light sonication.

C.2 Flip-chip Assembly

After the front-side fabrication of the QW dies, we move on to preparing Si substrates and flip-chip bonding of the QW dies on to the prepared Si substrates. These substrates are made of high-resistivity Si to prevent unwanted loss of THz radiation and go through a series of metallization steps that define electrode pattern and indium patches for the flip-chip boning. After the bonding, the gap between the QW die and the Si substrate is filled with underfill epoxy to prevent any damage of the bonded surface throughout the back-side fabrication.

Dicing and Cleaning

First, a high-resistivity Si wafer is diced or cleaved into smaller pieces. For THz applications, it is important to check the thickness and the surface polishing of the wafer to maximize THz radiation going into the device. The required optimal thickness for the Si wafer can be caluclated based on the dimension of a Si lens in use, and doueble-side polished (DSP) wafer is recommended to minimize reflection loss.

1. Use eiather a dicing saw (e.g. ADT dicing saw) or a cleaving tool to dice or cleave the wafer.

2. Solvent clean with light sonication.

Metallizations for Electrode Patterns

After dicing or cleaving the Si wafer into samples of desired sizes, we proceed to a series of metallization steps for electrode patterns that match the terminals already defined on the front side of the QW sample. These patterns also contain bonding pads that will eventually connect to the terminals on the front side of the QW sample. Since there is potentially a signifcant height difference (500 nm) bewteen the two Ohmic contacts and the Schottky gate on the front side of the QW die, it is recommended to do two separate metallizations first for the electrodes that connect to the Ohmic contacts and then the electrode for the Schottky gate to compensate for the height difference.

1. Photolithography and O_2 descum. Apply HMDS before spin-coating photoresist to promote adhesion of the photoresist to the native oxide (SiO_2) of the Si pieces. Inspect the exposed pattern under a microscope.

2. Deposit 4 nm Ti and 100 nm Au using either Ebeam 1 or Ebeam 3 deposition tool. This metallization define the electrodes that connect to the Ohmic contacts on the QW die.

3. Lift-off and solvent clean with light sonication.

4. Repeat the above metallization step to define the electrode for the Schottky contact. Deposit thicker Au based on the measured height difference between the Ohmic contacts and the Schottky contact (typically 400 nm).

Metallization for Indium Patches

After we define the electrode patterns, we proceed to another metallization step for indium patches. The target thickness of the indium is ~ 2 μm.

1. Photolithography and O_2 descum. Apply HMDS before spin-coating photoresist. Inspect the exposed pattern under a microscope.

2. Use a thermal evaporator (e.g. Thermal Evap 2) to deposit ~ 2 μm In. There is more than a factor of two difference in the thickness measured by the crystal monitor of Thermal Evap 2 and the actual thickness. Typically, $\sim$9.6 k$\AA$ on the crystal monitor reading corresponds to an actual thickness of ~ 2.2 μm, which is also likely limited by the thickness of the photoresist (AZ4210) in use.

3. Lift-off and solvent clean with light sonication.

4. Store the Si substrate inside a nitrogen box to prevent the oxidation of indium.

Dicing

In this step, we dice the processed Si sample into smaller substrates (typically 3 μm $\times$ 3 μm).

1. Coat the front side of the Si sample with HMDS and photoresist (e.g. AZ4210). Soft-bake it at 95 °C for 1 minute.

2. Dice the sample.

3. Clean the diced substrates following the standard sovlen clean recipe with light sonication.

Flip-chip Bonding

In this step, we flip-chip bond the QW die to the host Si substrate using indium as solder material. We use a flip-chip bonder (e.g. Fintech flip-chip bonder) to do the bonding. For the bonding, the QW die is first placed with the processed front side facing down and picked up by the pick-up arm of the flip-chip bonder. The Si substate is then placed and alignment is done based on the alignment marks defined on the front side of the QW die and on the Si host substrate using the optical microscope system of the bonding tool. The alignment accuracy can be as good as within $\sum 1\ \mu$m, but there is always some misalignment due to poor resolution of the scope. After the alignment, the QW die is placed on and pushed against the Si substrate while both the die and the substrate are being heated above the melting temperature of indium ($\sim$ 160 °C). The amount of the bonding force and the duration can be adjusted. After the bonding, the bonded sample is quickly cooled down to room temperature.

1. Inspect the front sides of both the QW die and the Si substrate. Clean both the QW die and the Si substrate with light sonication if necessary.

2. Configure the flip-chip bonder. The bonding force arm as well as the x-center should be configured properly to match the size of the QW dies. For a 2 mm x 2 mm die, we use 3 x 3 bonding force arm and 1.5 x 1.5 x-center. Read the manual of the tool or consult a cleanroom staff for further details on how to configure the tool.

3. Pick up the QW die with the bonding force arm. The QW sample should be placed with the front side facing down, so the plate of the tool should be cleaned first to prevent any contamination of the front side.

4. Remove the oxidation layer for the indium patches. Indium oxidizes and we need

to remove the thin oxidation layer for good bonding results. Prepare a 1:40 HCl:DI solution and quickly dip the Si substrate for 1 - 2 seconds and rinse it with DI water.

5. Place the Si host substrate and do the alignment. Follow the alignment procedure of the tool.

6. Run 'Indium TC' recipe for the bonding. In the recipe, the force setting is 3 N,

7. Check the bonding result by measuring the resistances across each pair of contacts in a probe station at room tepmerature.

Underfilling

After the bonding, we fill the gap between the QW die and the Si substrate with underfill epoxy. This is a critical step for good surface quality for the back-side processing. We use EPO-TEK® 353ND for the underfill epoxy. The product has an excellent sealing property, is resistant to the selective etch process during the back-side processing, and transmitting THz well.

1. Prepare the underfill epoxy. The product comes in two parts A and B. Mix A and B by the weight ratio of 10:1. Use a scale to do this. Mix the pot in an aluminum dish and use a wooden stick to slowly stir the pot. Try to avoid any bubbles in the mixed epoxy. Mix the pot for about 5 minutes and wait for another 5 minutes for the bubbles to settle down. At this point, the pot life is $\sim$ 3 hours, so it is recommended to dispense the epoxy within this time frame.

2. Sharpen a wooden tooth pick apply a small amount of the epoxy on a side of the Si substrate. Wait for $\sim$ 2 minutes until the epoxy glob is sucked into the bonded surfaces. Apply more epoxy if necessary.

3. Wait for ∼ 10 minutes for the underfill epoxy to fill the gap. This waiting step is critical to avoid any bubbles trapped in the bonded surfaces.

4. Cure the epoxy by placing the sample on a heating plate at 80 °C for ∼ 1.5 hours. While the recommended curing temperature is as high as 135 °C, the epoxy cured at such high temperatures tends to contain more bubbles that destroy the surface uniformity and also become more prone to surface damages during the backside etch process. The first may be likely due to evaporation of trapped water vapor.

5. Inspect the cured epoxy under a microscope. Gently touch the cured epoxy on the side with a sharpened wooden stick to check the hardness of the cured epoxy. If the epoxy is not cured well, the epoxy may be brittle and can be cracked.

C.3 Backside Processing

After flip-chip bonding and underfilling, we are now ready to process the back side of the QW die. First, we remove the bulk of the back side GaAs by lapping and the remaining GaAs through a series of selective wet etches. At this point, the QW die consists of a very thin (∼ 660 nm) GaAs/AlGaAs membrane that contains a single 40-nm quantum well with mirrorlike finish on the back side. After the wet etch, we remove the underfill epoxy surrounding the GaAs/AlGaAs membrane (now this so-called edge bead is taller than the GaAs/AlGaAs membrane and must be removed for back-side patterning and metallization) and do final patterning and metallizatoin for the back-side processing.

Lapping

We first start by mechanically lapping down the bulk of the back-side GaAs of the QW die. About 450 μm of GaAs should be removed (the QW die is left with $\sim$ 50 μm of GaAs on the back side) for a resonable wet etch time ($\sim$ 3.5 hrs). For the lapping, we use lapping films with three different grit sizes, starting from 30-μm film to remove the first $\sim$ 350 μm, then switching to3-μm film to remove another 100 μm, and finally finishing with a 0.3-μm film to polish the surface. It is important to use films with different grit sizes to avoid damages on the front side of the sample (typically, the grit can penetrate 10 times the grit size). The plishing at the end gives a ince surface finish after the lapping which is good for uniforminity during the following wet etch processes.

1. Configure the lapping tool (Allied bulk mechanical polisher). Follow the tool instruction to do this, but the routine goes something like this: clean all surfaces, install a platen, clean a sample chuck, align the sample chuck relative to the platen.

2. Bond the sample to the sample chuck. Heat the sapmle chuck on a heating plate at 120 °C. Wait for the chuck to heat up. It usually takes about 5 minutes. Apply crystal wax. Flatten the wax using a razor blade. Place the sample at the center of the chuck. Gently push the sample against the sample chuck using wooden q-tips to make the sample sit uniformly on the chuck. Remove the chuck from the heating plate and wait for it to cool down.

3. Remove $\sim$ 350 μm using an Al_2O_3 film with a 30-μm grit. First lap $\sim$ 100 μm and measure the remaining thickness to check if there is any offset. Continue lapping down to $\sim$ 350 μm.

4. Switch to 3-μm grit film (pink) and continue lappng another 100 um.

5. Finish with a 0.3-μm grit film (white). Lap about $\sim$ 10 μm.

6. Check the surface for any visible surface damage. The surface should look polished to naked eyes.

7. Inspect the polished surface and measure the thickness of the remaining GaAs on the backside using a confocal microscope. Typically the measured thickness of the remaining GaAs is $\sim 50\ \mu$m.

Selective Wet Etches

After we mechanically remove the bulk of GaAs on the back side, we do a series of selective wet etches to remove the remaining ($\sim$ 50 μm) GaAs and the 500-μm $Al_{0.74}Ga_{0.26}As$ layer on the back side. First, we remove the remaining GaAs using citric acid that has very high selectivity against the etch stop layer ($\sim$ 500-μm $Al_{0.74}Ga_{26}As$ layer). After we remove the GaAs, we do the second selective wet etch using diluted HF to remove the etch stop layer. The diluted HF solution has good selectivity against GaAs, so the 10-nm GaAs cap works as the etch stop layer for the second selective etch. After the wet etch, the cured epoxy surrounding the GaAs/AlGaAs membrane is now taller than the back side of the membrane and must be removed for good patterning results.

1. Inspect the surface quality of the back side. Rinse with solvent if there is any wax or GaAs residue on the back side. Also, look for any sign of surface damage (e.g. cracks) during the lapping process.

2. Bond the sample to a glass slide using crystal wax.

3. Remove the native oxide of GaAs on the back side by soaking the sample in diluted NH_4OH solution (NH_4OH:DI = 1:20) for 1 minute.

4. Prepare citric acid solution. Mix premix citric acid solution (50 to 50 with water by weight) with $H_{s2}O_2$ (premix $C_6H_8O_7$:H_2O_2 = 6.5:1). Place a stirring bar. Stir at 300 rpm. Etch for roughly 3.5 hours. Inspect the surface by eye. If the front-side contacts are visible with clean, mirror-like surface quality, then the etch is done.

5. Prepare diluted HF solution for the second selective etch. Mix 49% HF with DI water (HF:DI = 1:4). We're removing the 500-nm $Al_{0.74}Ga_{26}As$ layer here, so the etch time is relatively short. Dip the sample for $\sim$ 10 seconds. Rinse with DI water for 1 minute. Do a second dip for $\sim$ 7 seconds and rinse with DI water for 2 minutes.

6. Inspect the surface and blow dry with N_2.

7. Remove the sample from the glass slide and rinse the sample with acetone followed by isopropanol.

8. Peel off the underfill epoxy surrounding the QW die under a microscope using a razor blade. If the epoxy was properly cured, peeling off should be very easy.

Metallization for Top Gate Pattern

This is the final step of the IBASE process where you define the top gate metal pattern on the sample. The steps generally follow the previous patterning and metallization steps but working with a smaller sample requires some adjustments. For example, with the smaller sample size, spin-coating photoresist with good uniformity becomes harder (edge bead problem). This edge bead problem can be partially solved by placing dummy Si substrate pieces around the sample when spin-coating.

1. Solvent clean. I tend to avoid sonication at this point to avoid any damage on the GaAs/AlGaAs membrane and stick with plain solvent rinsing to clean the sample.

2. Photolithography and O_2 descum. Place Si substrates with similar thickness around the sample to mitigate the edge bead problem when spin-coating.

3. Deposit 4 nm Ti and 100 nm Au using either Ebeam 1 or Ebeam 3 deposition tool.

4. Lift-off after $\sim$ 1 hr of acetone soak. Avoid using sonication.

Appendix D

Finite-Element Method (FEM) Simulation Results

In this appendix, we present finite-element method (FEM) simulation results for the antenna structures used for the prototype TACIT mixers described in this work. These include a single-slot antenna for a resistively-coupled TACIT mixer and a modified bow-tie antenna for a capacitively-coupled TACIT mixer.

FEM Simulation

In simulating the antenna structures, we use ANSYS High Frequency Structure Simulator (HFSS). The software allows for the 3D modelling of electromagnetic (EM) structures and for the EM simulation of the structures by adaptively meshing the structures in tetrahedral finite elements and solving the Maxwell's equations in a given finite element with a given solution setup, port setting, and boundary setting. For the simulation antenna structures, we use modal solution setup and lumped port setting, in which the provided electromagnetic structures are excited with a single mode at a given frequency

with a known power.

3D Model, Material, and Boundary Setting

Accurate 3D models of EM structures with correct material and boundary setting are important for accurate modeling results in ANSYS HFSS. For our antenna structures placed on Si substrates, we enclose the structures with two material boxes—the top vacuum box and the bottom Si box. The external faces of these boxes are set to radiation boundaries such that the EM radiation propagates infinitely without getting reflected from the faces. Also, with the same reason, the global material (the material outside the boxes) is set to Si to minimize the surface reflections for a more accurate far field patterns on the Si side. The faces of these boxes are placed at least a quarter wavelength away from the EM structures as recommended by the software.

Port Setting

To feed the antenna structures, a lumped port is used in our simulation. The port impedance is set to 50 Ω and the integration line is defined as a line connecting the top and the bottom gates. For the case of the single-slot antenna, a vertical integration line is introduced. For the case of the bow-tie antenna, an integration line is defined on the same plane with the top and the bottom gates. Note that for the vertical port excitation for the single-slot antenna, the impedance calculated from the simulation includes the effect of the geometric capacitance due to the overlap of the metal extensions for the top and the bottom gates. This geometric capacitance is already included in the device RF impedance in our RF model. As a result, for more accurate antenna impedance, we must de-couple the effect of the geometric capacitance from the simulation results.

Results for Single-slot Antenna

3D Model

Figure D.1 shows the 3D model for the single-slot antenna. As we mentioned earlier, the antenna structure is placed in-between the vacuum box and the Si box with the external faces set as radiation boundary. The global material is set to Si. Figure D.1(b) shows the antenna structure as well as the port setup for the model, with the inset showing the vertical integration line for the feed. The material for the antenna metals was set to gold.

S11 and Antenna Impedance

Figure D.2 shows the calculated S11 and the antenna impedance for the slot antenna. The antenna impedance here includes the effect of the geometric capacitance, which can be de-coupled when calculating the antenna impedance of the antenna itself. Figure D.2 shows that the slot antenna is resonant at 1.93 THz, which is quite far off from 2.52 THz and 3.11 THz where we performed the THz measurements for the resistively-coupled TACIT mixers. Because of this, the antenna impedance is rather small at 2.52 THz and 3.11 THz.

Gain Pattern

Figure D.3 shows the gain (radiation) pattern for the single-slot antenna. Figure D.3(a) shows the 3D gain pattern overlaid with the 3D model and figure D.3(b) shows the gain for the E-plane and the H-plane of the antenna in linear scale. As shown in the figure, the radiation efficiency is rather poor for the single-slot antenna.

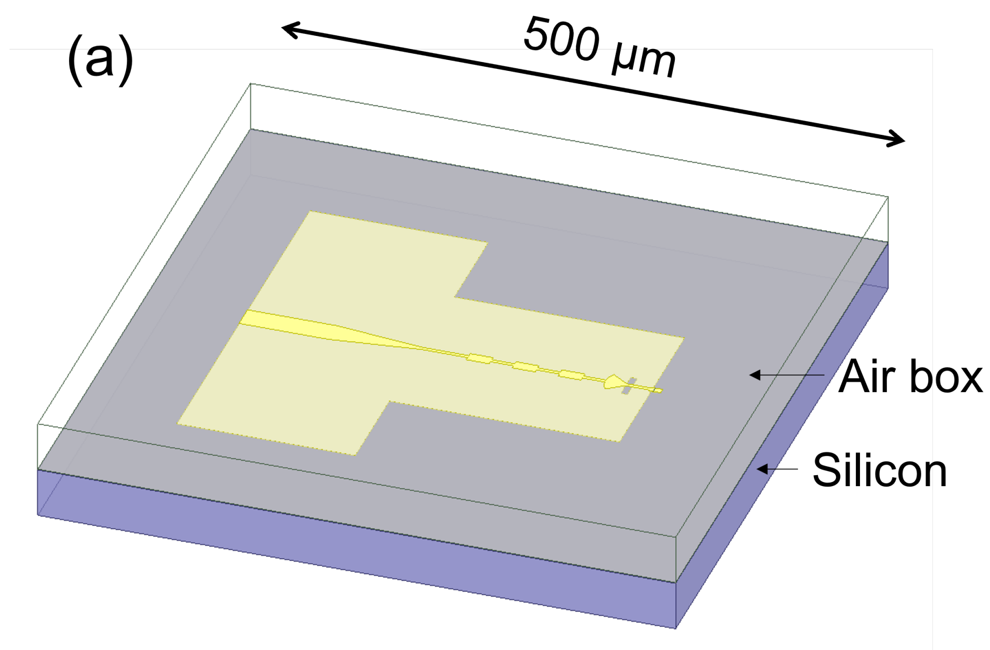

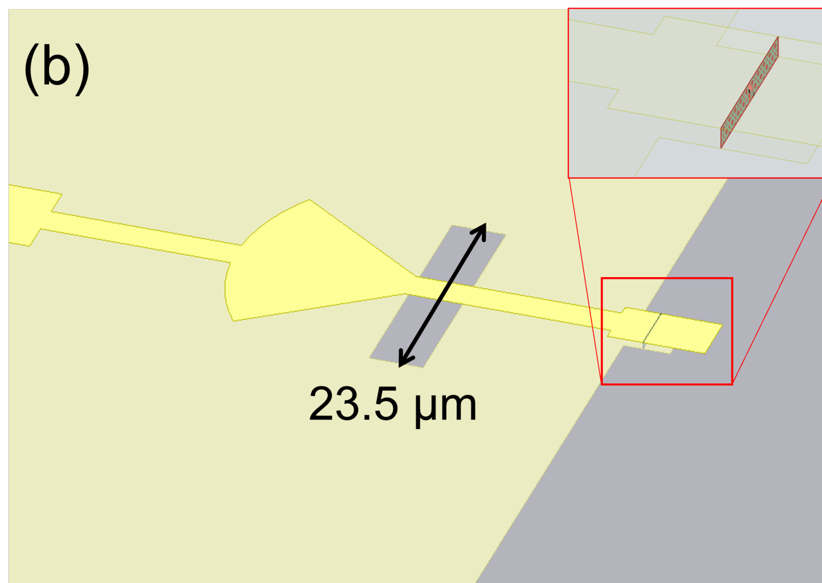

Figure D.1: 3D model for the single-slot antenna. (a) Full 3D model. (b) Model near the active region.

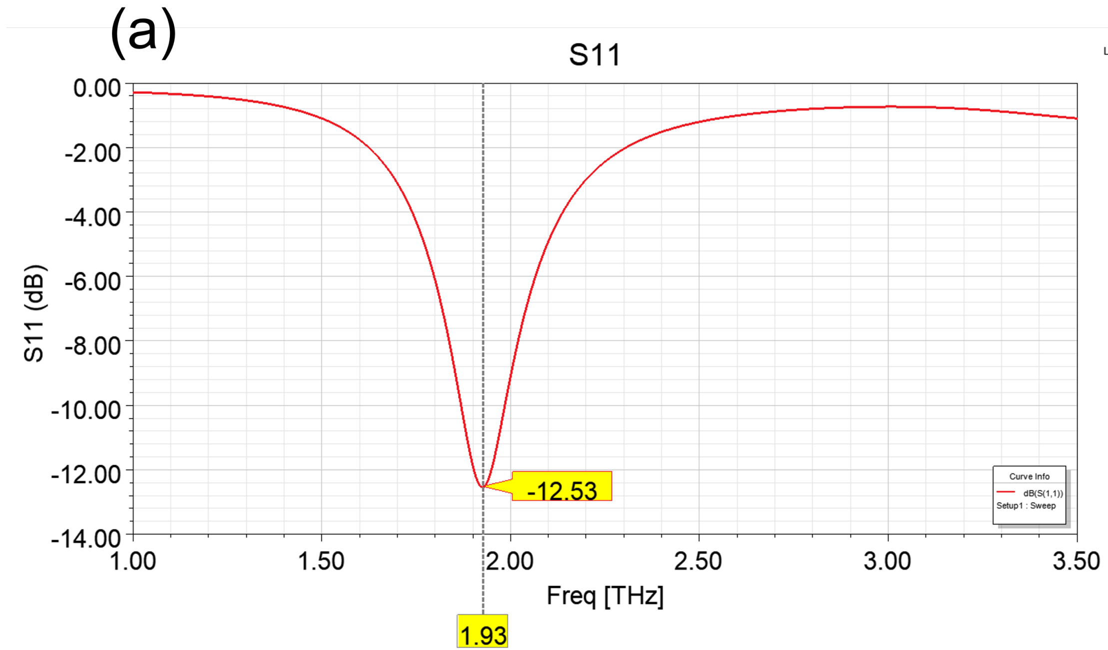

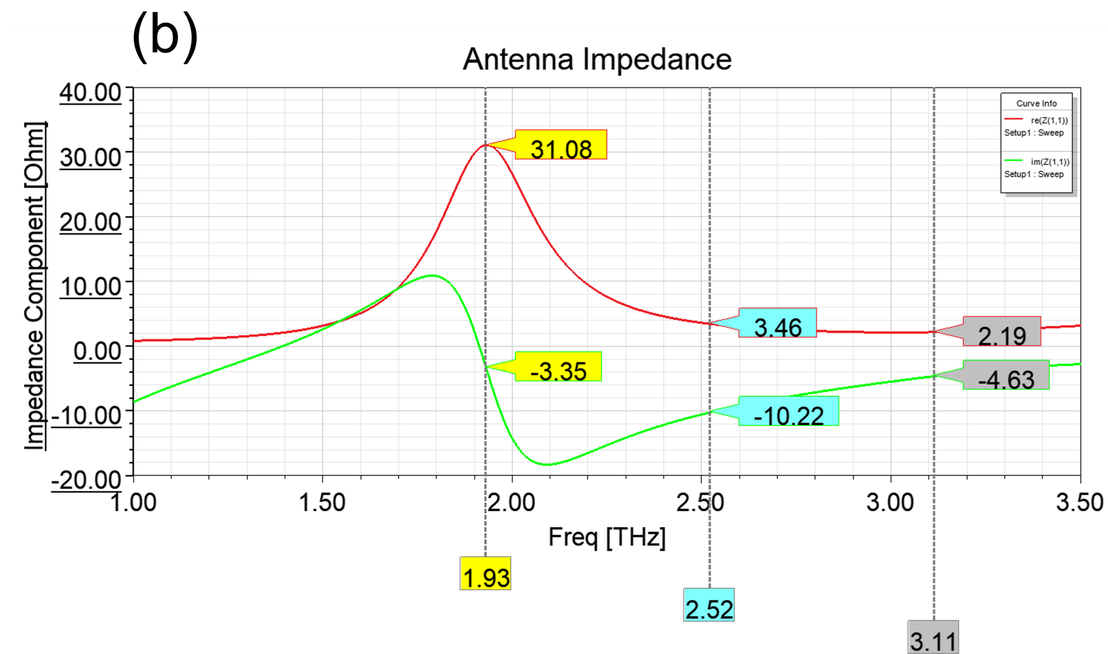

Figure D.2: S11 and antenna impedance for the single-slot antenna. (a) S11. (b) Antenna impedance.

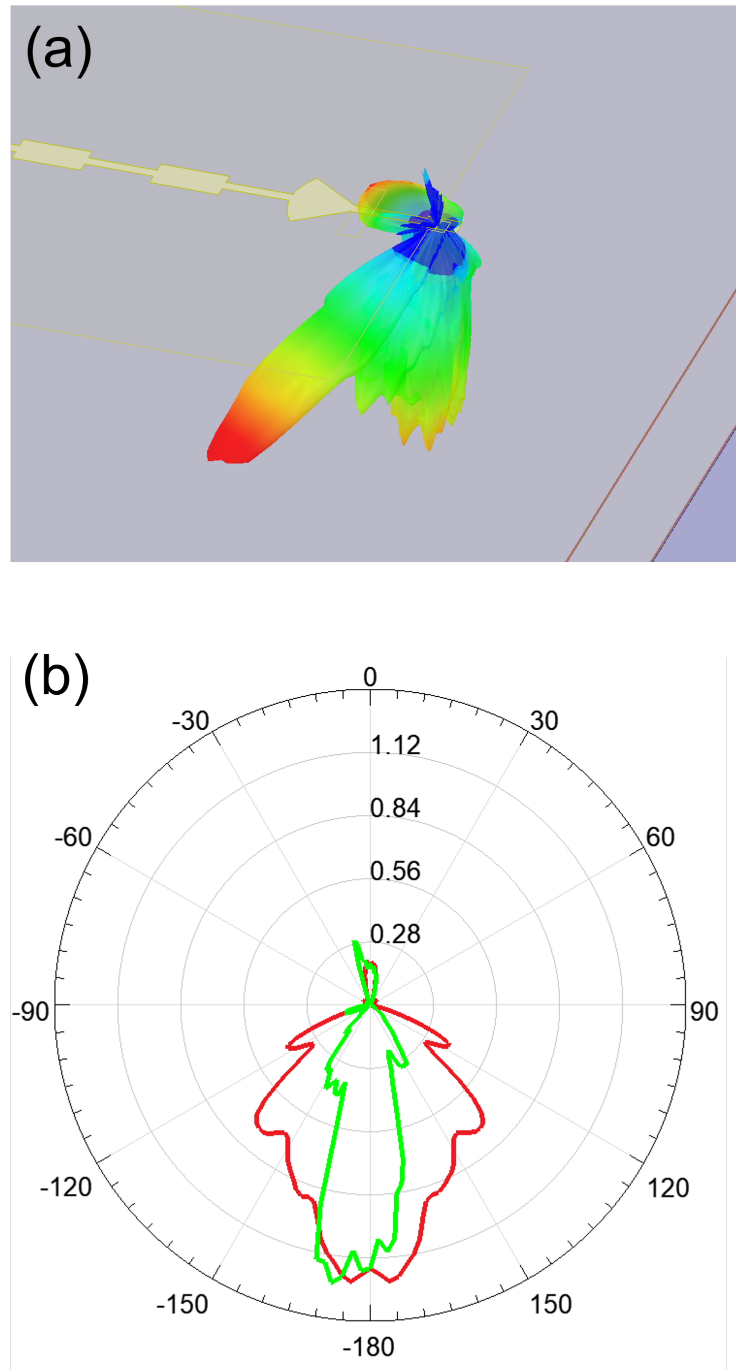

Figure D.3: Gain patterns for the single-slot antenna. (a) 3D gain pattern. (b) Gain pattern for the E-plane (green) and for the H-plane (red).

Bow-tie Antenna

3D Model

Figure D.4 shows the 3D model for the bow-tie antenna. The antenna structure is placed in-between the vacuum box and the Si box with the external faces set as radiation boundary. The global material is set to Si. Figure D.4(b) shows the antenna structure near the active region as well as the port setup for the model, with the inset showing the planar integration line for the feed. The material for the antenna metals was set to gold.

S11 and Antenna Impedance

Figure D.5 shows the calculated S11 and the antenna impedance for the bow-tie antenna. Both the simulated S11 and the antenna impedance imply the broadband operation of the bow-tie antenna. The real part of the antenna impedance ($\mathbb{R}_{ant}$ is consistent with a typical value of a broadband THz antenna on Si substrate.

Gain Pattern

Figure D.6 shows the gain (radiation) pattern for the bow-tie antenna. Figure D.6(a) shows the 3D gain pattern overlaid with the 3D model and figure D.6(b) shows the gain for the E-plane and the H-plane of the antenna in linear scale. As shown in the figure, while the radiation efficiency for the bow-tie antenna seems to be a lot better than that for the single-slot antenna, the gain pattern is highly directive, with most of the radiation (> 80 %) radiating outside the 120° angle from the center on the Si side. Since only the radiation within this angle can be coupled out efficiently with Si lenses in our quasi-optical coupling scheme, we expect that the final radiation effciency for the bow-tie antenna is also rather poor.

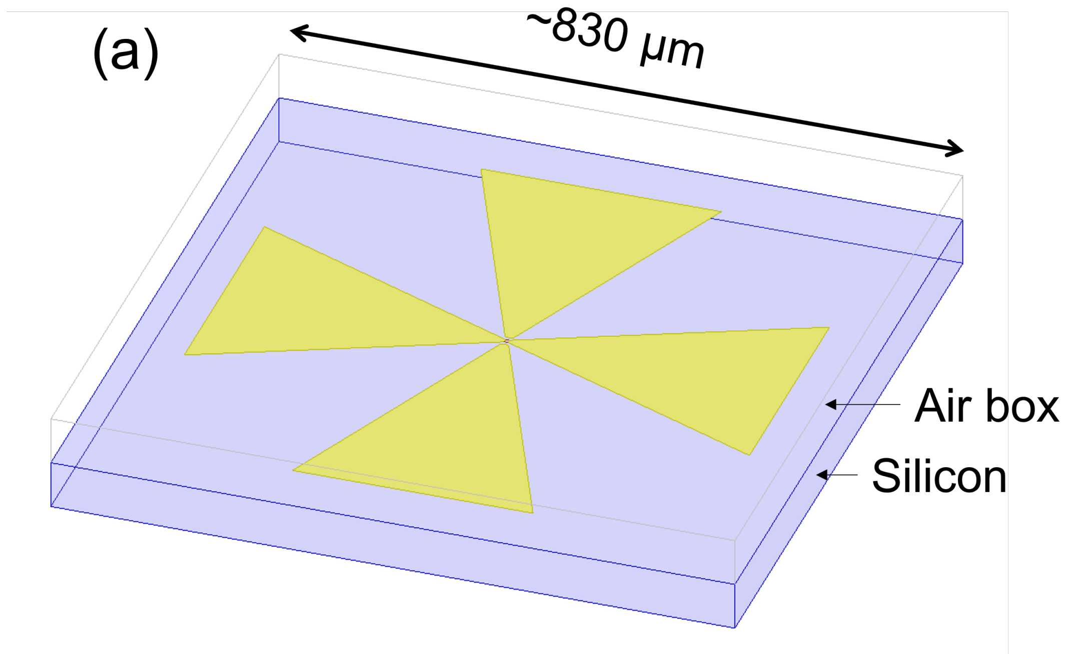

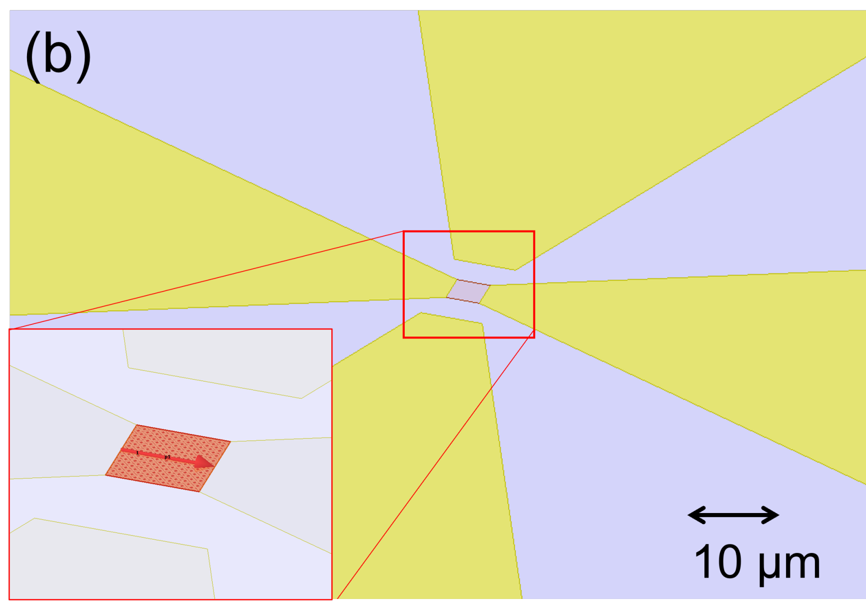

Figure D.4: 3D model for the bow-tie antenna. (a) Full 3D model. (b) Model near the active region.

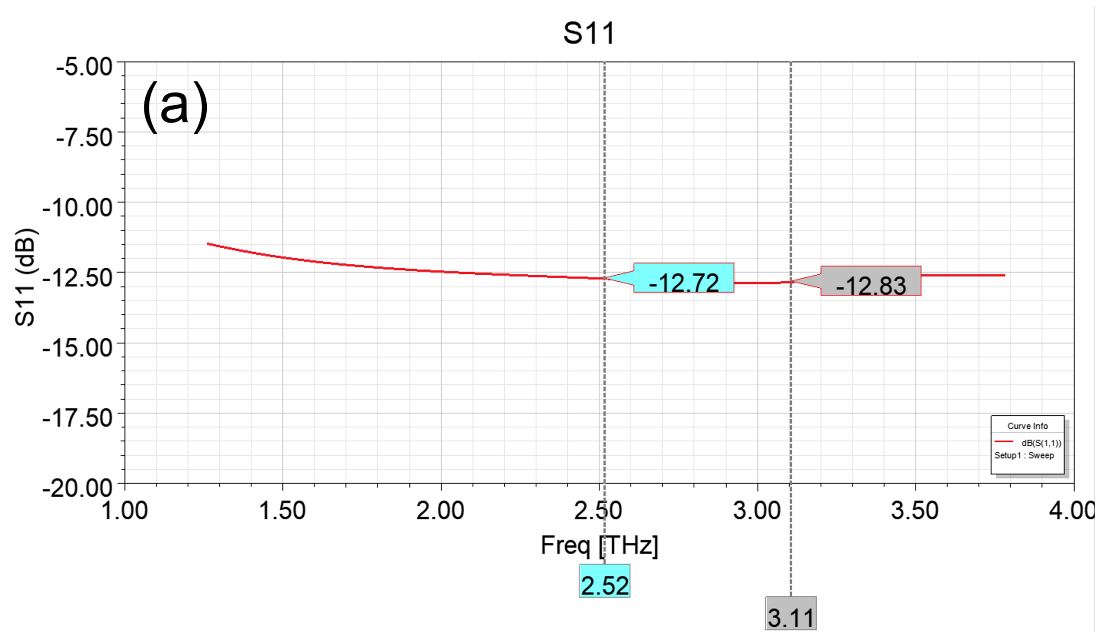

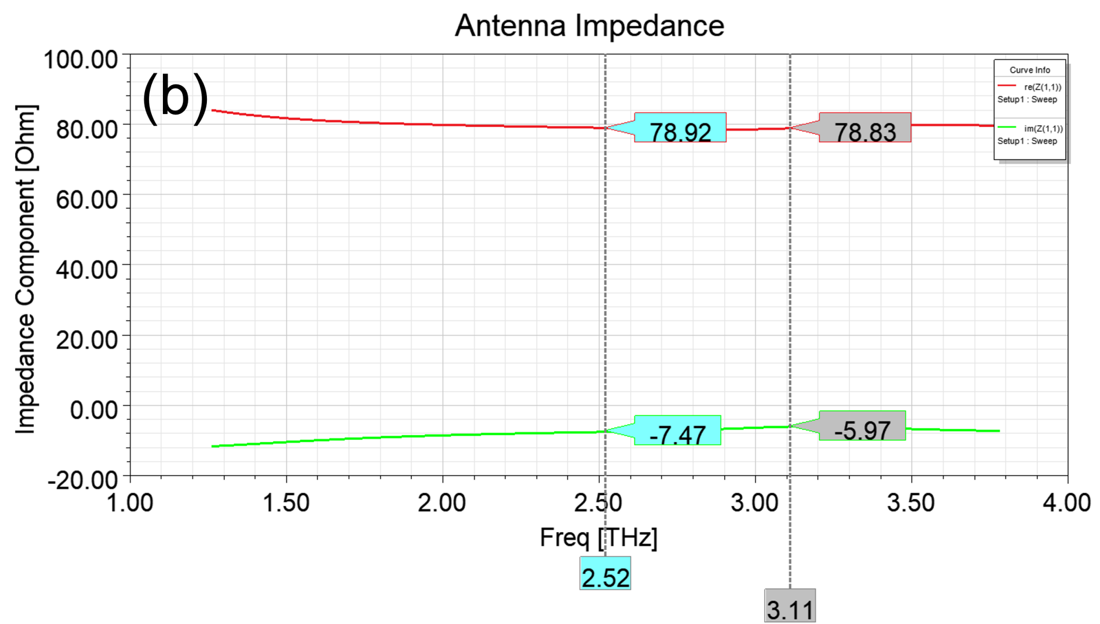

Figure D.5: S11 and antenna impedance for the bow-tie antenna. (a) S11. (b) Antenna impedance.

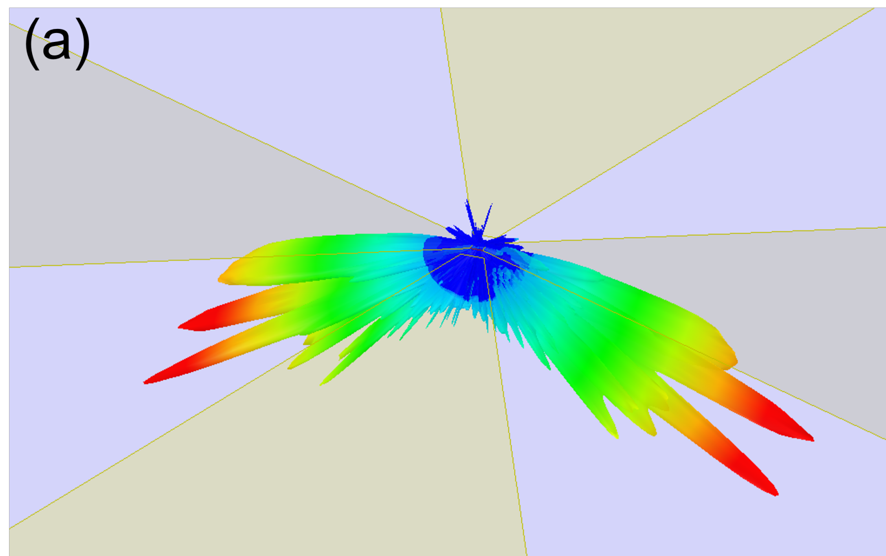

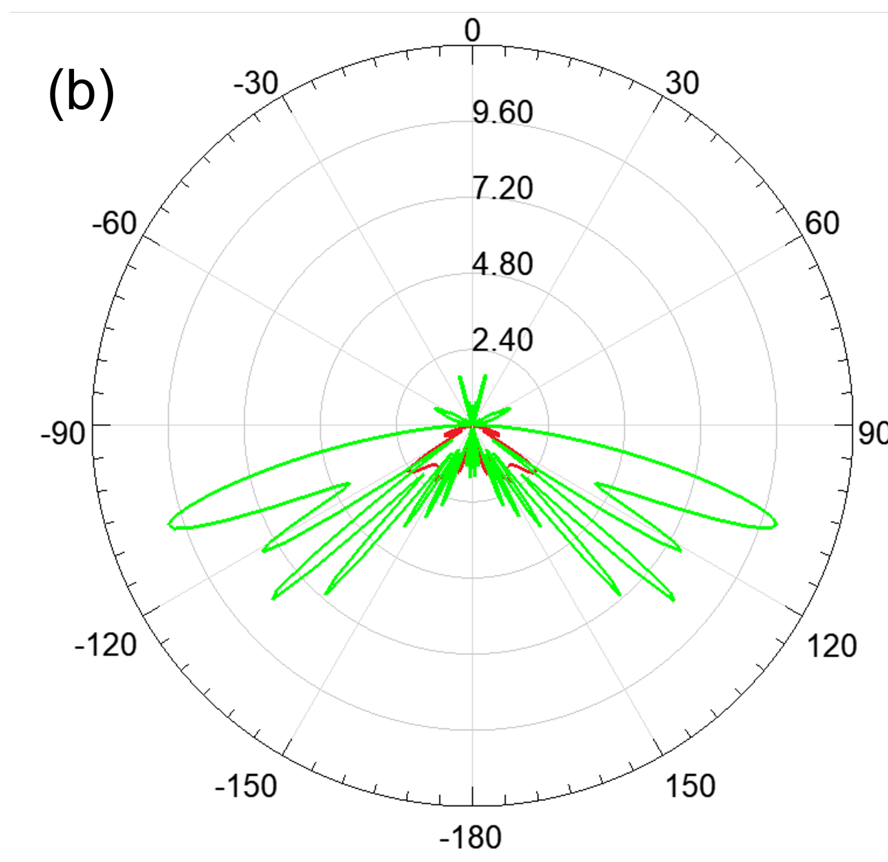

Figure D.6: Gain patterns for the bow-tie antenna. (a) 3D gain pattern. (b) Gain pattern for the E-plane (green) and for the H-plane (red).

Bibliography

[1] H. P. Röser, "Heterodyne spectroscopy for submillimeter and far-infrared wavelengths from 100 μm to 500 μm," *Infrared Physics*, vol. 32, no. C, pp. 385–407, 1991.

[2] J. W. Waters, "Submillimeter-Wavelength Heterodyne Spectroscopy and Remote Sensing of the Upper Atmosphere," *Proceedings of the IEEE*, vol. 80, no. 11, pp. 1679–1701, 1992.

[3] F. C. De Lucia, "The submillimeter: A spectroscopist's view," *Journal of Molecular Spectroscopy*, vol. 261, no. 1, pp. 1–17, 2010.

[4] T. G. Phillips and J. Keene, "Submillimeter Astronomy," *Proceedings of the IEEE*, vol. 80, no. 11, 1992.

[5] P. Siegel, "Terahertz technology," *IEEE Transactions on Microwave Theory and Techniques*, vol. 50, no. 3, pp. 910–928, 2002.

[6] P. H. Siegel, "THz instruments for space," *IEEE Transactions on Antennas and Propagation*, vol. 55, no. 11 I, pp. 2957–2965, 2007.

[7] C. Kulesa, "Terahertz spectroscopy for astronomy: From comets to cosmology," *IEEE Transactions on Terahertz Science and Technology*, vol. 1, no. 1, pp. 232–240, 2011.

[8] D. Farrah, K. E. Smith, D. Ardila, C. M. Bradford, M. Dipirro, C. Ferkinhoff, J. Glenn, P. Goldsmith, D. Leisawitz, T. Nikola, N. Rangwala, S. A. Rinehart, J. Staguhn, M. Zemcov, J. Zmuidzinas, and J. Bartlett, "Review: far-infrared instrumentation and technological development for the next decade," *Journal of Astronomical Telescopes, Instruments, and Systems*, vol. 5, no. 02, p. 1, 2019.

[9] M. Tonouchi, "Cutting-edge terahertz technology," *Nature Photonics*, vol. 1, pp. 97–105, 2007.

[10] S. S. Dhillon, M. S. Vitiello, E. H. Linfield, A. G. Davies, M. C. Hoffmann, J. Booske, C. Paoloni, M. Gensch, P. Weightman, G. P. Williams, E. Castro-Camus, D. R.

Cumming, F. Simoens, I. Escorcia-Carranza, J. Grant, S. Lucyszyn, M. Kuwata-Gonokami, K. Konishi, M. Koch, C. A. Schmuttenmaer, T. L. Cocker, R. Huber, A. G. Markelz, Z. D. Taylor, V. P. Wallace, J. Axel Zeitler, J. Sibik, T. M. Korter, B. Ellison, S. Rea, P. Goldsmith, K. B. Cooper, R. Appleby, D. Pardo, P. G. Huggard, V. Krozer, H. Shams, M. Fice, C. Renaud, A. Seeds, A. Stöhr, M. Naftaly, N. Ridler, R. Clarke, J. E. Cunningham, and M. B. Johnston, "The 2017 terahertz science and technology roadmap," *Journal of Physics D: Applied Physics*, vol. 50, no. 4, 2017.

[11] D. M. Mittleman, "Perspective: Terahertz science and technology," *Journal of Applied Physics*, vol. 122, no. 23, 2017.

[12] J. Neu and C. A. Schmuttenmaer, "Tutorial: An introduction to terahertz time domain spectroscopy (THz-TDS)," *Journal of Applied Physics*, vol. 124, no. 23, 2018.

[13] P. H. Siegel, "Terahertz technology in biology and medicine," *IEEE Transactions on Microwave Theory and Techniques*, vol. 52, no. 10, pp. 2438–2447, 2004.

[14] Q. Sun, Y. He, K. Liu, S. Fan, E. P. Parrott, and E. Pickwell-MacPherson, "Recent advances in terahertz technology for biomedical applications," *Quantitative Imaging in Medicine and Surgery*, vol. 7, no. 3, pp. 345–355, 2017.

[15] J. Federici and L. Moeller, "Review of terahertz and subterahertz wireless communications," *Journal of Applied Physics*, vol. 107, no. 11, 2010.

[16] H. J. Song and T. Nagatsuma, "Present and future of terahertz communications," *IEEE Transactions on Terahertz Science and Technology*, vol. 1, no. 1, pp. 256–263, 2011.

[17] H.-J. Song and N. Lee, "Terahertz Communications: Challenges in the Next Decade," *IEEE Transactions on Terahertz Science and Technology*, vol. 1, pp. 1–1, 2021.

[18] F. C. De Lucia, "Science and Technology in the Submillimeter Region," *Optics and Photonics News*, vol. 14, no. 8, p. 44, 2003.

[19] E. Bründermann, H. W. Hübers, and M. F. G. Kimmitt, *Terahertz techniques*, vol. 151. 2012.

[20] C. Walker, C. Kulesa, P. Bernasconi, H. Eaton, N. Rolander, C. Groppi, J. Kloosterman, T. Cottam, D. Lesser, C. Martin, A. Stark, D. Neufeld, C. Lisse, D. Hollenbach, J. Kawamura, P. Goldsmith, W. Langer, H. Yorke, J. Sterne, A. Skalare, I. Mehdi, S. Weinreb, J. Kooi, J. Stutzki, U. Graf, M. Brasse, C. Honingh, R. Simon, M. Akyilmaz, P. Puetz, and M. Wolfire, "The Stratospheric THz Observatory (STO),"

Ground-based and Airborne Telescopes III, vol. 7733, no. July 2010, p. 77330N, 2010.

[21] P. Temi, P. M. Marcum, E. Young, J. D. Adams, S. Adams, B. G. Andersson, E. E. Becklin, A. Boogert, R. Brewster, E. Burgh, B. R. Cobleigh, S. Culp, J. De Buizer, E. W. Dunham, C. Engfer, G. Ediss, M. Fujieh, R. Grashuis, M. Gross, E. Harmon, A. Helton, D. Hoffman, J. Homan, M. Hütwohl, H. Jakob, S. C. Jensen, C. Kaminski, D. Kozarsky, A. Krabbe, R. Klein, Y. Lammen, U. Lampater, W. B. Latter, J. Le, N. McKown, R. Melchiorri, A. W. Meyer, J. Miles, W. E. Miller, S. Miller, E. Moore, D. J. Nickison, K. Opshaug, E. Pfüeller, J. Radomski, J. Rasmussen, W. Reach, A. Reinacher, T. L. Roellig, G. Sandell, R. Sankrit, M. L. Savage, S. Shenoy, J. E. Schonfeld, R. Y. Shuping, E. C. Smith, E. Talebi, S. Teufel, T. C. Tseng, W. D. Vacca, J. Vaillancourt, J. E. Van Cleve, M. Wiedemann, J. Wolf, E. Zavala, O. Zeile, P. T. Zell, and H. Zinnecker, "The sofia observatory at the start of routine science operations: Mission capabilities and performance," *Astrophysical Journal, Supplement Series*, vol. 212, no. 2, 2014.

[22] G. L. Pilbratt, J. R. Riedinger, T. Passvogel, G. Crone, D. Doyle, U. Gageur, A. M. Heras, C. Jewell, L. Metcalfe, S. Ott, and M. Schmidt, "Herschel Space Observatory," *Astronomy and Astrophysics*, vol. 518, no. 7-8, 2010.

[23] S. Gulkis, M. Frerking, J. Crovisier, G. Beaudin, P. Hartogh, P. Encrenaz, T. Koch, C. Kahn, Y. Salinas, R. Nowicki, R. Irigoyen, M. Janssen, P. Stek, M. Hofstadter, M. Allen, C. Backus, L. Kamp, C. Jarchow, E. Steinmetz, A. Deschamps, J. Krieg, M. Gheudin, D. Bockelée-Morvan, N. Biver, T. Encrenaz, D. Despois, W. Ip, E. Lellouch, I. Mann, D. Muhleman, H. Rauer, P. Schloerb, and T. Spilker, "MIRO: Microwave Instrument for Rosetta Orbiter," *Space Science Reviews*, vol. 128, no. 1, pp. 561–597, 2007.

[24] P. F. Goldsmith, "Sub-millimeter heterodyne focal-plane arrays for high-resolution astronomical spectroscopy," *URSI Radio Science Bulletin*, no. 362, pp. 53–73, 2017.

[25] E. Bründermann, H. W. Hübers, and M. F. G. Kimmitt, *Terahertz techniques*, vol. 151, ch. 6, pp. 293–300. 2012.

[26] E. Bründermann, H. W. Hübers, and M. F. G. Kimmitt, *Terahertz techniques*, vol. 151, ch. 5.5, pp. 221–245. 2012.

[27] C. K. Walker, *Terahertz Astronomy*, ch. 6, pp. 159–230. 2015.

[28] T. G. Phillips and K. B. Jefferts, "A low temperature bolometer heterodyne receiver for millimeter wave astronomy," *Review of Scientific Instruments*, vol. 44, no. 8, pp. 1009–1014, 1973.

[29] H. W. Hübers, "Terahertz heterodyne receivers," *IEEE Journal on Selected Topics in Quantum Electronics*, vol. 14, no. 2, pp. 378–391, 2008.

[30] S. M. Smith, N. J. Cronin, R. J. Nicholas, M. A. Brummell, J. J. Harris, and C. T. Foxon, “Millimeter and submillimeter detection using Ga1-xAlxAs/GaAs heterostructures,” *International Journal of Infrared and Millimeter Waves*, vol. 8, no. 8, pp. 793–802, 1987.

[31] J. X. Yang, W. Grammer, F. Agahi, K. M. Kau, and K. S. Yngvesson, “Two-dimensional electron gas hot-electron mixers for millimeter waves and submillimeter waves,” in *Second International Symposium on Space Terahertz Technology*, p. 70, 1991.

[32] K. S. Yngvesson, “Ultrafast two-dimensional electron gas detector and mixer for terahertz radiation,” *Applied Physics Letters*, vol. 76, no. 6, pp. 777–779, 2000.

[33] J. Shah, “Hot Carriers in Quasi-2-D Polar Semiconductors,” *IEEE Journal of Quantum Electronics*, vol. 22, no. 9, pp. 1728–1743, 1986.

[34] J. X. Yang, F. Agahi, D. Dai, C. F. Musante, W. Grammer, K. M. Lau, and K. S. Yngvesson, “Wide-Bandwidth Electron Bolometric Mixers: A 2DEG Prototype and Potential for Low-Noise THz Receivers,” *IEEE Transactions on Microwave Theory and Techniques*, vol. 41, no. 4, pp. 581–589, 1993.

[35] M. Lee, L. N. Pfeiffer, K. W. West, and K. W. Baldwin, “Wide bandwidth millimeter wave mixer using a diffusion cooled two-dimensional electron gas,” *Applied Physics Letters*, vol. 78, no. 19, pp. 2888–2890, 2001.

[36] M. Lee, L. N. Pfeiffer, and K. W. West, “Ballistic cooling in a wideband two-dimensional electron gas bolometric mixer,” *Applied Physics Letters*, vol. 81, no. 7, pp. 1243–1245, 2002.

[37] P. J. Burke, I. B. Spielman, J. P. Eisenstein, L. N. Pfeiffer, and K. W. West, “High frequency conductivity of the high-mobility two-dimensional electron gas,” *Applied Physics Letters*, vol. 76, pp. 745–747, feb 2000.

[38] J. N. Heyman, K. Unterrainer, K. Craig, B. Galdrikian, M. S. Sherwin, K. Campman, P. F. Hopkins, and A. C. Gossard, “Temperature and intensity dependence of intersubband relaxation rates from photovoltage and absorption,” *Phys. Rev. Lett.*, vol. 74, pp. 2682–2685, Apr 1995.

[39] M. Helm, “Chapter 1 The Basic Physics of Intersubband Transitions,” *Semiconductors and Semimetals*, vol. 62, pp. 1–99, jan 1999.

[40] H. H. Schneider, *Quantum well infrared photodetectors : physics and applications / H. Schneider, H.C. Liu.* Springer series in optical sciences, 126, Berlin ;: Springer, 2007.

[41] M. S. Sherwin, C. Cates, B. Serapiglia, Y. Dora, J. B. Williams, K. D. Maranowski, A. C. Gossard, and W. R. McGrath, "Tunable Antenna-Coupled Intersubband Terahertz (TACIT) Mixers: the Quantum Limit Without the Quantum Liquid," in *Proceedings of Far-IR, Submm, and mm Detector Technology Worskhop*, (Monterey, CA), 2002.

[42] C. L. Cates, G. Briceno, M. S. Sherwin, K. D. Maranowski, K. Campman, and A. C. Gossard, "A concept for a tunable antenna-coupled intersubband terahertz (TACIT) detector," *Physica E*, vol. 2, no. 1-4, pp. 463–467, 1998.

[43] M. S. Sherwin, "Tunable antenna-coupled intersubband terahertz (TACIT) detector," U.S. Patent 5914497, Jun. 22, 1999.

[44] C. Cates, J. B. Williams, M. S. Sherwin, K. D. Maranowski, and A. C. Gossard, "Quantum well based tunable antenna-coupled intersubband Terahertz (TACIT) detectors at 1.8-2.4 THz," in *Terahertz Spectroscopy and Applications*, vol. 3617, pp. 58–66, 1999.

[45] C. L. Cates, G. Bricelio, M. S. Sherwin, K. D. Maranowski, and A. C. Gossarcic, "A NON-BOLOMETRIC MODEL FOR A TUNABLE ANTENNA-COUPLED INTERSUBBAND TERAHERTZ (TACIT) DETECTOR," in *9th International Symposium on Space Terahertz Technology*, pp. 597–606, 1998.

[46] C. L. Cates, J. B. Williams, M. S. Sherwin, S. Barbara, K. D. Maranowski, and A. C. Gossard, "Tunable Antenna-Coupled Intersubband Terahertz (TACIT) Detectors for Operation Above 4K 1 Introduction," in *11th International Symposium on Space Terahertz Technology*, 2000.

[47] G. B. Serapiglia, Y. Dora, M. S. Sherwin, M. Hanson, A. C. Gossard, and W. R. Mcgrath, "Design , fabrication and testing of semiconductor tunable antenna-coupled intersubband Terahertz (TACIT) detectors," in *14th International Symposium on Space Terahertz Technology, ISSTT 2003*, pp. 119–120, 2003.

[48] G. B. Serapieia, M. S. Sherwin, M. Hanson, and A. C. Gossard, "Detection of 1 . 6 and 2 THz radiation with a Tunable Antenna- Coupled Intersubba , ncl Terahertz (TACIT) detector .," in *15th International Symposium on Space Terahertz Technology, ISSTT 2004*, no. April, pp. 161–162, 2004.

[49] G. B. Serapiglia and A. C. Gossard, "Ultrafast Tunable Antenna-Coupled Quantum-Well," in *2005 Joint 30th International Conference on Infrared and Millimeter Waves and 13th International Conference on Terahertz Electronics*, pp. 267–268, 2005.

[50] N. Gautam, J. Kawamura, N. Chahat, B. Karasik, P. Focardi, S. Gulkis, L. Pfeiffer, and M. S. Sherwin, "A high-mobility tunable antenna coupled intersubband terahertz (TACIT) detector," *26th International Symposium on Space Terahertz Technology, ISSTT 2015*, vol. 1, pp. 16–18, 2015.

[51] "2021 technology highlights," *JPL Technology Highlights*, 2022.

[52] T. Ando, B. Fowler, F. Stern, I. B. M. T. J, and B. Devices, "Electronic properties of two-dimensional systems," no. 2, 1982.

[53] J. H. J. H. Davies, *The physics of low-dimensional semiconductors : an introduction / John H. Davies.* Cambridge, U.K. ;: Cambridge University Press, 1998.

[54] J. B. Williams, M. S. Sherwin, K. D. Maranowski, and A. C. Gossard, "Dissipation of intersubband plasmons in wide quantum wells," *Physical Review Letters*, vol. 87, no. 3, pp. 37401–1–37401–4, 2001.

[55] F. Arams, C. Allen, B. Peyton, and E. Sard, "Millimeter mixing and detection in bulk InSb," *Proceedings of the IEEE*, vol. 54, no. 4, pp. 612–622, 1966.

[56] B. S. Karasik and A. I. Elantev, "Analysis of the Noise Performance of a Hot-Electron Superconducting Bolometer Mixer," in *ixth International Symposium on Space Terahertz Technology*, pp. 229–246, 1995.

[57] B. S. Karasik and A. I. Elantiev, "Noise temperature limit of a superconducting hot-electron bolometer mixer," *Applied Physics Letters*, vol. 68, no. February, p. 853, 1995.

[58] S. J. Allen, D. C. Tsui, and B. Vinter, "On the absorption of infrared radiation by electrons in semiconductor inversion layers," *Solid State Communications*, vol. 20, no. 11-12, pp. 425–428, 1976.

[59] C. Yoo, M. Huang, J. H. Kawamura, K. W. West, L. N. Pfeiffer, B. S. Karasik, and M. S. Sherwin, "Demonstration of a tunable antenna-coupled intersubband terahertz (TACIT) mixer," *Applied Physics Letters*, vol. 116, no. 1, 2020.

[60] H. J. Blihlmann and M. Ilegems, "Characterization of AuGe/Ni/Au Contacts on GaAs/AlGaAs Heterostructures for Low-Temperature Applications," *1*, vol. 1, no. 9, pp. 2795–2798, 1991.

[61] E. H. Linfield, G. A. Jones, D. A. Ritchie, A. R. Hamilton, and N. Iredale, "The fabrication of back-gated high electron mobility transistors - a novel approach using MBE regrowth on an in situ ion beam patterned epilayer," *Journal of Crystal Growth*, vol. 127, no. 1-4, pp. 41–45, 1993.

[62] R. J. Evans, M. P. Grimshaw, J. H. Burroughes, M. L. Leadbeater, M. J. Tribble, D. A. Ritchie, G. A. Jones, and M. Pepper, "Double two-dimensional electron gas structure formed by molecular beam epitaxy regrowth on an ex situ patterned n+-GaAs back gate," *Applied Physics Letters*, vol. 65, no. 15, pp. 1943–1945, 1994.

[63] K. M. Brown, E. H. Linfield, D. A. Ritchie, G. A. Jones, M. P. Grimshaw, and M. Pepper, "Resonant tunneling between parallel, two-dimensional electron gases: A new approach to device fabrication using in situ ion beam lithography and molecular beam epitaxy growth," *Applied Physics Letters*, vol. 64, no. 14, pp. 1827–1829, 1994.

[64] M. Berl, L. Tiemann, W. Dietsche, H. Karl, and W. Wegscheider, "Structured back gates for high-mobility two-dimensional electron systems using oxygen ion implantation," *Applied Physics Letters*, vol. 108, no. 13, 2016.

[65] J. P. Eisenstein, L. N. Pfeiffer, and K. W. West, "Independently contacted two-dimensional electron systems in double quantum wells," *Applied Physics Letters*, vol. 57, no. 22, pp. 2324–2326, 1990.

[66] M. V. Weckwerth, J. A. Simmons, N. E. Harff, M. E. Sherwin, M. A. Blount, W. E. Baca, and H. C. Chui, "Epoxy bond and stop-etch (EBASE) technique enabling backside processing of (Al)GaAs heterostructures," *Superlattices and Microstructures*, vol. 20, no. 4, pp. 561–567, 1996.

[67] A. F. Croxall, K. Das Gupta, C. A. Nicoll, M. Thangaraj, I. Farrer, D. A. Ritchie, and M. Pepper, "Patterned backgating using single-sided mask aligners: Application to density-matched electron-hole bilayers," *Journal of Applied Physics*, vol. 104, no. 11, pp. 1–7, 2008.

[68] K. D. Gupta, A. F. Croxall, W. Y. Mak, H. E. Beere, C. A. Nicoll, I. Farrer, F. Sfigakis, and D. A. Ritchie, "Linear non-hysteretic gating of a very high density 2DEG in an undoped metal-semiconductor-metal sandwich structure," *Semiconductor Science and Technology*, vol. 27, no. 11, 2012.

[69] C. K. Walker, *Terahertz Astronomy.* 2015.

[70] B. Galdrikian, *Nonlinear and nonperturbative dynamics in quantum wells.* PhD thesis, University of California Santa Barbara, Santa Barbara, CA, 1994.

[71] C. M. Morris, *Interplay of quantum confinement, electron-electron interactions, and terahertz radiation in indium gallium arsenide quantum posts and gallium arsenide quantum wells.* PhD thesis, University of California Santa Barbara, Santa Barbara, CA, 2011.

[72] R. E. Williams, *Modern GaAs processing methods.* Boston: Artech House, 1990.

[73] A. G. Baca, *Fabrication of GaAs devices*. Processing series ; no. 6, London: Institution of Electrical Engineers, 2005.

[74] A. Ketterson, F. Ponse, T. Henderson, J. Klem, and H. Morkoç, "Extremely low contact resistances for AlGaAs/GaAs modulation-doped field-effect transistor structures," *Journal of Applied Physics*, vol. 57, no. 6, pp. 2305–2307, 1985.

[75] M. Kamada, T. Suzuki, F. Nakamura, Y. Mori, and M. Arai, "Investigation of orientation effect on contact resistance in selectively doped AlGaAs/GaAs heterostructures," *Applied Physics Letters*, vol. 49, no. 19, pp. 1263–1265, 1986.

[76] O. Göktaş, J. Weber, J. Weis, and K. von Klitzing, "Alloyed ohmic contacts to two-dimensional electron system in AlGaAs/GaAs heterostructures down to submicron length scale," *Physica E: Low-Dimensional Systems and Nanostructures*, vol. 40, no. 5, pp. 1579–1581, 2008.